UNIVERSITY OF CALIFORNIA
SANTA CRUZ

PLATFORMS FOR *IN VITRO* ELECTROPHYSIOLOGY EXPERIMENTS ON THE INTERNET OF THINGS

A dissertation submitted in partial satisfaction of the
requirements for the degree of

DOCTOR OF PHILOSOPHY

in

BIOMOLECULAR ENGINEERING & BIOINFORMATICS

by

Kateryna Voitiuk

September 2024

The Dissertation of Kateryna Voitiuk
is approved:

Professor David Haussler, Co-chair

Professor Mircea Teodorescu, Co-chair

Professor Benedict Paten

Professor Keith Hengen

Peter Biehl
Vice Provost and Dean of Graduate Studies

Table of Contents

List of Figures

List of Tables

Abstract

Platforms for *In Vitro* Electrophysiology Experiments on the Internet of Things

by

Kateryna Voitiuk

In vitro cultures, including brain organoids, have advanced our understanding of neurodevelopment and disease. However, traditional methods for managing these cultures are labor- and data-intensive and prone to inconsistencies. This thesis presents an Internet of Things (IoT) based experimentation platform addressing these challenges in neuroscience research.

First, we created Piphys, an open-source neurophysiological recording platform with IoT-enabled software, lowering the barrier to entry for multichannel electrophysiology and introducing cloud-based recording for improved data management. Next, we developed a comprehensive IoT cloud laboratory architecture that supports multiple devices and offers software services for communication, data handling, and user interface. We created a generalized device software model and communication standard, establishing a foundation for rapid experiment development, integration, and feedback loops. Afterward, we applied this architecture in a 7-day integrated experiment with imaging, electrophysiology, and fluidics devices sustaining and monitoring cerebral cortex organoids, demonstrating that automation can match manual care results. Finally, in collaboration with UCSF,

we developed a screening system for gene therapy using electrophysiology and optogenetic devices. We demonstrated the ability to suppress seizure-like activity with light in human hippocampal slices from epilepsy patients.

This platform enhances the ability to conduct multi-modal, multi-device experiments and bridges distances between collaborators. It unifies scientific instrumentation and interaction methodology for advancing research in brain development, neuroplasticity, and neurological disease.

This work is dedicated to my friends and family, who have supported me during my Ph.D. journey.

Acknowledgments

Thank you to my Braingeneers colleagues, past and present, including the broader Teodorescu, Salama, and Haussler Labs and the UCSC Genomics Institute and Baskin School of Engineering, for creating a fantastic research environment. I want to especially acknowledge my co-first authors with whom I worked very closely: Jinghui Geng (Sury), John P. Andrews, Spencer T. Seiler, Mirella Pessoa de Melo (Ella), and David F. Parks – you are amazing colleagues, whether in prototyping, experimentation, writing, or review, we worked together through thick and thin, and never gave up. I want to express deep gratitude to Hunter Schweiger, Sebastian Hernandez, Claudia Paz Florez, Matthew G. Keefe, and John Andrews for their hard work on the biological models featured in this thesis.

Mircea Teodorescu, David Haussler, and Sofie Salama: thank you for being there for me for the last seven years, for your enthusiasm and advice, and for allowing me the resources to follow my interests. Tom Nowakowski, Mohammed Mostajo Radji, and Tal Sharf: thank you for your support and guidance on research and career topics. Rob Currie, Dan Freeman, and Jerry Glass: thank you for your positivity and generous engineering advice on the hardware and software aspects of this thesis. Jess Sevetson, I am lucky to have you as a mentor, and thank you for taking our group to the next level in electrophysiology with both your practical and theoretical knowledge. Thank you to my undergraduate

mentees; you have helped me grow and learn as a mentor. I also thank every member of my thesis committee.

I am grateful for the trainee funding and support from the NIH NHGRI T-32 program and to Ed Green, Russ Corbett-Detig, and Angela Brooks for leading the program at UCSC, the ARCS Foundation for the ARCS Fellowship and Agilent Technologies for being my fellowship sponsor, and the University of California Office of the President for the President's Dissertation-Year Fellowship.

Marie Obien, Urs Frey, David Jaeckel, Jan Mueller, Ed Li, and many more colleagues at MaxWell Biosystems: thank you for being open and supportive of my use cases and modifications to your HD-MEA platform and for bringing together a strong electrophysiology research community.

Finally, thank you to Mircea Teodorescu and Sri Kurniawan, as well as David and Lu Haussler, for making me feel welcome and for your support and advice throughout my life before and during graduate school.

List of Terms and Acronyms

Internet of Things (IoT) A network of physical objects embedded with electronics, software, sensors, and connectivity—that enables these objects to collect and exchange data.

Cloud A network of remote servers hosted on the internet to store, manage, and process data, rather than a local server or a personal computer.

Message Queuing Telemetry Transport (MQTT) A lightweight publish-subscribe protocol often used in Internet of Things applications to exchange information between devices.

Spike sorting The process of identifying and classifying neurons and their spike events from recorded electrical signals.

In vitro A process or reaction occurring in a controlled environment, such as a test tube or culture dish, outside a living organism.

In vivo A process or reaction occurring in a whole, living organism.

Ex vivo A process or reaction occurring in tissue from an organism, outside

the body of the organism.

Organoid A miniaturized and simplified version of an organ produced *in vitro* in three dimensions that mimics the structure and functionality of an organ.

Electrophysiology The study of the electrical properties of biological cells and tissues, involving measurements of voltage changes or electric currents on a wide variety of scales from single ion channels to whole organs like the brain or muscle.

Optogenetics A biological technique that uses light to control cells (typically neurons) that have been genetically modified to express light-sensitive ion channels.

Neurodevelopment The process by which the nervous system forms, grows, and matures – from the formation of neurons to the organization of neural circuits and brain structures.

Multi-modal Involving or integrating multiple modes or methods of information delivery or interaction, such as the use of various sensor and actuator types in research or technology.

Chapter 1

Introduction

Recent advances in commodity hardware allow for more affordable computing and storage. The Internet of Things allows many devices to come online when needed and be relinquished when not needed. A multitude of protocols have been developed to effectively and securely manage and communicate with these devices. Affordable, internet-connected devices have already been developed for ECG, EEG, EMG, and heart rate variability monitoring [92, 260, 76, 249, 82, 264]. Furthermore, commodity cloud computing from major companies as well as academic coalitions [223] has become widely available and many tools for downstream analysis to process voltage recordings are already offered online [246, 39, 215, 262, 124]. However, data acquisition for *in vitro* cultures remains relatively isolated, as no platform exists to stream data online to link with these analysis infrastructures.

One solution is to write software add-ons for existing data acquisition systems. However, not all existing data acquisition systems are flexible or open regarding data formats, programmability, and remote control. Additionally, channel count and price range are not always suitable for the desired application.

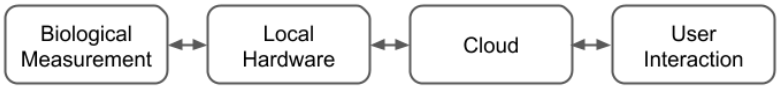

Figure 1.1: **Cloud-based experiment paradigm.** Biological measurement and local hardware are presented to the user through the cloud, such that experiment management and control can be administrated remotely and may be automated by a computer program.

Extracellular voltage recordings from *in vitro* cell cultures are crucial in the investigation of neural activity and dynamics. These recordings allow us to assess information processing in complex neuronal networks and enable discovery on a scale from single neuron firing patterns to local and long-range functional connectivity, network synchrony, and oscillatory activity [74, 19, 185, 90, 233, 211]. *In vitro* neuron cultures connected to a computer through a bidirectional communication system would allow us to systematically test hypotheses over months of culture in a scalable and automated fashion. Such *in vitro* culture models serve as a flexible system that is much easier to scale up than animal models, especially when paired with developments in robotic automation, microfluidics, and probes [157, 215, 190, 2]. A wider application of this technique could be used for drug

discovery and genetic screens.

Further, the combination of longitudinal recordings and large numbers of parallel experimental replicates allows investigations to progress significantly faster and makes new experiments feasible [47]. Scaling up experiments generates the large volume of data necessary for taking advantage of machine learning algorithms (as proposed by SchmidtFutures) and creates a faster turnaround between hypothesis, experiment, and re-testing [193].

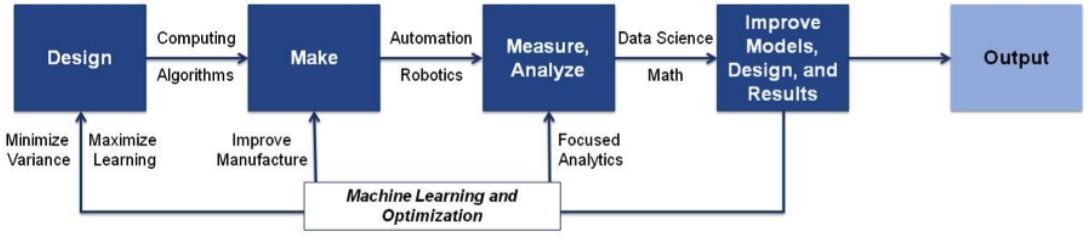

Figure 1.2: **The scientific method with computer optimization.** Proposed by philanthropic initiative, SchmidtFutures[1].

1.1 Overview and Motivation

During the initial stages of growth and development, the human brain self-assembles from a vast network of billions of neurons into a system of immense capability for sophisticated cognitive and learning behaviors. The human brain maintains those capabilities over a lifetime of homeostasis and accumulates many

[1]https://schmidtfutures.com/our-work/scientific-knowledge/ai-accelerator

activity patterns of memories and learned behaviors. The exact mechanisms that allow such properties to emerge from the initial neuronal organization at birth remain unclear.

Over decades of inquiry, much progress has been made in studying large-scale patterns or behaviors exhibited by the brain. Advances in those studies include a much better grasp of brain physiology and human psychology. Much progress has also occurred in understanding the brain at a cellular level. For example, the structure of an individual neuron is no longer a mystery to the neuroscience community. However, it remains unclear how neural interactions on the order of 10,000 cells create higher-order information processing. This missing link – a theory that would unify what was learned about the brain at a macroscopic and microscopic scale – is the most intriguing problem in modern neuroscience. Understanding what goes wrong in this process allows us to model and move towards treating disease. A possible next step for the field would be to study *in vitro* models of such emergent information processing and create computational models with comparable performance.

1.2 Identification of Problem

Even though the emergence of cognition from seemingly simple components has been a focus of much research - over years of inquiry, we have yet to see a

theory that would have adequate predictive strength or descriptive elegance. The pace of progress in this area has been limited by experimental toolkits available to researchers. New tools are required to either enable novel experimental approaches or to achieve robust statistical confidence in data outcomes. As a rapidly evolving field, neuroscience continually benefits from the emergence of such tools. For example, the development of various organoid models refined over the last decade is shown in Figure 2.2 allowed scientists to have a more transparent view on human neurodevelopment in a dish.

Longitudinal recordings are essential to capture features of neurodevelopment and dynamics - only long continuous observations could give us a chance to understand properties of neuron development, how 2D and 3D cultures grow and change activity patterns, what rhythms the activity may follow [159, 257, 266, 267], and what genetic mechanisms are responsible for our neural structure and cognition. Organoids should remain online continuously instead of being taken on and off of expensive instruments for short recording periods. Long-term recordings are essential to study responses to electrical or drug stimuli over weeks and months.

Longitudinal recordings from multi-channel experiments demand vast amounts of data and memory. The data is challenging to manage, especially since out-of-the-box hardware and software are often offline. Storage on physical disks usually requires manual monitoring and laborious data transfer for backup or processing.

Furthermore, many recording systems require a designated workspace for experiments with a physical computer nearby with cables or wireless transmission to stream data. Several open-source efforts have been created to provide more affordable and modifiable recording equipment [54, 217, 162, 109, 63]. However, no software solutions exist to easily manage and control a large amount of electrophysiology equipment and data simultaneously.

Additionally, current commercially available solutions are cost-prohibitive for large-scale (even dozens of organoids) experimentation. Reducing the cost of electrophysiology hardware from hundreds of thousands to just thousands of dollars per experiment will allow scalability. Lower cost and ease of management of recording hardware and data would allow a greater number of organoids to run simultaneously, improving the statistical robustness of a given experimental result.

Another feature lacking from the tool kit of today's neuroscience is a common experimental platform. Current recording hardware and experiment management software are not adequate for the immediate needs of today's neuroscience. This discourages multi-modal experiments, which would integrate many different devices performing measurements and perturbations together, where a measurement could influence a specific perturbation sequence. Lack of flexibility and programmability. Not automated, we cannot use computers to make quick progress.

Cloud biology is well suited for education because it enables students to access, control, and experience advanced experiments in a professional laboratory beyond the capabilities of high school or undergraduate classrooms. I hope to demonstrate the broader applicability of IoT to fundamental research, focused on its ability to create versatile experiments through multi-device monitoring and automation.

1.3 Contribution to the Field

This thesis introduces a novel experimentation platform standardizing laboratory device operation, communication, data management, and links to analysis. It enhances scientific throughput by automating diverse experiments, enabling feedback loops, and improving reproducibility through consistent workflows. The platform facilitates multimodal experiments combining various measurement and perturbation techniques.

The key contributions of this work include:

- **Piphys**: An open-source electrophysiology platform for low-cost multichannel electrophysiology which introduces cloud-based recordings, described in Chapter 3.

- **IoT Cloud Laboratory and Device Software Package**: A generalized framework for integrating many devices into a cloud-connected experiment,

described in Chapter 4 and further developed in Chapter 5.

- **Electrophysiology, Fluidics, and Imaging Platform**: A cloud-connected system for managing multi-modal devices and their cooperation in biological experiments, described in Chapter 5. Experimental results showed automated sustenance of organoids can achieve the same results as manual care.

- **Optogenetics Platform**: A system designed for optogenetic control and manipulation of neuronal activity in conjunction with electrophysiology recording, described in Chapter 6. Experimental results showed that it is possible to shut down epilepsy by suppressing excitatory neuron populations with optogenetic inhibition in human hippocampus slices.

The thesis chronicles the development of these platforms and their applications to *in vitro* electrophysiology within the Internet of Things (IoT) cloud laboratory. The contribution is to unify scientific instrumentation and interaction methodology for advancing research in brain development, neuroplasticity, and neurological disease.

Chapter 2

Background

2.1 Neurons and Neural Spikes

A typical cortical neuron with labeled functional parts is shown in Figure 2.1b, with its distinct neural spike waveform in Figure 2.1b. A neuron has many different membrane proteins, which are proteins embedded within its lipid bi-layer membrane [218]. The neuron uses the membrane proteins to selectively pump out positive ions like sodium (Na+), potassium/kalium (K+), and calcium (Ca+), using the chemical energy from adenosine triphosphate (ATP) [219]. As a result, the inside of the cell becomes relatively more negative than the outside. Thus, the cell converts chemical energy into electrical potential energy by separating ionic charges across its cell membrane and creating a negatively (polarized) membrane

resting potential relative to the outside [85]. Next, depolarization (a neural spike or action potential) occurs when other membrane protein channels (i.e., ligand-gated and voltage-gated) open and allow positive ions to rush back into the cell, creating an electrical cascade that echoes down the neuron's axon and reaches the presynaptic terminal [84]. At the presynaptic terminal, this electrical signal triggers the influx of calcium ions, which in turn causes synaptic vesicles containing neurotransmitters to fuse with the cell membrane and release their contents into the synaptic cleft [105]. The neurotransmitters diffuse and bind to specific receptors on the postsynaptic neuron [51]. Depending on the type of neurotransmitter and receptor, this binding can either excite or inhibit the postsynaptic neuron, potentially triggering a new action potential and continuing the signal propagation [102]. After signaling, neurotransmitters are rapidly removed from the synaptic cleft, either through reuptake by the presynaptic neuron, degradation by enzymes, or uptake by surrounding glial cells, ensuring precise temporal control of synaptic transmission [95].

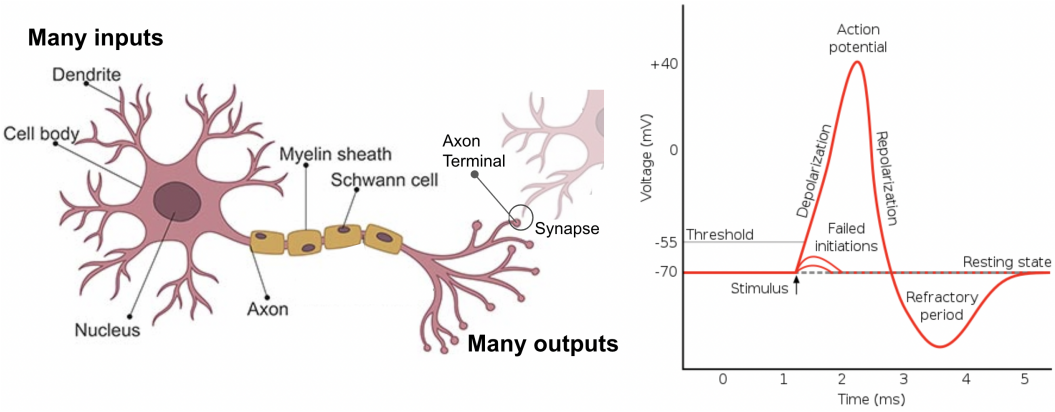

Figure 2.1: **The neuron and its action potential.** **(a)** A cortical neuron with labeled functional parts. The neuron receives inputs from other cells through dendrites. Inputs to the cell may be strong enough to trigger a membrane depolarization or spike, in the neuron. The spike propagates down the axon to reach other neurons. While the signal propagating along the axon is electrical, signals between neurons are typically passed through chemical neurotransmitters within synapses. Image adapted from Cusabio[1]. **(b)** An example of a voltage trace of a neural spike, measured with respect to the inside of the neuron. The neuron starts at a resting internal membrane voltage of -70 mV. As the neuron integrates inputs from its dendrites, voltage-gated sodium channels in its cell membrane open and let ions in, causing depolarization. The rush of ions overshoots and hyperpolarization is followed by a refractory period. Image adapted from Wikimedia Commons users Chris73 and Diberri[2].

2.1.1 Neural Connectivity and Network Structure

The human brain contains about 86.1 ± 8.1 billion neurons [11]. Each neuron has connections with other neurons via synapses. There are many different kinds of neurons with different morphologies and different roles, such as excitation and inhibition, responding and releasing different neurotransmitters within their

[1] `https://www.cusabio.com/Cell-Marker/Neuron-Cell.html`
[2] `https://commons.wikimedia.org/wiki/File:Action_potential.svg`

synapses. Much of the neural organization in the brain is driven by genetic mechanisms and afterward wired through experience during an organism's lifetime. The brain exhibits hierarchical organization with small-world networks with high local connectivity and more sparse long-distance connections [16, 140]. Organizational regularities include brain regions with distinct topologies. For example, cortical columns [153] are guided by radial glial cells [183, 151, 186]. Cortical columns form feedforward (FF) and feedback (FB) information processing streams as "counter-stream architectures" [140, 141, 240].

2.2 Electrophysiology

Electrophysiology measures the electrical activity of neurons and the nervous system to understand their function. Neuroscientists use a diverse toolkit of techniques to measure and analyze neuronal activity, combining electrical and optical approaches. These methods provide crucial insights into neuronal function at various scales, from single cells to entire brain regions.

2.2.1 Electrical Methods

The primary measurements in electrophysiology include: voltage (action potentials and subthreshold membrane potential changes), current (ion flow across cell membranes), resistance (membrane and axonal properties), and capacitance

(cell membrane characteristics).

Voltage measurements allow us to assess information processing in complex neuronal networks and enable the discovery of trends on the scale of a single neuron firing to local field potentials and long-range functional connectivity, network synchrony, and oscillatory activity [74, 19, 185, 90, 27, 233, 211].

Intracellular voltage recordings (i.e., patch-clamp) measure with respect to inside the cell [160, 73]. Extracellular voltage recordings measure with respect to outside the cell [97, 80]. Voltage measurements are done with electrode probes, which are typically small insulated wires with an exposed tip. Electrodes can come in many formats, such as planar microelectrode arrays (MEAs) (also referred to as multielectrode arrays) [224, 163, 265, 50], flexible 3-dimensional microelectrode array baskets [170] that record neurons near the surface of neural tissue, stiff arrays of silicon probes [259, 190, 207] inserted inside the tissue via a micromanipulator, implantable mesh electrodes [130, 125], and tetrodes [79] which flexibly splay out when inserted into tissue, covering a larger 3D space. Examples of electrodes can be visualized in Figure B.2. Electrode probes are bi-directional, meaning they can switch between recording (measuring neural output) electrical voltage and stimulation (producing neural input) by inducing electrical voltage.

2.2.2 Optical Methods

Neural activity can also be measured using fluorescent labeling and imaging techniques, offering complementary advantages to electrical recording methods. Fluorescent indicators can be visualized using high-resolution cameras, providing excellent spatial resolution and allowing for the observation of large neuronal populations simultaneously [4].

Indicator dyes, such as Fura, Fluo, and Indo, work by penetrating inside cells and binding to intracellular calcium [227, 69]. In contrast, genetically encoded calcium indicators (GECIs), such as the green fluorescent GCaMP family, offer reduced cytotoxicity compared to dyes [35]. Genetically encoded voltage indicators (GEVIs), such as ArcLight and ASAP1, allow for faster detection of membrane potential changes that can resolve high-frequency spike trains [99, 225]. GECIs and GEVIs require genetic modification of a cell line to express the proteins, while dyes can be used with any cells on the day of the experiment.

For stimulation purposes, optogenetics has emerged as a powerful technique. Section 2.1 described how membrane proteins can regulate membrane potential by pumping out or letting in ions. Optogenetics utilizes genetically modified neurons that express light-sensitive membrane proteins, called opsins, allowing for precise temporal and spatial control of neural activity using specific wavelengths of light [68, 43, 59, 263]. Excitatory opsins like channelrhodopsin-2 (ChR2) can depolarize

neurons in response to blue light, while inhibitory opsins such as halorhodopsin (NpHR) can hyperpolarize neurons in response to yellow light [68, 263].

Wild-type cells typically do not express calcium indicators or opsins naturally. Therefore, genetic engineering is required, typically through CRISPR-Cas9 [195] genome editing of cell lines or through viral vector delivery, such as adeno-associated virus (AAV) [158]. Both methods can be used to target specific cell types [133], which allows more precise perturbations to understand the role of specific cell types in neural activity. AAV delivery is advantageous when genetic modification of tissue must be done shortly before the experiment, as it can effectively transfect cells within a week [33].

Both electrical and optical methods can be combined to create versatile recording and stimulation methodologies, leveraging the strengths of each approach to meet specific experimental needs [83].

2.2.3 Data Acquisition Hardware and Software

Data acquisition hardware is a vital component of an electrophysiology setup, driving voltage sampling and secure storage of data in computer memory. First, voltage measurements from electrode probes must be amplified. Amplification is performed by an operational amplifier circuit (op-amp). Afterward, the signal must be digitized or converted from an analog signal into a digital number which

can be stored in a computer. The process is done by an analog-to-digital converter (ADC). Often, amplification and digitization can be combined on the same silicon chip (such as Intan) [75]. A computer central processing unit (CPU) or field-programmable gate array (FPGA) can drive the circuit to produce digitized voltage samples at a specific clock rate, also known as the "sampling rate" of the recording. This timed stream of samples is stored in computer memory for subsequent analysis and a record of the experiment. A detailed comparison of existing and proposed electrophysiology data acquisition systems is in Appendix A.

2.2.4 Spike Sorting

Multi-electrode arrays with thousands of channels have been used to measure tens of thousands of neurons [199, 155]. Experiments at this scale cannot be inspected by hand for spiking neurons. Spike sorting algorithms aim to identify individual neurons in neural tissues [196, 128, 199]. Algorithms such as MountainSort4 [39], Kilosort [168], and SpykingCircus [262] use specific clustering techniques, as well as thresholding, to identify often illusive neural activity. Deep learning-based methods for spike sorting use convolutional networks or combinations of convolutional and recurrent artificial neural network architectures to detect spikes [201, 150]. Unsupervised spike sorting with deep learning [22, 21] or classical machine learning [192, 86] can eliminate bias from training sets curated

by humans.

Although simple thresholding techniques are less accurate than more involved sorting algorithms, thresholding is faster and more computationally efficient during real-time analysis [138, 155]. Many algorithms running on FPGAs contain application-specific circuits that can accelerate neural detection through signal thresholding on the order of micro-seconds (faster than a neuron fires in milliseconds) [169, 184, 230]. However, advances in speed, efficiency, and size of Graphical Processing Units (GPUs) would also allow the acceleration of classical and deep learning algorithms near the site of neural recording [150].

2.2.5 Open-Loop and Closed-Loop Experiments

Open-loop experiments are performed either by passive observation of neural activity or by linear, reductionistic stimulation and recording of response [189]. Closed-loop experiments, on the other hand, take advantage of the inherent feedback and "loopiness" part of the nervous system and its dynamic interactions with the world. The experiments may involve placing neural cultures inside a virtual environment or embodying neural cultures with an artificial animal (animat) through a sensory-motor loop to create an interactive environment with structured stimuli [44, 34, 112]. By putting a computer in the loop with neural cultures, it is possible to control the system being studied and explore the

functional consequences.

Closed-loop experiments require fast signal processing and decision-making to generate a stimulation pulse in response to neural activity patterns [234]. Efficient closed-loop experimentation can be programmed through an FPGA with feedback on the order of 10 µs [169, 230, 184]. To date, closed-loop neural experimentation has only been done inside labs on a small scale [197], with much of the work pioneered by Steve Potter's lab. Further research in closed-loop systems will enable neuroscience studies at a deeper interactive level.

2.3 Biological Models of the Brain

2.3.1 *In Vivo* Models

In vivo models have been the standard model of study ranging from worms and flies [32, 41, 20], mice [61, 78, 79, 94], all the way to monkeys [58, 209, 15, 187] and humans [103, 121]. *In vivo* models are considered the most realistic and state-of-the-art. At the same time, there is currently a limited observational capability due to the number of physically possible interventions that could be performed on an animal. Sectioning animal brains into slices [104, 165, 139] to have a more in-depth investigation into neural dynamics, brings the *in vivo* model into the open for observation.

2.3.2 *In Vitro* 2D Models

In vitro models, such as acute brain slice cultures and two-dimensional plated neuron cultures, became key to investigating neuroscience principles, allowing us to examine how the brain works in a dish. Protocols for reprogramming cells [229] opened the door for the widespread use of human-derived pluripotent stem cells, which previously only came from embryonic sources and were therefore limited. Traditional two-dimensional cultures were the basis for many early network activity experiments [247, 13, 159]. Nonetheless, two-dimensional cultures have limitations of low cell density, and a stiff, flat surface of the culture dish is not physiologically natural [25].

2.3.3 *In Vitro* 3D Models

Three-dimensional culture models [12] are more physiologically relevant through cell morphology, extra-cellular matrix production, cell density [118], neural activity [238], and ion channel expression [119]. Brain organoids are three-dimensional neural tissue structures generated from human stem cells (iPSCs), which can model neural development and connectivity [120]. Electrophysiological experiments have displayed neural activity in cerebral organoids [213, 233, 204, 191, 258]. Organoids are more realistic than two-dimensional cultures, recapitulating the brain, which is inherently three-dimensional. Organoids are the best *in vitro*

model we have at the moment and future-proofing capacity (the field is supportive – with the scientific community engineering organoids advances with glial subpopulations, connections with each other, better reproducibility, and nutrition). Innovations on organoids include fused organoids of different tissue types (assembloids) [179, 214], and brain organoids connected together by axon bundles (connectoids) [42, 167].

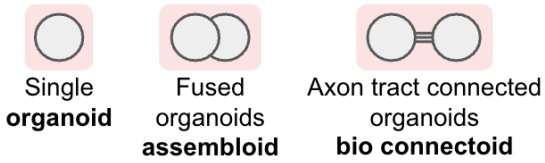

Figure 2.2: **Types of organoids.** On the left are types of organoids published in literature: *single organoids* [120], *assembloids* [180, 214], and *connectoids* [42, 167].

2.4 Internet of Things for Biology

In the past, cloud biology has been used for biology education [87, 88, 235], ecology [71], agriculture [60] and marine biology [256]. Cloud systems are advantageous for research experiments where live sensors are spread across vast distances. Ecology and marine biology experiments use cloud biology to control a fleet of sensors as they traverse through vast ecosystems, like forests and oceans [77]. Such systems have been used to protect the environment through disaster management by monitoring information in sparsely populated areas [3].

In the specific case of IoT cloud biology, the most commonly mentioned IoT-connected biological devices come from the field of medicine. IoT is an emerging technology in medicine, where it has been named the Internet of Medical Things [203, 243]. Small medical devices connected to the Internet are useful for collecting biological data from patients' vitals [117]. IoT devices have been proposed for monitoring the health of fetuses in pregnant women [131]. Online architectures for monitoring wearable medical devices are encompassed in the larger field of telehealth [56, 72]. Not all applications of IoT devices in medicine are used to collect biological data. For example, non-wearable motion detectors may be used to monitor the safety of patients in the hospital [93].

IoT has been used less commonly in the laboratory of cellular biologists. Some examples exist from ecology and Amazon Alexa integration of lab devices [111], to commercial devices [181]. As in the general case of cloud biology, one of the notable use cases of IoT is in educational experiments [235].

Chapter 3

Light-weight Electrophysiology Hardware and Software Platform

3.1 Introduction

There is a need in the neuroscience community for flexible, programmable electronics to record *in vitro* cultures, such as organoids, to understand activity changes over time during development. Appendix A compares existing electrophysiology platforms. Most electrophysiology platforms, including Open Ephys, require a dedicated personal computer and benchtop space, none are IoT-controlled and are generally expensive (tens of thousands of dollars). Combined, these factors create a barrier to entry and difficulties with scalable use. Therefore, the goal

of Aim 1 is to create an inexpensive, optimized electronics platform for interfacing with neural culture models.

Throughout the work, we will refer to the hardware created as "Piphys". The name Piphys comes from the combination of "Raspberry Pi" and "electrophysiology". The Raspberry Pi is a low-cost, small-scale, single-board computer. Piphys eliminates the need for a desktop or laptop computer to manage an electrophysiology experiment or for an operator to be present in the lab to initiate a recording. The system is built for long-term experiments with the goal of full automation using programs that can optimize experimental protocols.

The following sections explain the progression of Piphys systems along with descriptions of their functionality. The critical physical innovation in Piphys devices is the hardware expansion boards that enable a Raspberry Pi computer to interface with an Intan RHD chip to perform electrophysiology.

3.2 Results

3.3 Piphys Pilot

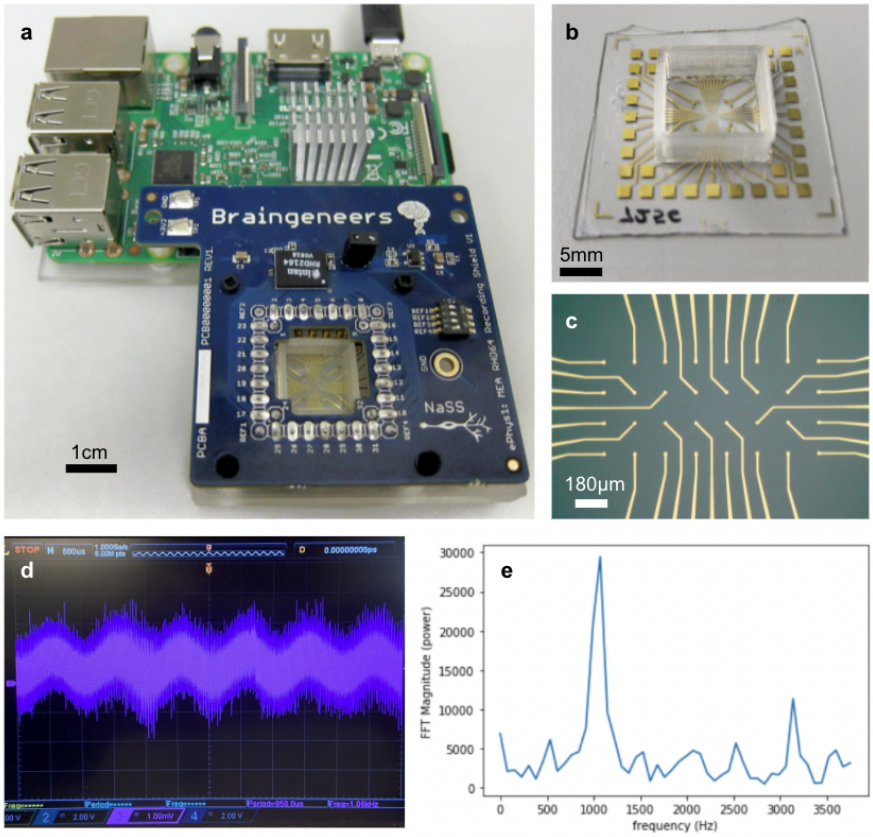

Figure 3.1: **Piphys Pilot design.** **(a)** Electrophysiology recording shield (blue) interfaces with the Raspberry Pi and enables voltage measurements. **(b, c)** Multielectrode array fabricated at UC Santa Cruz containing gold PEDOT:PSS electrodes (25 µm diameter) spaced 180 µm center-to-center on glass. **(d)** 1kHz attenuated waveform produced by a benchtop waveform generator and voltage divider, recorded by an oscilloscope. **(e)** Fast Fourier Transform of signal recorded by the Pilot. The spectrum is noisy due to attenuation, with the peak around 1kHz, as expected.

3.3.1 System Design

3.3.1.1 Hardware Design

Circuit design

The printed circuit board was designed in Autodesk Eagle. The Intan RHD2000 electrophysiology amplifier chip is the key driver of the shield biopotential-sensing functionality. The chip amplifies voltage signals sensed by the electrodes and converts the analog to digital values for storage and buffering inside the Raspberry Pi Computer. A switch slide chip allows the user to select a reference electrode, e.g., the electrode closest to the tissue sample. A low-noise linear voltage regulator was used to convert 5V power from Raspberry Pi to 3V power used by the chip. Although the Raspberry Pi has its own 3V power output, voltage conversion was used to smooth and isolate any power fluctuations from the power supply. The recording shield hangs off the board's edge, furthest away from the computer electronics to reduce potential electrical noise exposure.

Multi-electrode array

A custom multi-electrode array fabricated at UC Santa Cruz is at the system's center. It contains 32 gold electrodes (25 µm diameter) spaced 180µm center-to-center on a glass wafer. The electrodes are coated in PEDOT:PSS, which lowers electrical impedance, thus enhancing the conductivity of signals [176]. Four reference electrodes shaped as curved arches are located on the periphery of the

sensing area.

Interfacing recording Piphys Pilot with multi-electrode array

The recording shield connects to the contact pads on the electrode array using spring-loaded pogo pins, which adapt their height and maintain contact with the surface. The design can be adapted to Multi-electrode arrays of different form factors using interface boards, allowing the usage of both custom and commercial footprints. Pogo pins remain the most popular and accessible contact solution. Wire bonding the MEA to the circuit board and push-pull connector to the shield may be a more elegant solution but requires additional equipment and manufacturing time.

The Raspberry Pi, recording shield, and multi-electrode array are held together by a 3D printed base prototyped with Formlabs Clear V2 material. M2 nylon standoffs are inserted into the base using a friction fit and secure the shield to the base. The base and electronics can all be coated in an inert material such as Parylene C to ensure bio-compatibility.

3.3.1.2 Software Design

The software design described in Section 3.4 is fully compatible with the Pilot, using the same low-level software drivers and high-level cloud APIs.

3.3.2 Results

Validation of the electrophysiology system was performed with a benchtop signal generator. The generator was set up to produce a sine wave with frequency 1kHz and amplitude 1V. The sine wave was attenuated with a voltage divider circuit from 1V to 2mV, to fall in the sensing range of the Intan RHD2000 chip. The magnitude of attenuation made added a lot of noise to the signal.

The interface pins of the electrophysiology shield were placed in contact with a conductive pad, which was tied to the attenuated wave. All 32 channels were recorded simultaneously. A Fast Fourier Transform of Channel 0 is shown in Figure 3.1e.

3.3.3 Discussion

Validation could have been performed more thoroughly using a signal generator capable of producing a range of low-amplitude waveforms with slower frequencies. 1kHz was the lowest frequency of the benchtop signal generator, which is still too fast to emulate neuronal firing rate. A signal generator such as the hs-tester device from White Matter would be suitable for finer testing and tuning.

There were many small mistakes in the first implementation of the hardware due to unforeseen nuances in programming. Further, the RHD2000 64 channel chip was used to record a 32 channel electrode array due to the availability of

components on hand. Therefore, only half of the channels on the chip were wired, and the rest remained floating. During the programming phase, it became apparent that the chip has two analog to digital conversion elements (ADCs), each serving 32 channels, and it was preferable to sample only one of them to increase the sampling rate over the Serial Peripheral Interface. However, it turned out the electrodes were wired to both ADCs, thus the resulting system had about 15 active electrodes out of the possible 32. The system also lacked modular connectors to enable the attachment of different probes to the electrophysiology shield, without being constricted by the original MEA footprint geometry. These problems were addressed in the next-generation device, described in the following section.

3.4 Piphys Main Design

The following content in this Section 3.4 is from the journal article published in the IOPscience Journal of Neural Engineering [244]. I wrote the hardware design and data analysis section, while Sury Geng wrote the software and experiment sections and accompanying figures, Matt Keefe wrote the tissue culture section, David Parks wrote the dashboard section. I have edited and revised all sections with the team throughout the process.

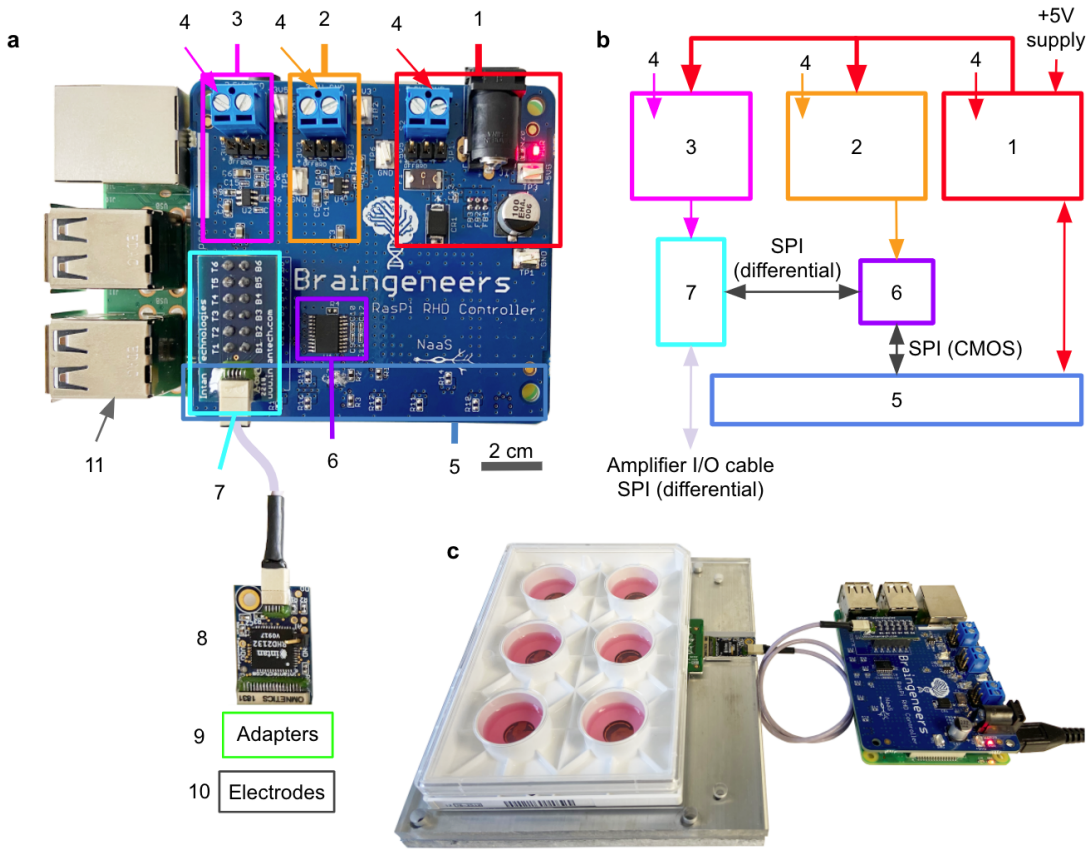

Figure 3.2: **Piphys main design. (a)** Expansion shield (blue board) attached on top of Raspberry Pi (green board). **(b)** Logic level connection. **(c)** Example interface with standard 6-well electrode plate. (1) +5V logic, (2) +3.3V logic, (3) +3.5V logic, (4) External supply inputs, (5) Raspberry Pi input/output pins (bottom), (6) LVDS converter, (7) Intan RHD adapter, (8) Intan RHD 32-channel recording headstage containing Intan RHD2132 bioamplifier chip, (9) Optional adapter board to electrodes, (10) Multiple electrode types possible, (11) Raspberry Pi computer (bottom).

3.4.1 System Design

3.4.1.1 Hardware Design

Circuit design

An expansion shield connects the Raspberry Pi to the Intan RHD 32-channel

recording headstage containing the Intan RHD2132 bioamplifier chip. The chip is configured to use low-voltage differential signaling (LVDS) to reduce the effects of noise and electromagnetic interference (EMI) and allow increased cable length. However, the Raspberry Pi communicates using complementary metal-oxide-semiconductor (CMOS) level logic. To translate between the two signal types, the expansion shield uses the SN65LVDT41 chip from Texas Instruments. The SN65LVDT41 chip has four LVDS line drivers and one LVDS line receiver to control data lines required to communicate with the Intan chip over its Serial Peripheral Interface (SPI).

Besides translation between signal types, the expansion shield provides different levels of power derivative from the +5V source input. The +5V input powers both the Pi and shield, can be supplied either through the power barrel on the shield or through the micro-USB on the Pi for flexibility. On the shield, the power source is filtered through ferrite beads to remove high-frequency power line noise. The +5V source is converted to a +3.5V source for the Intan RHD2132 bioamplifier chip and a +3.3V for the SN65LVDT41 chip. Conversion is performed by low-noise linear voltage regulators to smooth and isolate any fluctuations from the power supply.

Connection to electrodes

Electrodes are connected to the Intan RHD 32-channel recording headstage.

For experiments reported here, we created a connection to a commercially available 6-well multi-electrode array (MEA) plate from Axion Biosystems. However, any other electrode system fitting an Omnetics 32-pin connector is compatible. The design can be adapted to custom and commercial MEAs of different form factors using adapter boards shown in Figure B.2.

The Axion electrode plate mates its bottom contacts to spring finger pins on our designed adapter board. The parts are aligned using a custom holder consisting of a plastic interior surrounded by aluminum plates and compressed together by screws on four corners. The plastic holder has a slot to hold the adapter board and a groove to align the plate in the correct position. The aluminum plate casing prevents warping of the plastic and ensures even pressure compressing the plate and connector on both sides. The compressing holder provides consistent mating of spring finger pins to electrode contacts on the plate.

The mapping of electrode position to channel number is shown in Appendix B.

System performance

To reduce environmental noise and maximize the signal-to-noise ratio (SNR), we use a Faraday cage during recording. The Faraday cage is made of 1 mm thick steel with a power line connected to earth ground. For noise measurements, an empty Axion plate was filled with the same media used in cell culture and placed

in the Faraday cage. The noise baseline of this media-only system was an average of 2.36 $\pm$ 0.4 μV RMS for all the channels with digital software filters. A 60 Hz IIR Notch filter was applied to remove the power line noise before recording primary human neuron culture. In addition, a 300-6000 Hz 3rd order Butterworth bandpass filter was used to attenuate frequency components outside the neural activity range.

3.4.1.2 Software Design

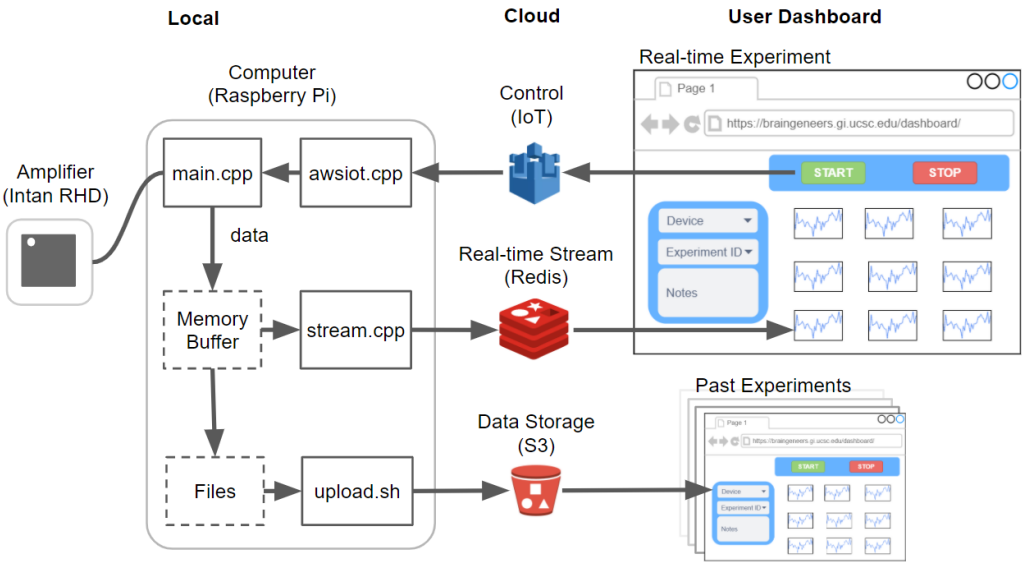

Figure 3.3: **Software overview**. The software that runs on the local Raspberry Pi device communicates with the Intan RHD2132 bioamplifier chip to stream and store the digitized neural signal. Concurrently, it pushes the signal to Redis for real-time visualization on the online dashboard. Datasets are also uploaded to S3 after each recording for permanent storage and access. Experimental control such as 'start', 'stop', and variable configuration is sent from the dashboard through Amazon IoT to the local device. Past experiment data can also be browsed using records from S3.

The Piphys system runs custom software to perform: (1) communication with the Intan RHD2132 bioamplifier chip, (2) buffering and file storage of recorded voltage data locally, (3) real-time data streaming and plotting on the online dashboard, and (4) experiment control from the dashboard. In order to stream data, interact with data being recorded, and control the device, we deployed Redis, Amazon IoT, and S3 as described in Methods.

To perform an electrophysiology recording, the user can configure the sampling rate and start the experiment from the dashboard. Once started, the neural cell activity is firstly digitized and sampled by the Intan RHD2132 bioamplifier chip in 32 channels. Raspberry Pi stores the data on local memory and also streams it to Redis for real-time visualization on the online dashboard. For data integrity and upload efficiency, raw data is saved every 5 minutes on local memory and streamed every 10 seconds to Redis. Once the recording ends, all local data files are uploaded to S3 for permanent storage, and data is further backed up to Amazon Glacier for long-term archiving. Local data files on the Pi auto-erase every 14 days to release memory. To view a dated recording, the user can select and pull the data files from S3 to the dashboard for display (Figure 3.3).

Communication with hardware

Communication between Raspberry Pi and Intan RHD2132 bioamplifier chip uses Serial Peripheral Interface (SPI). SPI is a fast and synchronous interface

that is widely used in embedded systems for short-distance data streaming. It is a full-duplex master-slave-based interface where both master and slave can transmit data at the same time. The protocol for both Raspberry Pi and Intan RHD2132 bioamplifier chip is a four-wire interface: Clock (SCLK), Chip select ($\overline{CS}$), Master-Out-Slave-In (MOSI), and Master-In-Slave-Out (MISO). In Piphys, the Raspberry Pi acts as the master device and generates a clock signal and recording commands to configure the Intan RHD2132 bioamplifier chip through MOSI. The Intan chip responds as slave and sends the digitized data back by MISO. The chip allows configuration of sampling rate and bandwidth of the low-noise amplifiers. The 32 channels on the chip are sampled sequentially with available sampling rate options from 2 kHz to 15 kHz per channel. The amplifiers give 46 dB midband gain with lower bandwidth from 0.1 Hz to 500 Hz, and upper bandwidth from 100 Hz to 20 kHz.

Online dashboard

Users interact with Piphys devices through a web browser application, referred to as the Graphical User Interface (GUI). The GUI allows a user to initiate a recorded experiment and monitor electrical activity on each channel. Programatically, the GUI mimics an IoT device that sends messages to other devices (i.e., Piphys units) and listens to their corresponding data streams in a high-performance Redis database service. The Piphys device produces a single data

stream to Redis, and many users can view the stream from the Redis server. Therefore, many users can monitor and interact with a particular Piphys device without additional overhead placed on that device.

Users can be located anywhere on the Internet without concern for where the physical Piphys device is or which network it is on. We routinely perform electrophysiology experiments from Santa Cruz on a Piphys-connected device that is located 90 miles away in San Francisco.

When a new user opens the browser GUI, the web application queries the AWS IoT service for online Piphys devices to populate a device dropdown list. When the user selects a device from the dropdown, an MQTT 'ping' message is sent to the relevant device every 30 seconds, indicating that a user is actively monitoring data from that device. As long as the Piphys device receives these pings, the Piphys device will continue to send its raw data stream to the central Redis service. When the Piphys device has not received any user messages for at least a minute, it will cease sending its raw data stream. This protocol ensures the proper decoupling of users from devices. The Piphys device is not dependent on a user gracefully shutting down.

While the Piphys device feeds raw data to the Redis service, data transformations are applied downstream by other IoT-connected processes. For example, the Piphys Control Panel displays a threshold spike sorted transformation of the raw

data. This data transformation is an independent process that listens for MQTT requests for the raw data stream and transforms the raw stream into a stream containing the past ten spike events detected per channel. For channels with no detected spikes, a random sample of the channel is saved to the stream every 30 seconds to provide a sampling of the channel's activity.

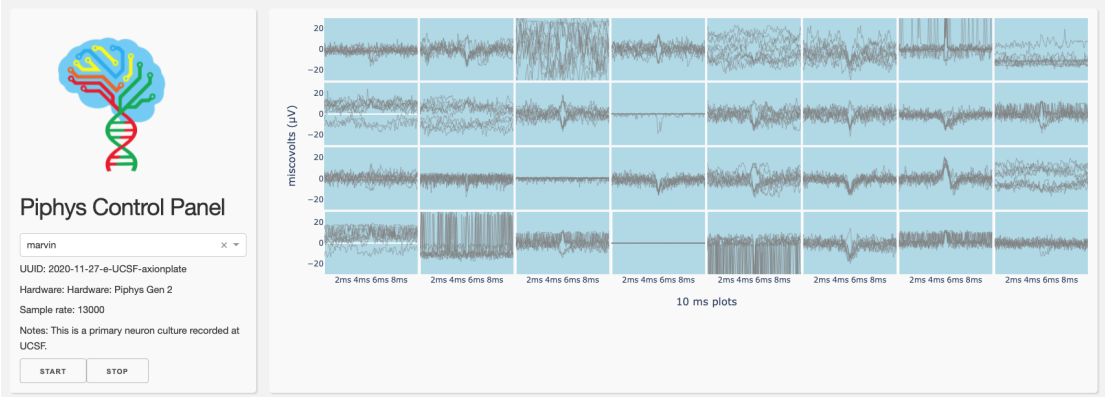

Figure 3.4: **Dashboard.** A control panel interface is displayed through the browser running spike detection by thresholding.

3.4.2 Results

We tested the Piphys system for long-term recordings of human primary neurons. These neurons were cultured in an Axion CytoView MEA 6-well plate (see Methods section below). After recording, the raw data was ingested to SpyKING CIRCUS software [262] for analysis. SpyKING CIRCUS is a semi-automatic spike sorting software that uses thresholding, clustering, and greedy template match approaches to detect single cell action potentials. Here, we show two types of results,

first for single neuron recordings and second for a bursting neural network.

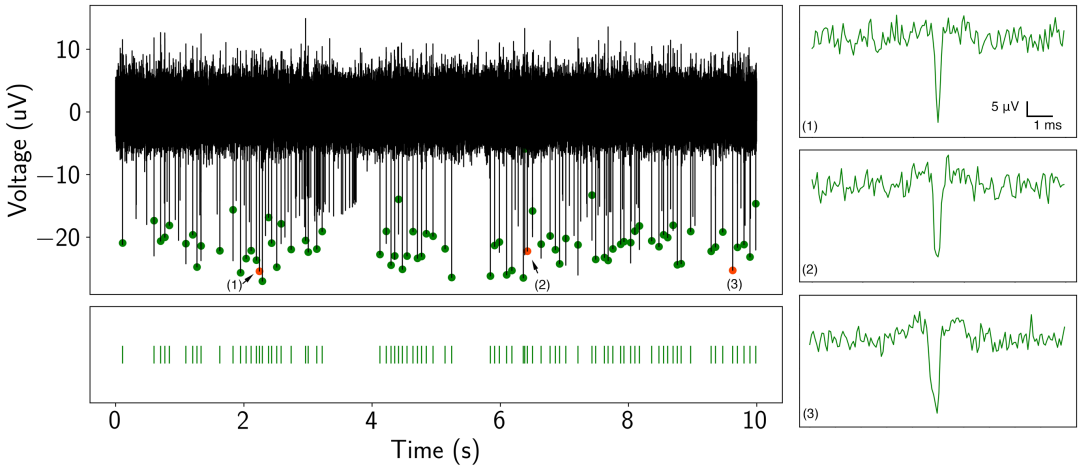

Figure 3.5: **Detection of neuronal spike activity using Piphys.** Spike train (black trace) from a recorded neuron in the time domain from Piphys. Spikes shown here are sorted from SpyKING CIRCUS software and labeled on the raw data with green and orange dots. Bottom: spike raster is aligned with the detected spikes showing firing activities at specific positions. (1)(2)(3) Individual spike examples randomly picked from the spike train.

Recording from primary neurons

After 14 days in culture, primary neurons were recorded with the Piphys system and two commercially available systems: the Intan RHD USB interface board and the Axion Maestro Edge. After recording, all three datasets were filtered with bandpass filtering from 300 Hz to 6000 Hz and spike sorted with a threshold of $\pm$ 6 μV. Figure 3.5 shows a ten-second spike train from Piphys with dots highlighting detected spikes in the raw data.

To further demonstrate the applicability of Piphys to primary neuron recording, we compare the shape of the detected action potential and quality metrics

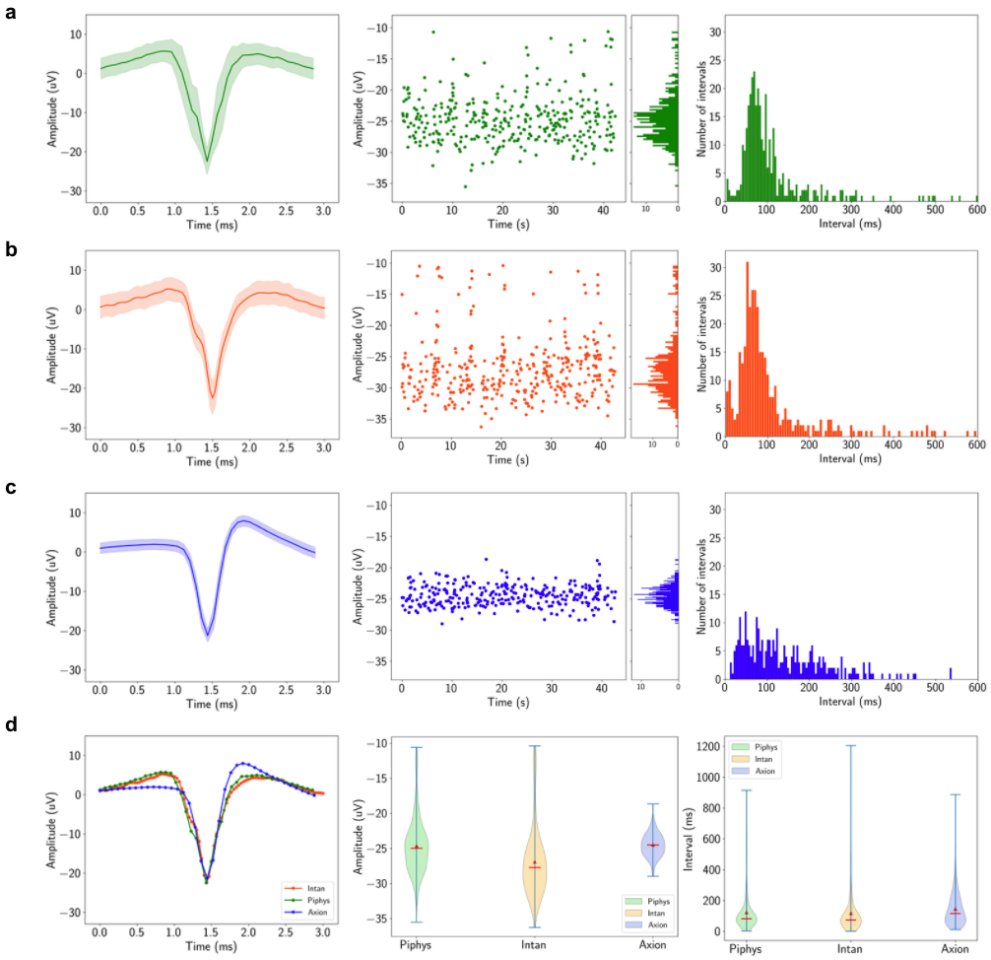

Figure 3.6: **Piphys performance is similar to commercial systems.** Spike sorting result for the same recording channel from Piphys, Intan RHD USB interface board, and Axion Maestro Edge. Shown from left to right are mean waveform with standard deviation (shaded area), amplitudes of the detected spikes over time, and interspike interval distribution. **(a)** Piphys **(b)** Intan RHD USB interface board **(c)** Axion Maestro Edge **(d)** Comparison of the mean waveform, amplitude, and interspike interval distribution from three systems.

such as amplitude distribution, interspike interval distribution, and firing rate to commercially available systems (Figure 3.6). The data was recorded from the same channel in the same well of neurons by Piphys, Intan, and Axion systems

in sequential order on the same day. The data recorded on Piphys corresponds to the data obtained from both commercial systems, with high similarity to Intan and overall consistency with Axion across metrics in Figure 3.6.

The mean spike waveform, shown in the first column of Figure 3.6, was determined by averaging the voltage in a 3 ms window centered around the point where the voltage crossed the spike threshold. Differences in Axion's waveform shape are a flatter starting point and a higher upstroke before settling to resting state. The amplitudes for the mean waveform are -24.67 $\pm$ 3.92 μV for Piphys, -26.92 $\pm$ 4.96 μV for Intan, and -24.50 $\pm$ 1.69 μV for Axion. Axion has a smaller deviation than Piphys and Intan, showing lower noise in the recording system.

The amplitudes of the detected spikes over time, shown in the middle column of Figure 3.6 are more sparse for Axion than for Intan and Piphys. Firing rates in events per second over the recording period shown are 8.05 for Piphys, 8.44 for Intan, and 6.86 for Axion.

The interspike interval histograms, shown in the middle column of Figure 3.6, have similar longer-tail distributions for Piphys and Intan centered at 122.79 ms and 118.15 ms, and a tighter distribution for Axion centered at 145.57 ms. However, the interspike interval means that all three systems are significantly close together.

The variation between Piphys and Axion could be attributed to physical dif-

ferences in the circuity and possible advanced filtering performed by Axion's proprietary BioCore v4 chip [1]. The filtering could account for the smoothness and low variability of the signal (measured 1.12 ± 0.18 μV RMS noise baseline), resulting in a smaller number of identified firing events with a tighter distribution. Piphys and Intan systems both use the same amplifier chips (Intan RHD2000 series), where the optional on-chip filtering was disabled during recording [2]. The raw signal, therefore, has a larger noise margin (measured 3.21 ± 0.66 μV RMS noise baseline for Intan, 2.36 ± 0.4 μV RMS for Piphys), which may create more false-positive firing events. The tail of the amplitude distributions in Intan and Piphys is skewed towards lower-amplitude events, closer to the noise floor. The interspike intervals for Intan and Piphys register several events with near-zero intervals, likely suggesting false-positive spikes from noise contamination. Contamination from noise, which is likely symmetrical, could affect the shape of the mean waveform calculated by overlaying and averaging all registered spikes.

Overall, these results demonstrate that Piphys can record neural activity in a manner comparable to commercially available hardware and software.

Detecting burst activity from primary neuron network

On day 42 of culture, we recorded from the neurons with Piphys and found the primary neurons displayed synchronized network bursts, consistent with previous

[1] https://www.axionbiosystems.com/resources/product-brochure/maestro-edge-mea-system-brochure

[2] https://intantech.com/files/Intan_RHD2000_series_datasheet.pdf

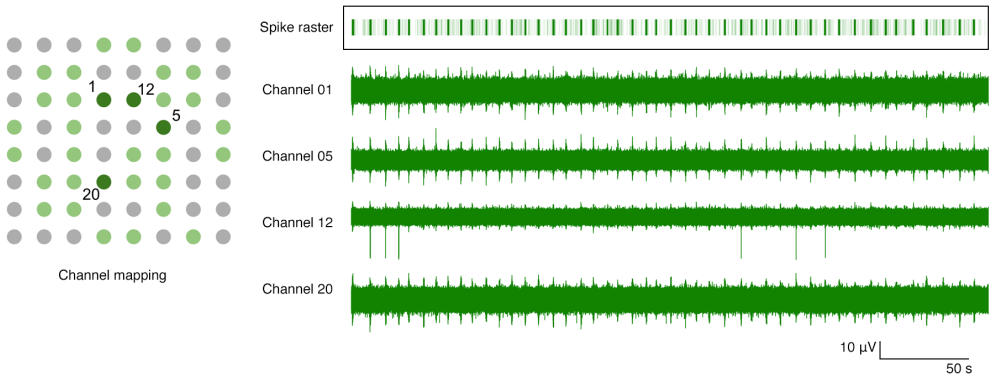

Figure 3.7: **Bursting activity across four channels with channel mapping.** Channel mapping shows 64 electrodes in well B2 of the Axion plate (detailed mapping in Figure B.1). Light green dots are the 32 electrodes recorded by Piphys. Dark green dots mark channels 1, 5, 12, and 20, whose raw recording plots are on the right. The spike raster superimposes all the detected spikes in the shown channels. Each light green vertical line in the raster indicates a spike, and the dark green bar results from superimposing multiple spikes in the burst. The bars in the raster plot align with the bursts throughout these four channels.

observations [247, 13]. Figure 3.7 shows the synchronous activity captured across four channels. After spike sorting, most detected spikes were arranged in short intervals with periods of silence in between. The spikes inside the bursts align among the channels, indicating that synchronized activity was present through the network. Quantitatively, the bursting has a general population rate of 0.13 bursts each second, with each burst lasting around 1 second. Within one burst, the number of spikes is 55 ± 17.58.

To further characterize Piphys system's performance, we compute the SNR of bursting activity by the following equation applied to the smoothed signal:

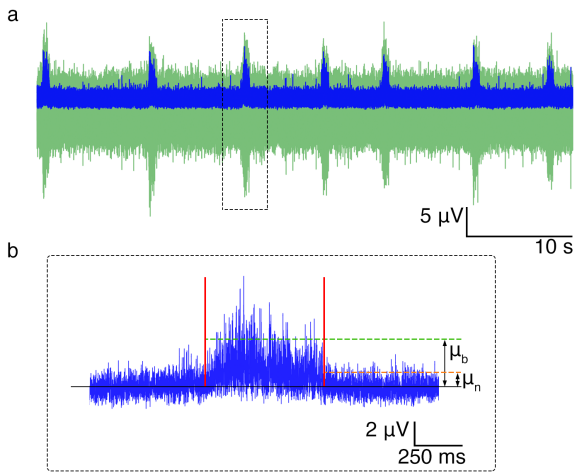

Figure 3.8: **Signal-to-noise ratio of a burst. (a)** Burst train (green) and the smoothed signal (blue). **(b)** Zoom in to the third smoothed burst showing means of the signal and the baseline noise for SNR calculation.

$$SNR(dB) = 20\log_{10}(\frac{\mu_b - \mu_n}{\sigma_n}) \tag{3.1}$$

where μ_b and μ_n are the mean for the burst and baseline noise, respectively, σ_n is the standard deviation of the noise. In Figure 3.8, background signal in green represents the original recording. The signal in blue is the smoothed product by boxcar averaging with a window size of three times the standard deviation of the original. The median SNR across active channels is measured at 4.35 dB. The mean for baseline noise in the burst recording is around 2.13 μV RMS, consistent with the noise measurement for the experiments described in the Performance section. These experiments further demonstrate that the Piphys system is sensitive and reliable in the relatively low amplitude neural signal recording range.

In addition, with its open-source, lightweight, and remote monitoring capability through the IoT, Piphys adds unique value in extracellular electrophysiology.

3.4.3 Discussion

Remote longitudinal recording of neural circuits on an accessible platform will open up many exciting avenues for research into the physiology, organization, development, and adaptation of neural tissue. Integration with cloud software will allow in-depth experimentation and automation of analysis.

The proof of principle for Piphys has been shown on 2D cultures. As experiments with other devices have shown, it should be applicable to measurements of 3D brain organoids, which are becoming an increasingly popular model for studying human brain tissue development and function [52, 120, 191, 213, 233, 204, 258].

Improvements to Piphys also include increasing sampling rate and precision of timing in between samples. Currently, the Raspberry Pi CPU samples the Intan RHD2132 bioamplifier chip, and the sampling rates are limited by the CPU's ability to multitask. Future solutions may involve adding another CPU or FPGA to the hardware shield. The platform will continue to be improved, and its modularity allows adapting hardware and software components as different needs arise.

The signal-to-noise ratio could be improved by enabling and tuning on-chip filtering and improving Faraday cage shielding. *In vitro* cultures typically fire

with amplitudes between 10 and 40 μV [206, 233, 159]. They demand sensitive recording equipment, as an increase of just a few μV in noise for spikes on the lower end of the spectrum can be considered a non-trivial variable.

Piphys software and hardware source files for building the Piphys system are available open-source on GitHub [3]. All files are provided 'as is' and end-users are encouraged to freely use and adapt the system for their own application-specific protocols.

Overall, the open-source Piphys design, programmability, and extreme flexibility of the Raspberry Pi significantly lowers the entry barrier of the electrophysiology system, providing an opportunity for broader applications in education and research.

3.4.4 Materials and Methods

Tissue source

De-identified tissue samples were collected with previous patient consent in strict observance of the legal and institutional ethical regulations. Protocols were approved by the Human Gamete, Embryo, and Stem Cell Research Committee (institutional review board) at the University of California, San Francisco.

Primary neuron culture

Prior to cell culture, the electrode surfaces of 6-well Axion plates (Axion

[3] https://github.com/braingeneers/piphys

Biosystems, CytoView MEA 6) were coated with 10 mg/mL poly-D-lysine (Sigma, P7280) at room temperature overnight. The following day, plates were rinsed 4x with water and dried at room temperature. Primary cells were obtained from human brain tissue at gestational week 21. Briefly, cortical tissue was cut into small pieces, incubated in 0.25% trypsin (Gibco, 25200056) for 30 minutes, then triturated in the presence of 10mg/mL DNAse (Sigma Aldrich, DN25) and passed through a 40um cell strainer. Cells were spun down and resuspended in BrainPhys (StemCell Technologies, 05790) supplemented with B27 (Thermo Fisher, 17504001), N2 (Thermo Fisher, 17502001), and penicillin-streptomycin (Thermo Fisher, 15070063), then diluted to a concentration of 8,000,000 cells/mL. Laminin (Thermo Fisher, 23017015, final concentration 50ug/mL) was added to the final aliquot of cells, and a 10uL drop of cells was carefully pipetted directly onto the dried, PDL-coated electrodes, forming an intact drop. The plate was transferred to a 37C, 5% CO2 incubator for 1 hour to allow the cells to settle, then 200uL of supplemented BrainPhys media was gently added to the drops. The following day, another 800uL of media was added, and each well was kept at 1 mL media for the duration of the cultures, with half the volume exchanged with fresh media every other day. The activity was first observed at 14 days in culture, and the second recordings were performed on day 42 of culture.

Circuit board design, reduction of noise and EMI

The printed circuit board was designed in Autodesk Eagle. The board has four layers of copper. The top and bottom layers of the board are GND, while the two layers inside are signal and power. Every signal via has a ground via next to it to sink EMI as signals switch layers. The layout of the circuit board is done in modules. Via stitching was done around the perimeter and throughout the board area to separate modules (highlighted by the colored rectangles in Figure 3.2) and fill in areas with no components. The amplifier chip and Raspberry Pi computer are separated by a cable such that noise from the computer would not interfere with the sensitive neural signal recording. During data acquisition, all of the electronics and biology were shielded by a 1 mm thick steel faraday cage.

Cloud services integration

We deployed servers and cloud computing platforms to achieve permanent data storage and messaging between the local device and the dashboard. The Internet of Things (IoT) service with MQTT messaging and device management was coordinated through Amazon Web Services (AWS). The dashboard was hosted on a server at UC Santa Cruz. We used Remote Dictionary Server (Redis) and Simple Storage Service (S3) were hosted on the National Research Platform (NRP) [223][4]. All services (except AWS IoT) are platform agnostic and can be hosted anywhere[5].

[4] `https://nationalresearchplatform.org/`

[5] Later in Chapter 5, AWS IoT was replaced by the combination of EMQX MQTT broker and Strapi shadows database to be cloud-provider agnostic.

Redis, real-time data stream Neuronal action potential recording with a high sample rate and multiple channels requires a high throughput pipeline to make real-time streaming possible. Remote Dictionary Server (Redis) is a good choice to implement this objective. It is a high-speed cloud-based data structure store that can be used as a cache, message broker, and database. Based on benchmarking results, Redis can handle hundreds of thousands of requests per second. The highest data rate for every push from Piphys system to Redis is 9.6 MB (32 channels $\times$ 15 kHz sampling rate $\times$ 16 bits/sample $\times$ 10 seconds), which can be satisfied with an internet bandwidth larger than 7.68 Mbps.

Internet of Things (IoT) communication

The dashboard is programmed to be an IoT device that sends Message Queuing Telemetry Transport (MQTT) messages to control and check the Piphys system. In response, the Piphys subscribes to a particular MQTT topic to wait for instructions. AWS IoT supports the communication of hundreds of devices, making the Piphys system's extension to a large scale possible in the future.

Simple Storage Service (S3)

The Simple Storage Service (S3) is the final data storage location. S3 is accessible from anywhere at any time on the internet. It supports both management from a terminal session and integration to a custom web browser application. After each experiment, a new identifier will be updated on the dashboard. When a

user asks for a specific experiment result, the dashboard can pull the corresponding data file directly from S3 for visualization.

3.5 Conclusion

The goal of making Piphys was to create a light-weight, low-cost electrophysiology system. The design has been received well by the DIY maker community and research labs that want to lower the cost of electrophysiology equipment[6]. Piphys also contributed to cloud-based Raspberry Pi-controlled laboratory suite alongside imaging and microscopy devices (Figure 4.6).

Future work would focus on supporting stimulation: optogenetic, electrical, or both. Section 6.4 describes an optogenetic stimulation module that can be integrated with Piphys. For electrical stimulation, adding an FPGA is necessary to support the communication rate with the Intan RHS chip and eliminate possible issues with sampling jitter during the increased frequency of data exchange with the Raspberry Pi. An onboard FPGA would also allow pre-processing signals and prototyping of on-chip spike sorting algorithms popular in the neuroengineering community [5, 169, 184, 230]. This could make Piphys a potential development board for the chip-based algorithms community.

Since the publication of Piphys, the field has moved towards using higher chan-

[6] `https://youtu.be/bEXefdbQDjw?si=XChktv_VtfWlq1i5&t=1412`

nel counts and higher spatial density despite the higher cost. Further experiments in this thesis use an HD-MEA system, which offers state-of-the-art technology in spatial density and channel count. HD-MEAs are important for discovering scientific phenomena at the cutting edge of resolution, while Piphys has a role in practical and educational projects.

Chapter 4

Internet of Things Cloud Laboratory

The following content in this Chapter 4 is adapted from the journal article published in Elsevier Internet of Things [173] co-first authored with David F. Parks, Jinghui Geng, Matthew A.T. Elliott. I helped influence the design choices for the IoT Architecture during its creation, drafted several of the figures in the manuscript, and helped co-write and edit all sections of the manuscript with the team.

4.1 Introduction

Cloud biology uses internet protocols to connect biological devices online. This allows live experiments to be monitored and controlled through a web application. Cloud biology has been suggested for the online control of high-throughput cellular biology [253]. A backbone of many cloud biology systems are small, inexpensive computing devices managed by a centralized server to control aspects of a biological experiment. In particular, Raspberry Pi computers have become a common device in many cloud biology experiments [100].

The Internet of Things (IoT) is a communication framework often used to manage multiple small devices to work in unison. IoT has become commonplace as a technology used in home sensors, distributed robotic factories, and personal wearables but is rarely used in cloud biology. The framework is designed for devices to be easily connected together and controlled through underlying messaging protocols like MQTT (Message Queuing Telemetry Transport).

IoT systems can provide many benefits to cloud-based biology experiments. IoT provides a standardized framework of communication that dramatically reduces the effort required to connect each device to the cloud and has been employed in lab automation [147, 17]. Fleets of devices can be controlled with negligibly more effort than controlling a single device because of the modular nature of the IoT framework. Live data streaming becomes possible using the same straight-

forward protocols as basic communication. IoT also provides its own method for instant notifications. This is particularly useful when an alarm notification should be sent to a scientist notifying their experiment is in danger [182].

This section introduces an IoT architecture for cellular biology, and demonstrates the architecture and its usage with laboratory benchtop experiments in electrophysiology, microscopy, and fluidics. The electrophysiology, microscopy, and fluidics devices were co-engineered by the authors of this IoT architecture. The devices use Raspberry Pi computers running similar software packages that are unified and simple to implement on new lab devices. Using this IoT system, scientists can have real-time control and monitoring of live experiments through an online web tool. Scientists can automate research and receive live updates on the health of experiments. This architecture benefits our research and would benefit other labs that implement similar functionalities.

The main contributions of this work are summarised as follows:

- Provide an architecture allowing numerous modalities of biological data collection (electrophysiology, microscopy, fluidics, and flexibility to add more) that can be monitored and controlled remotely.
- Outline a cost effective and scalable solution to expand the availability of cell biology experimentation, including an audience outside the exclusive environment of the lab.

- Define a system of communication and data storage infrastructure for managing and processing large scale laboratory datasets remotely and in a scientifically reproducible way.

4.2 System Design

Cost, scalability, maintainability, and scientific reproducibility were the fundamental requirements for our high throughput experimentation architecture. Low cost is made possible by cloud computing platforms offering affordable commodity computing and storage resources at supercomputer scales. Scalability and maintainability are achieved through IoT management of devices and software containerization of data analysis processes, which both offer plug-and-play approaches with minimal dependencies between components. Scientific reproducibility is embedded through standards-based workflow definitions using Nextflow and Dockstore.

Figure 4.1 depicts the high-level overview of the system. Data acquisition modules (devices) execute experiments in the lab. Each module performs a specific task, such as electrophysiology, microscopy, and fluid delivery. Users interact with the devices through a web-based user interface or a lower-level software API. The software API controls devices and enables any program to manage the flow of experiments. Logistics of device management, communication, and data storage

are handled through the National Research Platform (NRP, a nonprofit) and Amazon Web Services (AWS, for-profit)[1]. In the following sections, we describe each component of the architecture.

4.2.1 Device Management, Communication, and Control via MQTT

The data acquisition modules are lightweight and general-purpose IoT devices. The IoT devices connect to the services that support user control, data storage, analysis, and visualization via the MQTT (Message Queuing Telemetry Transport) protocol. MQTT is a well-supported, industry-standard publish-subscribe messaging protocol.

Figure 4.2 depicts MQTT's central role in coordinating communications between data acquisition modules and user interfaces. The MQTT protocol maintains the state and connection status for each device. It also provides a simple, lightweight publish-subscribe platform with defined *topics*. The *topics* are used by devices or user interface components to organize communication. There are two types of *topics*: a *topic* per each device (electrophysiology, microscopy, or any device performing experimental measurements or recording), and a *topic* per each running experiment. Each experiment is also assigned a UUID (Universally

[1]Later in Chapter 5, AWS IoT was replaced by the combination of EMQX MQTT broker and Strapi shadows database to be cloud-provider agnostic.

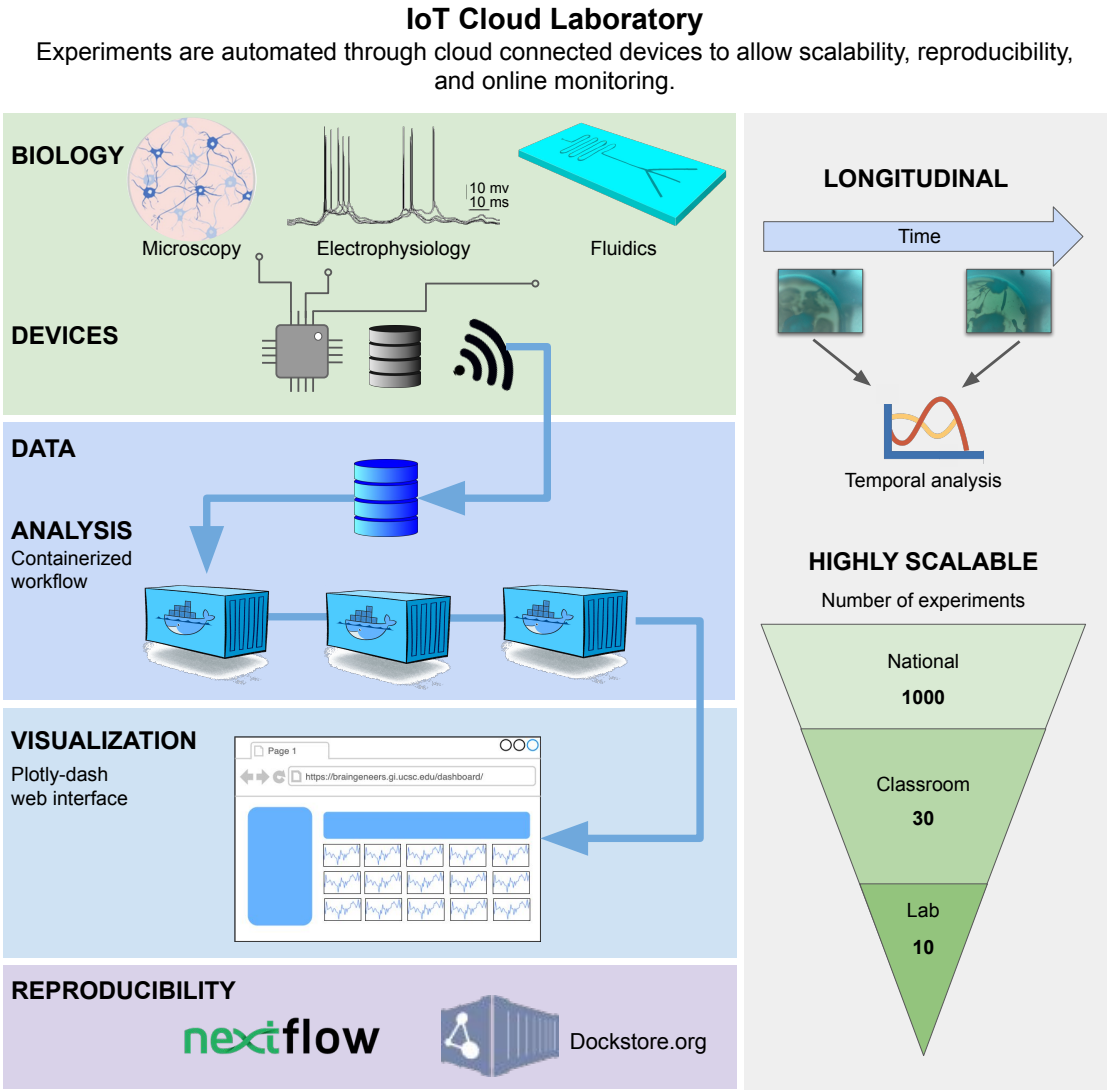

Figure 4.1: **IoT Cloud Laboratory**. Experiments are automated through cloud-connected devices to allow scalability, reproducibility, and online monitoring.

Unique IDentifier), which becomes an *active topic* for the period of operation.

An experiment starts when MQTT messages are published to the appropriate experiment and device *topics*. Devices subscribed to those *topics* receive the mes-

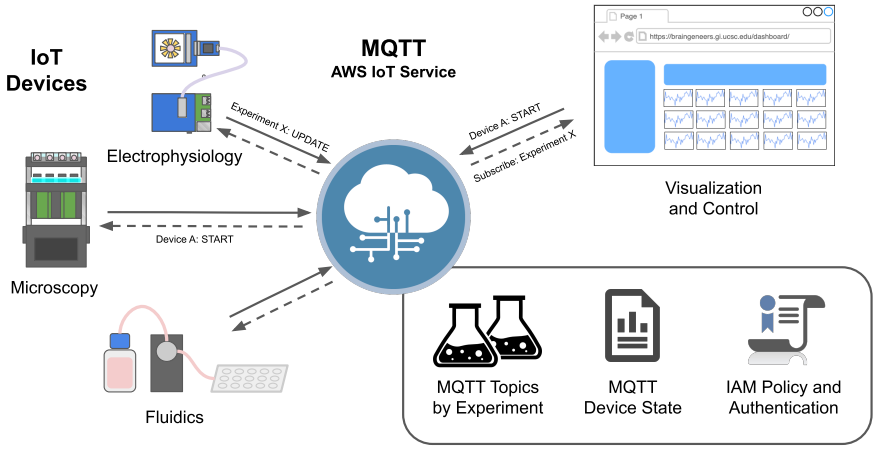

Figure 4.2: **Inter-device MQTT message broker.** The MQTT message broker provides integration and control over multiple internet-connected instruments. The functionality supports *clients*, data acquisition modules or software applications, to connect and subscribe to topics set by a *publisher*, such as the user interface (UI), with the proper authentication protocols. By doing so, *clients* subscribed to the topic will be informed of the state of each data acquisition module (e.g., start, stop, etc.) and parameter changes throughout an experiment.

sages and take the appropriate action. Actions can also be taken automatically based on sensor readings. For example, a temperature sensor that detects overheating can publish an emergency stop message to the appropriate devices and turn this device off. Actions may involve sending users alerts explaining errors or requesting intervention.

Chapter 5 and Appendix D further elaborate on the use of MQTT messaging between devices, and how it is used to conduct experiments.

4.2.2 Data Storage via Ceph/S3

Figure 4.3 shows how devices store experimental data. Primary storage and data processing are implemented on the NRP through a distributed commodity compute cluster based on Kubernetes and the Ceph [252] distributed file system. Ceph provides a highly scalable S3 interface to a virtually unlimited data store. Ceph/S3 is the primary storage for all datasets, from small to terabyte-scale, commonly recorded by electrophysiology, microscopy, and fluidic assays. Our larger parallelized data processing tasks have peaked at over 5 GB/sec of concurrent I/O from S3, demonstrating the substantial scalability of the file system. Access to the Ceph/S3 data store is universally available online, making it an excellent place to share large datasets across institutions.

As a research-oriented compute cluster, the NRP (National Research Platform) does not provide strong SLAs (Service Level Agreements) for the data store. Network outages due to local network, power, or user error can cause temporary service disruptions. No guarantee is made against data loss, though the Ceph filesystem provides mechanisms to guard against common failures such as losing a node or storage media. We mitigate against data loss by scheduling a Kubernetes Cron Job with a nightly backup of all data from Ceph/S3 to AWS Deep Glacier, a cloud IaaS (Infrastructure as a Service) service providing a long-term tape storage solution. Also, all data-producing edge devices maintain a local cache that can

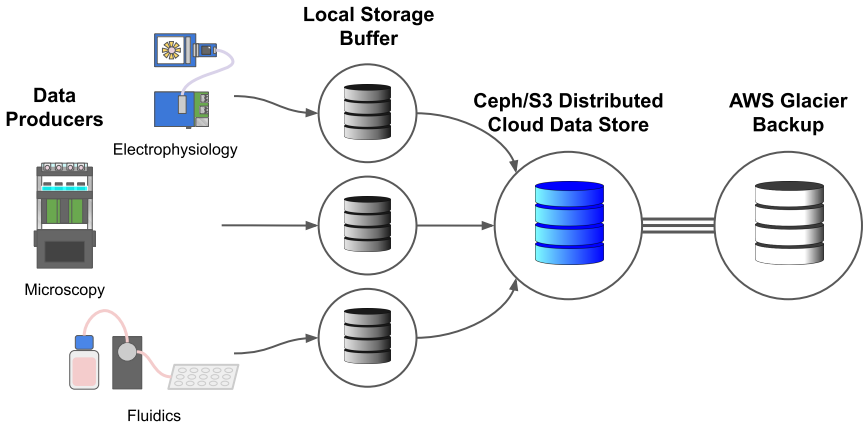

Figure 4.3: **Data storage architecture.** Data storage is buffered to the local device before being delivered to cloud S3 storage. Network and cloud service disruptions are expected. With the real-time data feed, interruptions only impact active visualizations of the data, which is acceptable, but the loss of experimental data is not. Each device buffers data to its local storage before making a best-effort attempt to upload it to the S3 distributed object store. Data may be buffered until the local storage is exhausted (typically enough for at least a day). The S3 distributed store is backed up to AWS Glacier to guard against user error (accidental deletion) and the loss of the S3 service. Cloud providers like AWS, GCP, and Azure have strong S3 service level agreements, unlike academic clusters such as the NRP.

withstand a temporary service disruption.

4.2.3 User Interface via Plotly Dash

A Plotly Dash[2] interface is easy to develop and code in Python, a common language for data science. Plotly offers rich interactive plotting functionality, including specialized biology-focused visualizations. Dash provides a template to build user interfaces that implement the Observer Design Pattern [62], making for

[2]https://plotly.com

an extensible and maintainable environment.

A Plotly Dash web application provides a user interface and visualizations for each lab device (see the "Visualization and Control" in Figure 4.4). This topic will be further discussed in the "Results and Discussion" section (Figure 4.6 "Control"). The web application can plot data from past experiments saved on Ceph/S3 or publish MQTT messages to the device or experiment *topics* in real-time. Figure 4.6 and Section 4.3.1 show how a user visualizes a "Piphys" electrophysiology device streaming data.

4.2.4 Data Streaming via Redis

Real-time streaming and real-time feedback are facilitated through a Redis service. Redis is a high-speed database that can be an inter-server and inter-process communication service. It is straightforward to interact with Redis using many languages, including Bash, Python, and C. Raw data feeds are sent to Redis only when the user is actively interacting with a data stream. For example, when looking at a real-time visualization, the UI client sends MQTT keep-alive messages to keep the data stream active. While MQTT is appropriate for small messages, Redis is the primary communication method for larger data blocks.

Figure 4.4 introduces a mechanism for handling large-scale real-time data streams. Redis provides common data structures with the inter-process locking

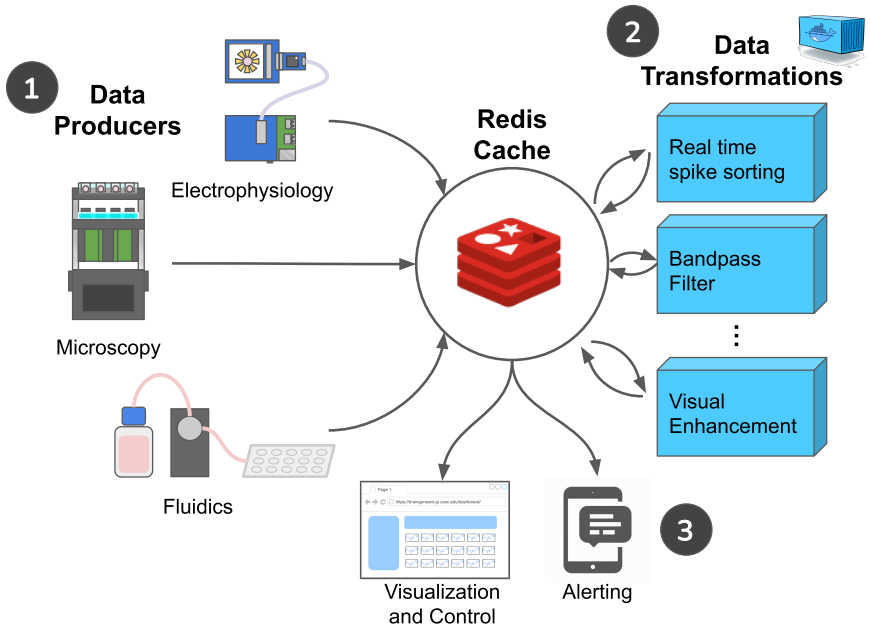

Figure 4.4: **Real-time data visualization.** (1) Electrophysiology, Microscopy, and Fluidic IoT devices produce real-time data streams on-demand only when a user is connected to a visualization that utilizes that stream. (2) Data transformations process raw data into a variety of helpful forms. Each independently containerized transformation reads a data stream and produces a new data stream. (3) Visualization and alerts notify IoT devices via MQTT that data streams are needed.

required to coordinate services running on separate devices. It provides a way for data producers to publish a real-time stream of data, such as an electrophysiology recording, and for a consumer of that data, such as the Plotly Dash UI, to coordinate with each other without direct dependencies between them. Data transformations using Redis shown in Figure 4.4 are discussed in Section 4.2.6. A Redis stream is effectively a queue that can be capped in length so that old data is automatically dropped once the maximum size of the stream is reached.

Consumers, such as the Plotly Dash website, can send a recurring MQTT message to the relevant data producer to start the data stream and read the data as it is produced. A Redis service interruption merely pauses data visualization. The data producers stream a raw data feed to Redis in real time while logging data in batches to Ceph/S3. The Ceph/S3 object store remains the primary source for data storage, and the data transfer to Ceph/S3 is resilient to service disruptions. There is no guarantee against data loss in the streaming approach, which is why Ceph/S3 is the primary datastore, and the Redis stream is reserved for visualizations that can incur service interruptions without lasting consequences.

4.2.5 Data Processing with Containers and Workflow Definitions

Longitudinal electrophysiology, microscopy, and fluidic experiments combine commonly created datasets on the multi-terabyte scale. Big data analysis is performed using containerized workflows built with Docker and Kubernetes and deployed using Nextflow. Large-scale machine learning especially relies on S3 for reading terabyte-scale datasets. Data analytics tasks such as neural voltage signal analysis, machine learning, and image analysis require substantial computing resources and processing in multiple stages.

Containerization is used in the infrastructure to provide substantial compu-

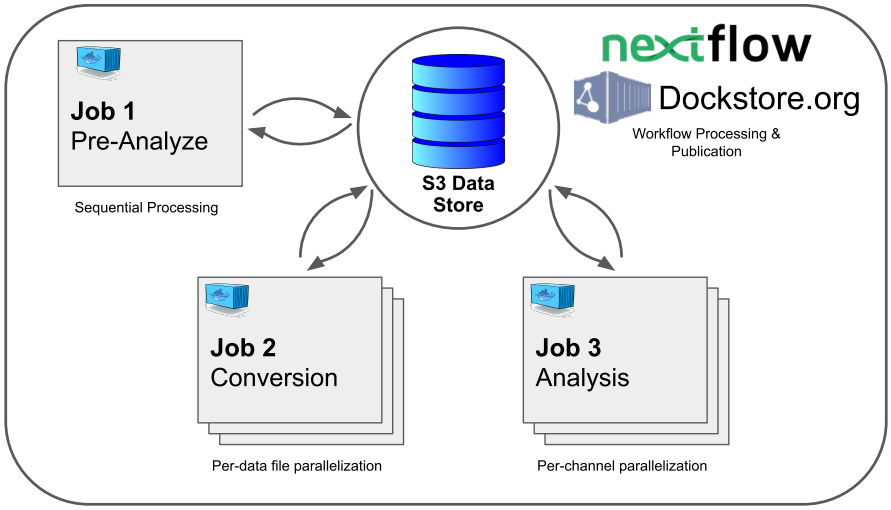

Figure 4.5: Example data processing workflow for an electrophysiology experiment. In Job 1, a subset of the data is analyzed to determine which channels are active. Next, in Job 2, raw data for each active channel is converted into the form necessary for data analysis (this step takes advantage of cluster parallelism, splitting tasks by data file). Finally, in Job 3, the data analysis, including spike sorting and other custom analysis tasks, is performed in parallel per active channel.

tation power and resources with simple cloud management. This is a method of packaging code and all its dependencies into a virtual environment so an application runs reliably in any computing environment. Containers are efficient and lightweight, they share a single host operating system (OS), and each container acts as an independent virtual machine without additional overhead (unlike full hypervisor virtual machines, which replicate the OS). The container can be uploaded to a repository (for example, on Docker Hub), downloaded, and run on any computer. This includes servers in a cluster or a local lab computer.

We introduced Dockstore.org [164] in our design as the next logical step in scientific reproducibility, building on containerization technology. Dockstore.org is a

website dedicated to hosting containerized scientific workflows. The formal definition of a workflow is the execution of repeatable computational or data manipulation steps, such as inputs, outputs, dependencies and the containers they run on. A common workflow language formalizes a containerized software process to ensure that organizations can run each other's software in a standards-compliant manner. Several formal workflow definition languages exist: Nextflow [48], Common Workflow Language (CWL) [6], and Workflow Description Language (WDL) and are all supported by Dockstore.

Besides being a formalized workflow language, Nextflow provides a workflow runtime engine capable of deploying containerized processes to various platforms such as Kubernetes, AWS, Google Cloud, and Azure. Figure 4.5 depicts a standard electrophysiology data processing workflow developed and run on Nextflow and deployed to the Kubernetes-based platform on the NRP. All workflows receive a standard UUID (Universally Unique IDentifier) pointer to a dataset, allowing the workflows to find the raw or preprocessed data produced by a dependent workflow.

4.2.5.1 Example Workflow for Processing Electrophysiology

A canonical workflow for an electrophysiology experiment is to detect the action potentials (spikes) of neurons by analyzing voltage recordings on multiple channels and producing standardized reports. This is part of a larger procedure called "spike sorting". The workflow consists of 3 Jobs that occur in stages: (1)

channel scan, (2) data conversion, (3) spike sorting and analysis.

In stage (1) of the workflow, the electrophysiology data is scanned to identify active channels. A JSON file with active channel information is recorded to Ceph/S3. This step requires a single task/container to run. In stage (2) of the workflow, the dataset is converted from its raw 2-byte integer-based data format into a 4-byte floating-point data format. This data transformation is performed in parallel on the cluster using multiple containers, each processing a single data file from the multi-file dataset. The original data file is downloaded locally, converted, and uploaded to a temporary location on Ceph/S3. Data is further separated into individual channels for efficient analysis during this process. Note that the conversion process must fully download and re-upload the dataset because multi-terabyte datasets are too large to fit on a single server. Finally, stage (3) of the workflow pulls the metadata from stage 1 and the converted data files from stage 2. The converted data is first processed using spike sorting algorithms, such as MountainSort [39] and Kilosort [226]. Then spike timing analysis is performed using the spike sorting output files. Spike sorting performs a preprocessing curation step akin to denoising protocols implemented in neural EEG data [1]. The results are placed back on the Ceph/S3 distributed filesystem.

Each dataset has a unique ID (UUID) which also serves as a location pointer to where data is stored on Ceph/S3. This UUID is the only parameter passed

between jobs. Besides the UUID, separate data analysis jobs remain fully independent, relying only on the availability of the appropriate input data on Ceph/S3. A focus on independent units of code facilitates long-term software maintainability. Besides the example illustrated in this section, Figure 4.7 shows a more general overview of resources employed and parallelization of the data processing by workflows, including imaging and fluidics.

4.2.6 Real-time Analysis, Data Processing, and Transformations

Deploying containerized workflows via Nextflow works well for large-scale post-processing and data analysis but does not provide a mechanism for real-time visualizations and experiment control.

The Redis in-memory database service coordinates the real-time exchange of data in *streams* between many producers and consumers. For example, an electrophysiology recording on 32 channels at 25 kHz will produce a data stream of 1.6 MB/sec, which a user may want to monitor in real time. Equivalently, a microscopy recording produces a stream of images for visualization.

Data transformation with visual enhancements applied in real-time is often more informative than seeing raw data. Data transformations are performed by containerized processes that read a stream of data and write a new stream of

transformed data. For example, a container reads a raw electrophysiology stream and writes a new stream with the bandpass-filtered data. After applying the data transformation, a visualization such as a Plotly Dash web page would read the appropriate data stream output. Data transformations have no dependencies other than the Redis stream they read from and can be entirely independent workflows. Transformations can easily be added or changed without changing any other software infrastructure components.

4.3 Results

For the results of the IoT architecture, we will focus on a case study analysis of various devices using the platform and an example of how the platform would scale with these devices under different consumption models.

4.3.1 Case Study Analysis

This software architecture supports different modes of data acquisition that measure and report data. Here we focus on three types of modules for proof of concept: (1) Electrophysiology – voltage recording and stimulation of neural cell cultures, (2) Microscopy – imaging of cell cultures, (3) Fluidics – feeding cells and sampling media for metabolites and RNA expression using a programmable microfluidics system. These modules are implemented and described in separate

publications and presented in Figure 4.6.

We will look at each of these data acquisition modules (IoT-based edge devices) and discuss how they interact with the software architecture and user. For this example, we assume users will interact with devices through the web UI application. Users can be located anywhere on the Internet without concern for the location of these physical devices. This facilitates cross-campus and cross-institutional collaborations. For instance, we often perform electrophysiology and microscopy experiments from Santa Cruz on devices located 90 miles away in San Francisco. Of course, experiments still require some manipulation by a researcher at the local site (i.e., placing cell cultures on the devices and performing adjustments if components are misaligned).

To begin an electrophysiology experiment, a user opens the browser with the Plotly Dash web application (Figure 4.6, Control). The application queries AWS IoT service[3] for online electrophysiology devices (Figure 4.6, Devices). The device can be Piphys [244] or any platform/recording system whose computer runs the same code that responds to the IoT architecture and can control the system programmatically. When the user selects a device, an MQTT 'ping' message is sent to the relevant device every 30 seconds, indicating that a user is actively monitoring data from that device. As long as the electrophysiology device receives

[3]Later in Chapter 5, AWS IoT was replaced by the combination of EMQX MQTT broker and Strapi shadows database to be fully cloud-provider agnostic.

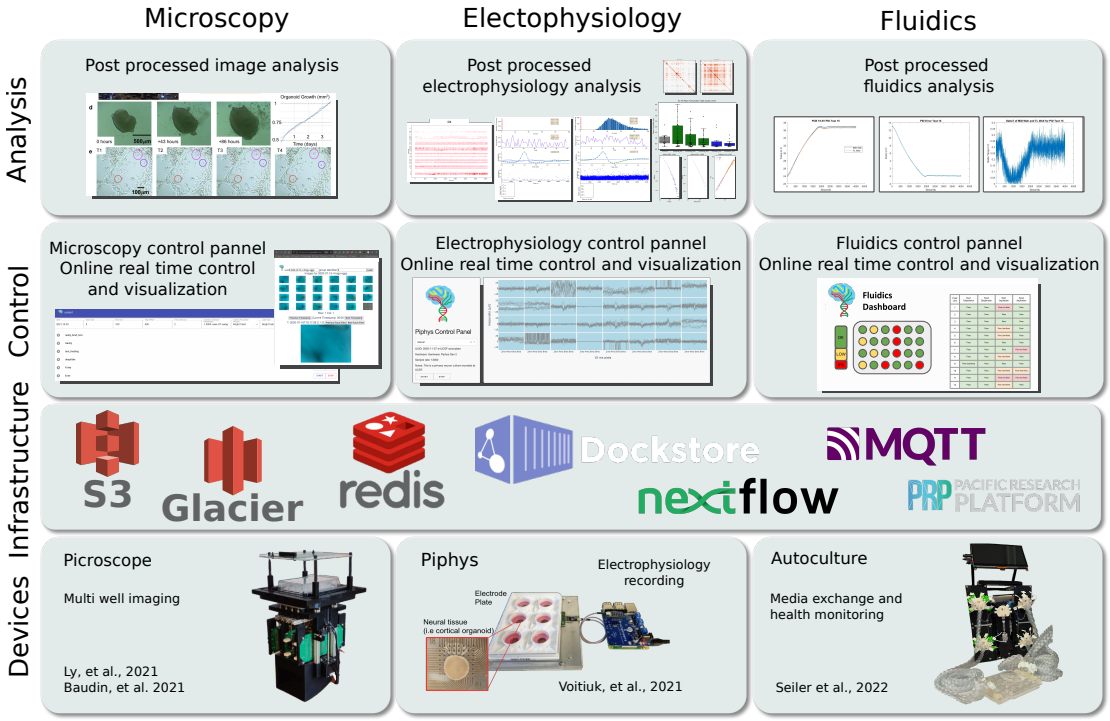

Figure 4.6: **An outline of existing tools that utilize the IoT Cloud Laboratory platform described in this paper.** (Device) shows Picroscope [134, 18] for microscopy, Piphys [244] for electrophysiology recording, and Autoculture [210] for fluidic media exchange and liquid biopsy. (Infrastructure) shows the primary suite of tools introduced in Section 4.2.2, 4.2.4 and 4.2.5. (Control) shows a snapshot of existing web-based control interfaces. These web pages are running on a server in the UCSC Genomics Institute. (Analysis) demonstrates some of the reports produced by workflows that run as data post-processing jobs. "Picroscope" and "Piphys" figures are adapted from [134, 18] and [244].

these pings, it will send raw data to its Redis stream (Figure 4.6, Infrastructure). Since the device is responsible for only a single data stream, many users can monitor and interact with the particular device without additional overhead. If the device has not received user messages for at least a minute, it will cease streaming its data. This protocol ensures the proper decoupling of users from devices, and devices are not dependent on a user, gracefully shutting down the connection.

As shown in Figure 4.4, one or more data transformation processes can read the raw data stream and post a processed stream of data, such as real-time spike sorting. The web visualization can display the appropriate transformed data stream for the user (Figure 4.6, Control).

Stopping the experiment will automatically initiate a batch processing workflow on the Kubernetes compute platform. Users can configure the workflow to include job modules such as spike sorting, clustering, and other customized metrics of neural activity.

Microscopy, such as the Picroscope, typically operates at a lower sampling rate and over a longer continuous period than electrophysiology. Microscopy devices record images of cell culture morphology at varying focal layers and time intervals. As with electrophysiology, these images are initially buffered locally and then flushed to the Ceph/S3 filesystem every few minutes. A user will view the data

in the same web UI portal as electrophysiology. Since cell culture morphology changes relatively slowly, microscopy visualizations do not require real-time Redis streaming. The user may update the parameters of the microscopy recording with MQTT messages sent to the device *topic* updating the state.

Fluidics devices support the lifecycle of the cell culture, providing new media and taking regular measurements relevant to the cell culture's health and environmental state. Much like microscopy, most of these measurements are sampled continuously over the lifetime of the culture and are posted directly to Ceph/S3 at regular time intervals. When the user accesses a UI page detailing the feeding and liquid biopsy sampling of the culture, these metrics will be pulled in near real-time from Ceph/S3. The user can update and change metrics by an MQTT message from the UI page to the device which updates its state and initiates a change in device behavior.

Current usage metrics for experiments are listed in Table 4.1.

4.3.2 Scaling

In the previous section, we considered one experiment with a few data acquisition modules running in a single lab (Figure 4.6, Table 4.1). This section considers hypothetical studies of tens to thousands of experiments operating simultaneously. Each use case will employ a varying set of features of the devices. We define three

	Microscopy	**Electrophysiology**	**Fluidics**
Device in the laboratory	Picroscope [134, 18]	Piphys [244]	Autoculture [210]
Number of experiments	130 UUIDs ∗	139 UUIDs ∗	10 plate runs (2,400 individual wells)
Currently stored data	6.5 TB and 2.9 million images (time series z-stacks)	8.5 TB voltage data (sample rate at 12-20 kHz)	<1 GB feeding logs, MetaFLEX data
Required network speed (Mbps/active experiment)	0.27	1.6	0.0027
Data storage rate (GB/active experiment/hr)	72	4140	0.72
Analysis on dataset	Auto subject edge detection	Spike sorting	RNA-seq analysis

Table 4.1: Data and metrics from IoT experiments conducted in the IoT Cloud Laboratory. ∗ Each unique experiment receives a UUID

use cases and provide an analysis of these and their assumptions. These use cases are called: Science, Student, and National. We provide a distribution over the basic functions and devices that we expect the users will employ in each case. For each case, we provide estimates of CPU, Network, and Storage resources required, visualized in Figure 4.7. Also provided in Figure 4.7 is an estimate of cloud computing and storage cost based on AWS pricing. The use of the NRP academic compute cluster precludes the majority of these costs and speaks to the value the

NRP brings to academic institutions.

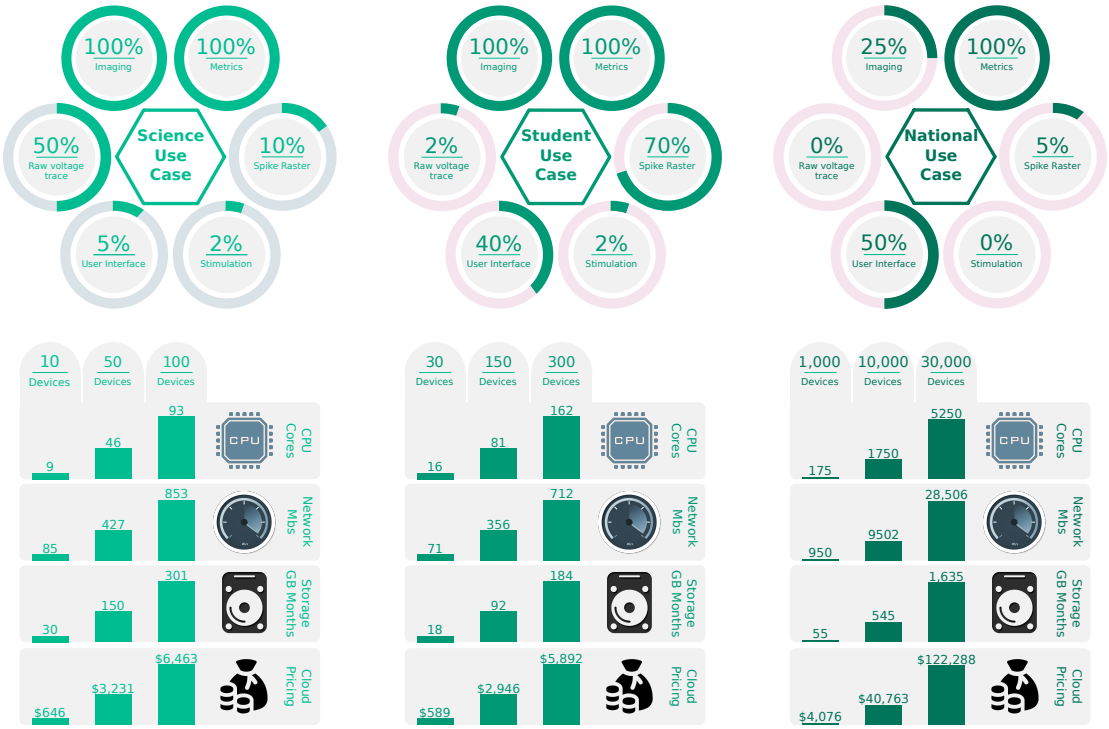

Figure 4.7: **Monthly resource utilization requirements given three use cases: Science, Student, and National scales.** The assumed distribution of device functions under each use case is displayed in circular gauge charts above. Resource utilization for CPU, network and storage are displayed in bar graphs below. An estimate of Cloud Pricing is provided at the bottom. The number of active devices varies from fewer devices in the Science Use Case to many in the National Use Case. We define "% Imaging" as the percentage of devices actively recording and storing microscopy images; "% Metrics," as the percentage of devices actively recording measurements such as media concentrations and temperatures; "% Raw voltage trace," as the percentage of devices recording and storing full raw voltage traces across all electrophysiology channels; "% Spike Raster," as the percentage of devices registering only neural spikes events (estimated to be 10% of the raw voltage data); "% User Interface," as the number of active users on the web interface relative to the total number of devices; and "% Stimulation," as the percentage of devices that are actively executing electrode stimulation requests.

In the Science use case, we assume a higher degree of active imaging and

electrophysiology. This use case focuses on more resource-intensive lab use in the pursuit of scientific inquiry in great detail. In this configuration, storage requirements are the most significant bottleneck, growing at tens to hundreds of GB of data per hour. We find that tens of devices are appropriate for this use case before resource utilization becomes excessive.

In the Student use case, we anticipate a limited number of universities using the devices to teach classes in cell biology on live cultures hosted at a remote lab. In this use case, we assume a scale on the order of hundreds of devices. Users in this scenario will rely heavily on visualizations, including both real-time microscopy and electrophysiology. The lab that hosts hundreds of experiments with the expectation of concurrent access will require additional network bandwidth beyond what is available in a typical lab or office. At least two Gigabit network ports and matching ISP bandwidth would be necessary to support the load. At this scale, if electrophysiology is involved, limiting data that is sent over the wire to active spiking events rather than raw signal measurements is imperative. This requires on-device spike detection.

Lastly, in the National use case, we consider a scaled-out fleet of thousands to tens of thousands of devices. This case assumes wide-scale adoption by laboratories or secondary education facilities across the country or world. This scale requires substantial cloud computing resources to support the load and serve mi-

croscopy images and electrophysiology data to every user. It will also require significant wet lab infrastructure at the site(s) housing the biology as well as expenses of cell culture maintenance. However, given this investment, this infrastructure can enable remote experimentation by a large and diverse population.

4.4 Materials and Methods

4.4.1 National Research Platform

The National Research Platform is an academic compute cluster run by the UCSD Supercomputer Center. It is described as a "potluck supercomputer," hosting and consolidating computing resource components of a large scale across many academic institutions. Compute resources are organized in public and private areas of the cluster. If a lab or institutions hosts compute resources on the cluster, they can choose to limit access to those resources, make them cluster-wide public, or make unused compute available for cluster-wide use. Most academic institutions can access the cluster's public resources via existing integration with CILogon. Institutions also benefit from hosting existing resources with the NRP cluster by taking advantage of the automated cluster administration and existing DevOps team. The cluster currently hosts over 7000 CPU cores, 500 GPUs, 35 TB of memory, and 2.5 PB of storage, as well as accelerator devices such as FPGAs.

4.4.2 Workflow Management

Docker, Kubernetes, Nextflow, and Dockstore are employed as workflow management tools. Docker enables a Container (effectively a virtual machine with less overhead) to be packaged with all software and configuration in a binary package that does not require re-installation to run on a new machine. Kubernetes is an industry scale scheduler for Docker Containers, which is hosted by the NRP. Nextflow provides standardized workflow definitions, which are stored and distributed on the Dockstore website.

4.4.3 Data Management

Large-scale data transfer and storage are achieved using a Redis server for real-time data transfer and Ceph distributed filesystem deployed on the NRP cluster. Redis is free open source software that enables distributed computing and high bandwidth data transfer. Ceph is a distributed filesystem that provides an S3 interface. The S3 interface is compatible with AWS/S3 standard but is not exclusive to Amazon services. Tools such as the AWS command line tools and Rclone can be used to access Ceph via the same interface as defined by AWS. The reason an S3 filesystem is valuable is that it is a scalable internet-accessible data store; therefore, data can be easily accessed by anyone with the appropriate credentials, within a lab, or between labs and institutions.

4.4.4 Message Queuing Telemetry Transport (MQTT)

For IoT, Raspberry Pi devices comprise most edge computing infrastructure, and they communicate over the MQTT protocol using the AWS IoT implementation of MQTT and related IoT services. Raspberry Pi devices are registered on the AWS IoT service and communicate over the publish/subscribe MQTT protocol.[4]

4.4.5 Frontend

On the frontend, Plotly/Dash is employed for real-time visualizations, and Jupyter Hub is employed for data analysis and data visualization tasks. Plotly/Dash is a web-hosted extension to the open-source Plotly plotting library, providing programmatic and real-time interaction with data for visualization purposes. Jupyter Hub provides a hosted Jupyter Notebook environment in which data analysis takes place. These services are hosted on a local lab server; they interact with the NRP/S3 for access to data and Redis and MQTT for communication with the cluster and real-time data.

[4]Later in Chapter 5, AWS IoT was replaced by the combination of EMQX MQTT broker and Strapi shadows database to be cloud-provider agnostic.

4.5 Conclusion

This paper outlines an IoT software architecture that supports the control and analysis of electrophysiology, microscopy, and fluidics on cell cultures. We emphasize the benefits of having a centralized online hub where automated experiments are managed through a portal. Scientists benefit from notifications on their experiments' status and monitor the progression without perturbing samples. Our architecture is built on an open-source design with scientific reproducibility in mind. Future advances in IoT architecture for cell biology may open new possibilities to scale high-throughput experiments, which benefit drug screens, gene knockout studies, and a host of other applications. This architecture example is intended to be generalized to other experiments and lab devices to further advance the implementation of IoT in cellular biology.

Chapter 5

Feedback-driven Electrophysiology, Fluidics, and Imaging Integrated System

The following content in this Chapter 5 is adapted from the bioRxiv pre-print article [245] undergoing journal submission, co-first authored with Spencer T. Seiler. I apply the IoT Cloud Laboratory paradigm in Chapter 4 to generalize a fleet of devices, requiring the design of a software *device-class* and a messaging convention on top of MQTT. Spencer and I both ran the experiments and collected data, drafted figures, and helped co-write and edit all sections of the manuscript with the team.

5.1 Introduction

Recently, advances in biological research have been greatly influenced by the development of organoids, a specialized form of 3D cell culture. Created from pluripotent stem cells, organoids are effective *in vitro* models in replicating the structure and progression of organ development, providing an exceptional tool for studying the complexities of biology [107]. Among these, cerebral cortex organoids (hereafter "organoid") have become particularly instrumental in providing valuable insights into brain formation [52, 120, 186], function [64, 7], and pathology [66, 129]. Despite their potential, organoid experiments present significant challenges. Brain organoids require a rigorous, months-long developmental process, demanding substantial resources and meticulous care to yield valuable data on aspects of biology such as neural unit electrophysiology [148], cytoarchitecture [222], and transcriptional regulation [129].

The primary methods for generating and measuring organoids depend on media manipulations, imaging, and electrophysiological measurements [177], which are all labor- and skill-intensive, limiting the power and throughput of experiments [244]. Cell culture feeding and data collection occur at intervals realistic for researchers. Furthermore, during manual feeding and data collection, the cell cultures are removed from the incubator, which provides a controlled gas, temperature, and humidity environment [23]. Ideally, feeding should be aligned with

the cells' metabolic cycles, and data should be collected at intervals on par with the biological phenomenon. The disturbance incurred by leaving the incubator environment is shown to increase metabolic stress and batch-to-batch variability, potentially impacting the quality of the experiment [250], as well as increasing contamination risk. These limitations hinder the depth of insights gained from these organoid models, particularly in studies focused on dynamic neural processes and disease modeling [177].

Laboratory robotics, most often liquid handling devices [113], offer increased precision and throughput but are primarily designed for pharmaceutical screens, limiting their adoption in research labs due to high costs, large footprints, and inflexible workflows [232]. Moreover, many of these systems lack the ability to seamlessly integrate new technologies as they emerge. Conversely, academic research labs are benefiting from advancements in commercial and custom-made technologies, facilitated by in-house fabrication methods like 3D printing [248, 137], which are enhancing their capacity to manipulate and measure biological systems. However, without an easy-to-integrate, device-agnostic robotic platform, researchers are constrained to manual operations, restricting the power and scope of their experiments. By outfitting devices to carry out automated jobs and relay data through communication networks, they acquire around-the-clock functionality and increased fidelity [89]. The flexibility in size (number of devices per integrated sys-

tem) allows researchers to optimize for the experimental design and budget. Implementing programmable feedback loops derives precision and self-optimization by dynamically adjusting to real-time data [221, 114, 37], offering a practical alternative to complex mathematical modeling for experiment control. This approach would enable more integrated, flexible automation in research settings, broadening the scope and efficiency of experiments.

Automating multiple devices to report data presents a challenge for device management and communication, necessitating flexible and efficient infrastructure. Addressing this need for an interconnected ecosystem of devices, services, and technologies is possible through designing networks using standards defined by the Internet of Things (IoT). This approach has already impacted wearables [178], agriculture [30], city infrastructure [228], security [202], and healthcare [108]. It was recently proposed to expand this approach to biology research [175]. Previously, each researcher built a custom device and code from scratch with unique assumptions for communication and behavior. Each device operated in solitude, lacking integration and feedback with other devices. Here, we establish a platform that addresses these challenges, combining electrophysiology, microscopy, microfluidics, and feedback control, automated and integrated through IoT technology for touch-free, in-incubator tissue research.

5.2 System Design

5.2.1 Integration

We have developed an integrated platform (Figure 5.1) that automates organoid culture and data collection in individual microenvironments. While microfluidics (Figure 5.1A) controls the media environment, digital microscopy captures the morphogenic features. The neural activity is recorded by local field potential measurements using complementary-metal-oxide semiconductor (CMOS) high-density microelectrode arrays (HD-MEA)[156](Figure 5.1B). The IoT cloud network brokers the communication between all devices and facilitates data storage, processing, and presentation services including an interactive webpage (Figure 5.1D). Through touch-free automation, samples remain undisrupted in the incubator, increasing the consistency of images and allowing for higher frequencies of feeding and recording.

At user-defined intervals, conditioned media is aspirated by a syringe pump through a system of distribution valves (Figure 5.1A), stored in a collection reservoir (without passing through the syringe pump vial (Figure 5.1C), and replaced by an equivalent volume of fresh media. Both types of media are perfused through flexible fluorinated ethylene propylene (FEP) tubing at 110 mm/s, which leads to low shear forces [210] (see Materials and Methods, Organoid Culture Using

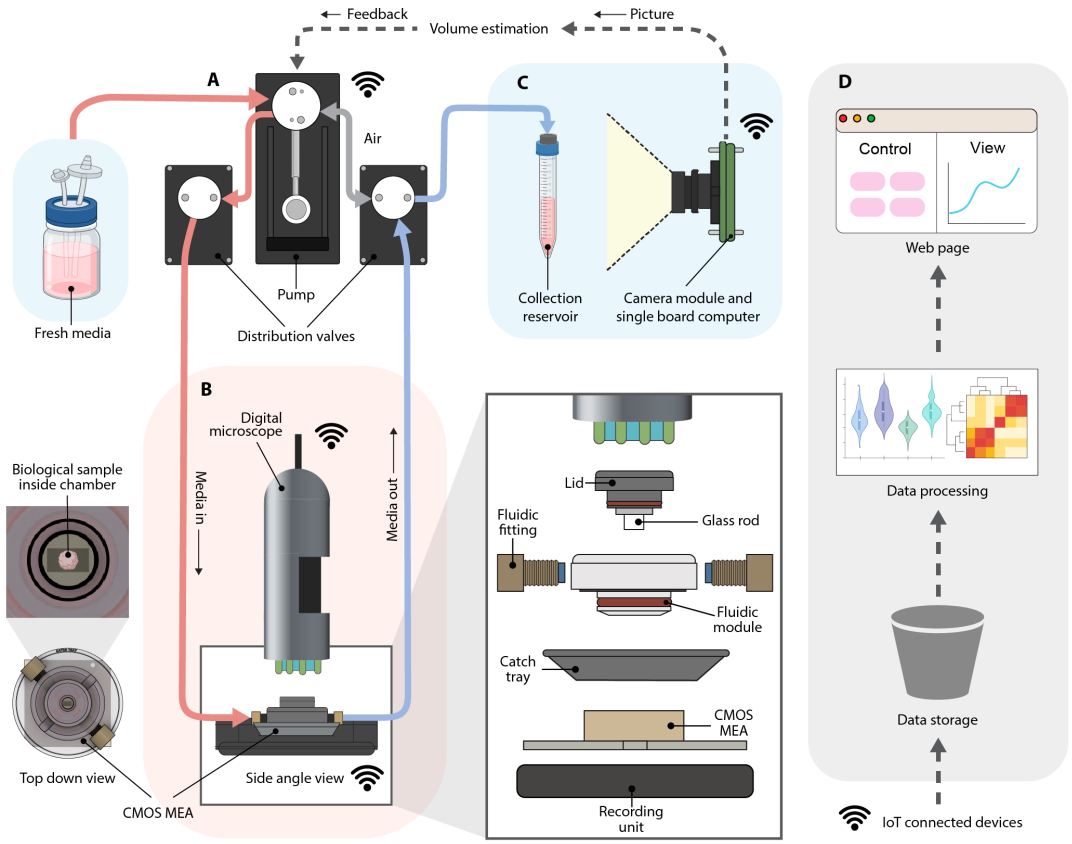

Figure 5.1: **Schematic diagram of the integrated feedback platform.** **(A)** A syringe pump and valve system dispense fresh media and aspirate conditioned media at user-defined intervals. The blue background represents 4°C refrigeration. **(B)** In-incubator microscopy and HD-MEA electrophysiology unit for automatic recording, media exchange. Exploded view: the 3D printed gasket-sealed culture chamber. The red background represents 37°C incubation. The microfluidic culture chamber has an access lid with a polished glass rod viewing port, a gasket-sealed microfluidic module with threaded microtube fluidic fittings, and an overflow catch tray. The microfluidic culture chamber attaches to the HD-MEA, which houses the sensor for recording electrophysiology signals. **(C)** The in-refrigerator camera captures images of aspirated conditioned media drawn from each culture for volume estimation feedback to the syringe pump system. **(D)** Devices communicate over MQTT (Message Queuing Telemetry Transport) protocol and automatically upload data to the cloud, where it is stored, processed, and presented on a web page.

Automated Fluidics).

The digital microscope (Figure 5.2A) is attached using 3D-printed parts on aluminum posts. The 3D printed culture chambers integrate the microfluidics and HD-MEAs. A liquid-impermeable O-ring gasket ensures media retention inside the chamber. The well lid includes a polished glass rod submerged in the media, improving image quality and removing the effects of condensation. Alignment grooves in the glass rod lid prevent rotation and incorrect fitting. The lid exchanges gas with the incubator conditions through ventilating air ducts (Figure 5.2C), similar to a cell culture well plate. The removable and re-attachable lid reduces manufacturing complexity and enables future use of other lids with applications beyond imaging.

Figure 5.2C shows the cross-section of the culture chamber attached to the HD-MEA. The media flows in (red) and out (blue). The sinuous media path and well geometry ensure minimum disturbance to the biological sample [210]. Fresh media is delivered on top of the volume present in the chamber, similar to partial media changes found in manual feeding protocols [45, 251]. The ideal operating range is between 350 to 700 µL (see Figure C.1 and Table C.1 for numerical volume limits). In the case of over-aspiration, media drops to a minimum of 170 µL before aspirating air from the chamber's headspace. The 3D-printed catch tray guards against overflow, collecting up to 1.5ml (200% of the chamber's capacity)

to protect the recording equipment from liquid damage.

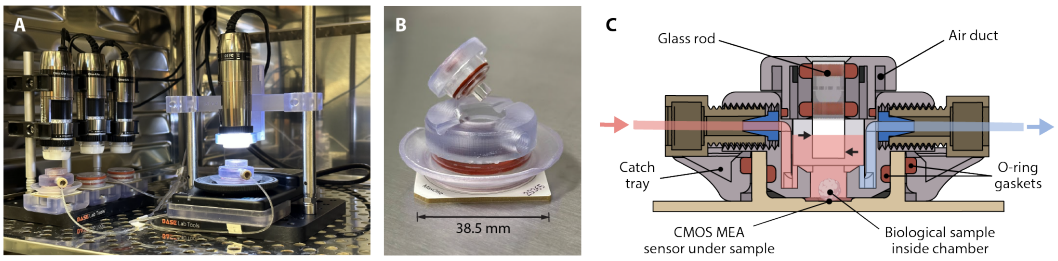

Figure 5.2: **The microfluidic culture chamber. (A)** The experimental setup inside an incubator shows two microfluidic culture chambers and two conventional membrane lids. **(B)** 3D printed culture chamber attached to the HD-MEA. **(C)** Cross-section showing the fluid path. Fresh media (red) enters the chamber, filling the internal cavity. Conditioned media (blue) is drawn out of the chamber. The media level, noted by the upper black arrow (559 µL) and lower black arrow (354 µL) on the glass rod, is the ideal operating range that keeps the rod immersed in media. The biological sample is adhered to the HD-MEA in the bottom of the cavity.

5.2.2 Computer Vision for Microfluidic Flow Feedback

We developed a computer vision volume estimation system to monitor the accumulation of aspirated media and identify anomalies during culture feeding events. Figures 5.3A and 5.3B provide a detailed view of the setup inside a refrigerator, which includes three main components: a collection reservoir support system, an LED panel, and a camera module (see Materials and Methods, Assembled Devices and Custom 3D-printed Components). The camera module remains on standby for image capture requests made by other IoT devices or users. Upon request, computer vision techniques are employed to estimate the media volume

within the reservoirs accurately.

Figure 5.3C shows the computer vision process (see Materials and Methods, Fluid Volume Estimation Using Computer Vision) for segmenting area related to the media in the reservoir. A calibration was required to establish the relationship between the segmented area in pixels and volume in milliliters. We captured 184 images of the collection reservoirs containing volumes of media ranging from 0 to 12 mL (several pictures for each volume), with each volume confirmed by a scale, accurate to 1 µL. For each specific volume in Figure 5.3D, multiple points overlap and are all accounted for to calculate the polynomial regression lines. To accommodate the reservoir's conical section (volumes <1.5 mL) and cylindrical section (volumes >1.5 mL), two distinct regressions were applied, ensuring a high degree of precision for each geometrical shape.

A Leave-One-Out cross-validation (LOO) [166] approach was employed to quantify the model's error. This method tests the model's accuracy and generalizability in an unbiased manner, ensuring that the calibration results in a model that performs reliably across different samples. The effectiveness of the model is assessed quantitatively with the following metrics: an average Mean Absolute Error (MAE) of 0.56% (equivalent to 27 µL), an average standard deviation of errors at 0.53% (22 µL), and an average Root Mean Square Error (RMSE) of 0.77% (35 µL). The polynomial models exhibit R-squared values of >0.99, denoting an

optimal fit of pixel area to liquid volume. Figure 5.3E shows the average absolute error percentage at a specific volume, with the bar indicating the error range from minimum to maximum.

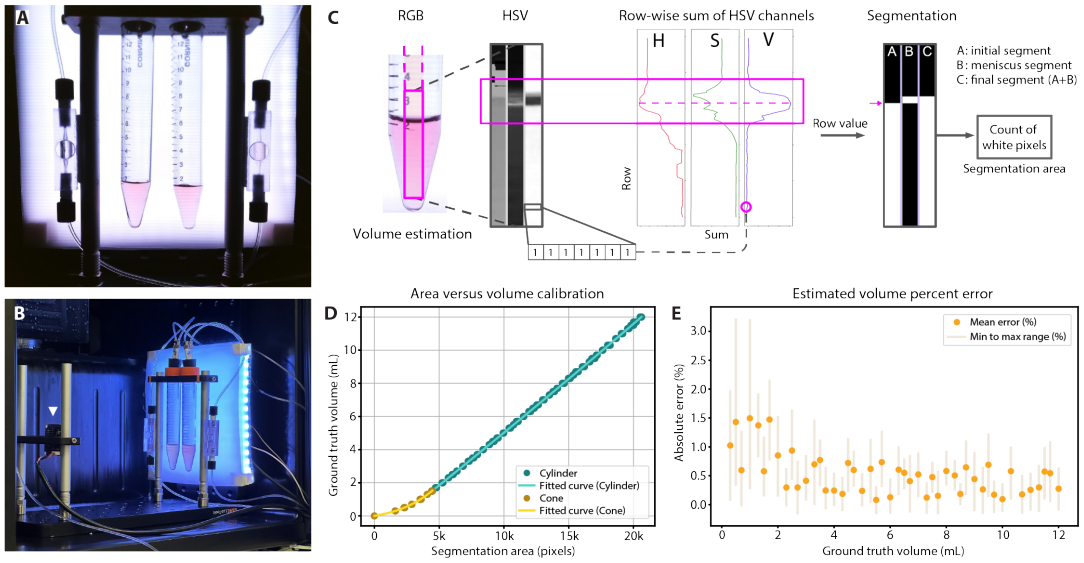

Figure 5.3: **Computer vision for volume estimation.** **(A)** Example of a raw image captured by the camera module. **(B)** In-refrigerator volume estimation setup. The CMOS camera module (the white triangle) images the conical tubes with a diffused LED backlight for even illumination. **(C)** Fluid segmentation: a rectangular pixel patch down the center of the conical tube; Row-wise summations of the HSV channels are used to detect the location of the meniscus. The initial liquid potion segmentation is added to the meniscus portion to yield the final segmentation. **(D)** Calibration graph with a fitted relationship of segmented pixel count to ground truth volume. **(E)** The absolute error percentage: orange dots represent the average error at selected volumes. The shaded bar represents the minimum to maximum error range.

5.2.3 IoT Ecosystem of Devices and Cloud-based Services

We built a cloud-based IoT ecosystem that enables communication between users, devices, and services to implement actions, record data, and streamline upload, storage, and analysis. All devices (here: pumps, microscopes, and microelectrode arrays) run software using the *device-class* Python framework (Figure 5.4A and Appendix D). Devices operate collectively with shared core software and complementary behaviors: they can request jobs from each other, yield during sensitive operations, and ensure collaborative functions and smooth operation (Figure 5.4D). Devices update their *shadow* in the database whenever their state information changes (i.e, assigned experiment, schedule, current job and estimated completion time, and other dynamic variables) to eliminate the need for device polling. Messages (i.e., job requests) between devices and services are sent through a centralized MQTT broker via the publish/subscribe protocol. This decoupled architecture allows for independent and extensible deployment of components. Data generated by devices is immediately uploaded to an S3 object storage in a predefined structure using an experiment Universally Unique IDentifier (UUID) as the top-level key. A 'metadata.json' file stores experiment details, sample information, notes, and an index of the produced data. Raw data is stored separately from analyzed data under different sub-keys. Cloud jobs, which operate as shared services, process raw data from S3 and write results back to S3, reporting status

via MQTT messages. To utilize the IoT ecosystem, users initiate experiments, control devices, and visualize data through a website (see Materials and Methods, Website and screenshots in Supplemental Figure D.1), with the typical user workflow in Figure 5.4C.

5.3 Results

The integrated research platform was used to study the effects of automation on the neuronal activity of pluripotent stem-cell-derived mouse cerebral cortex organoids. Embryonic stem cells were aggregated, patterned, and expanded to generate organoids using a previously defined differentiation protocol [53, 171]. Day 32 post-aggregation, 10 organoids were plated two-per-chip directly onto five HD-MEAs. For the 7-day study, the five chips were split into groups that were fed and recorded with standard manual procedures (Controls 1-3), automatic feeding and manual recording (AF), or automatic feeding and automatic recording (AFAR). Four chips (Controls 1-2, AF, and AFAR) were imaged in the incubator every hour, by their dedicated upright digital microscope (DinoLite).

Automated microfluidic feeds were used to increase the consistency and frequency of cell culture media replacement. We removed conditioned cell supernatant from the well and dispensed the equivalent volume of fresh media for each feed cycle. The controls had 1.0 mL media replacement every 48 hours, consistent

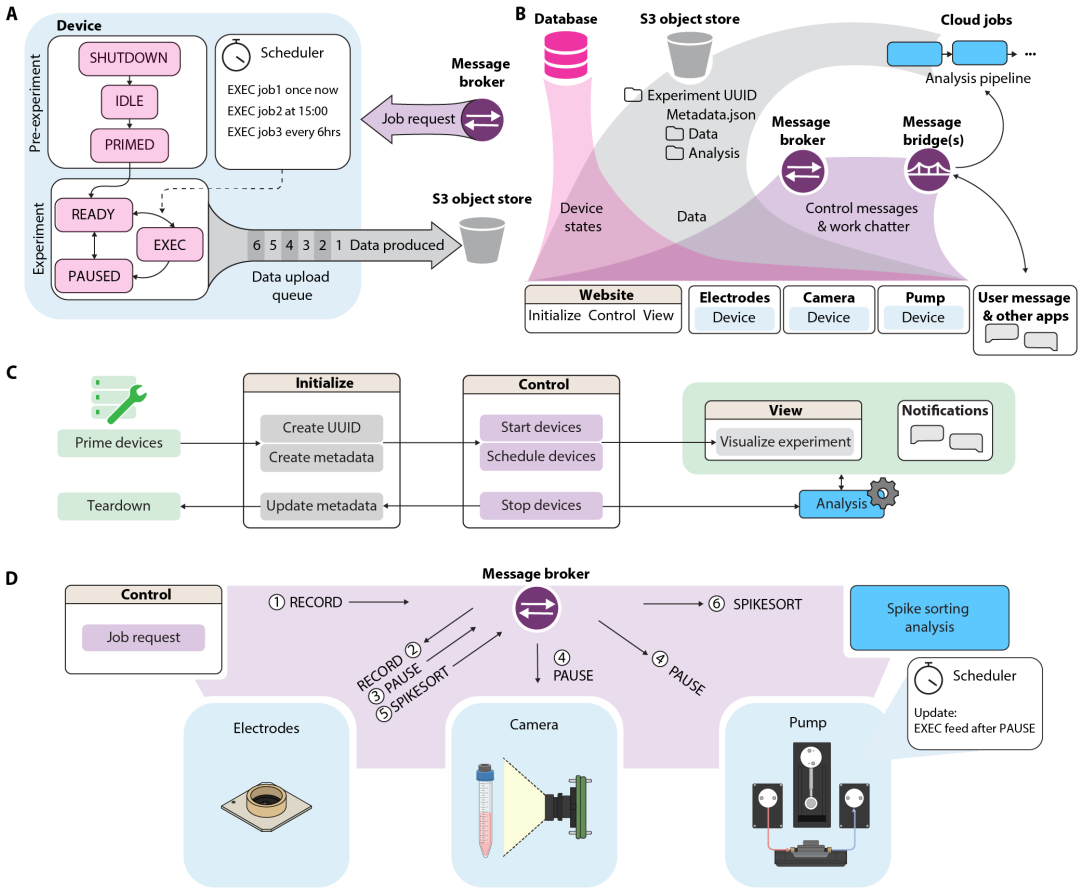

Figure 5.4: **Cloud-based device interactions. (A)** The *device-class* framework represents IoT devices as state machines, handling job requests, scheduling and executing tasks, and producing data for cloud storage. *(B)* IoT infrastructure: Device states are stored in a database and displayed via the website UI, while device-generated data is saved in cloud storage for access by the UI or analysis jobs. Communications are managed by a message broker, with message bridges connecting to analysis pipelines or text messaging apps. **(C)** User workflow. **(D)** Example inter-device communication: (1) A RECORD request is initiated; (2) the message broker delivers it to the recording unit; (3) the recording unit pauses other devices; (4) all devices receive the pause request; the pump reschedules a feed until after the pause; (5) after recording, the unit triggers data analysis.

with standard protocols. AF and AFAR were placed on a protocol in which 143

µL media were replaced every 6 hours, matching the total media volume turnover

across groups for the 7-day study. The schedule of automated media feeds was defined at the experiment's launch and initiated by a timed feeding job command sent to the microfluidic pump. The fidelity of feeding was controlled through a computer vision volumetric feedback loop on the aspirated conditioned media (Figure 5.3, 5.5A).

Conditioned media has a high protein content, contains cellular debris, and is susceptible to forming salt crystals [36, 132]. In microfluidic systems, this leads to clogs, error accumulation, and failure modes [122]. To overcome this, a volume estimation feedback loop was initiated each time the pump performed a job. Once media was perfused to/from a specific well, the pump sent a job request to the camera module responsible for imaging the well's collection reservoir. The image was captured, uploaded to the cloud, its volume estimated by the computer vision Estimator, and returned to the pump for feedback interpretation. Within tolerance, the action was declared a success (marked as a green check mark in Figure 5.5A), and no further action was taken. Outside of tolerance, the pump scheduled itself a new job proportional to the volume discrepancy and in relation to the number of previous feedback attempts (see Materials and Methods, Feedback Interpreter).

The system strives to resolve discrepancies on its own using feedback. However, in extreme cases where volume estimation returns a value outside of reason (i.e.,

> expectation + 2 mL) or if the feedback iteration limit is reached (i.e., > 20 attempts), the system was programmed to send an alert to a Slack messaging channel and pause. During the 7-day experiment, the system resolved errors independently, and this condition was not reached.

The automated feeding and feedback results for AF and AFAR are visually represented in Figure 5.5B-D. Figure 5.5C shows the traces of expected volume and computer vision estimated volume for AFAR (left) and AF (right) for the 7-day study (Days 5 to 12 post-plating). There was a collection reservoir change on Day 8 in which the 15 mL conical was replaced with a fresh tube. In both samples, the drop in estimated and expectation reflects the collection reservoir exchange. For AFAR (Figure 5.5B, left), a zoomed-in view of the feedback loop following the scheduled feeding cycle at 7:12 on Day 9 highlights feedback actions taken to remedy a volumetric discrepancy. In this instance, the volume estimation was less than expected after the feed cycle. Five consecutive aspiration jobs were carried out, and the estimated volume still remained under expectation. At the 6th iteration of feedback, a pull job was sent to the pumps, which raised the collection volume above the expected volume. In the 7th and 8th iterations of feedback, two dispense jobs were engaged to supplement the well for the over-aspiration. In a similar case, for AF (Figure 5.5B, right), a total of 6 iterations of feedback were engaged to bring the estimated volume into tolerance with the expected volume;

however, in this example, no dispense jobs were required. Figure 5.5D shows histograms summing pump events each day by subcategory. Each feeding cycle (four per day) was scheduled, and all other events occurred through feedback.

5.3.1 Manual Organoid Care was Reproduced with Automation

To interrogate organoid neuronal activity, extracellular field potentials were measured using 26,400 electrode HD-MEAs, which can record up to 1,020 electrodes simultaneously. We conducted daily activity scans to monitor neural activity. Heat maps derived from the first and final activity scans for each sample are presented in Figure 5.6B, with organoid body outlines for reference. To optimize electrode coverage, we generated specific configuration files for electrode selection based on the regions with the highest activity, which remained constant for four of the five chips. In one case (AF, Day 32+6), we adapted the configuration due to the emergence of a new high-signal area on the second day of recording. These maps allowed continuous electrode measurements for 10-minute intervals optimized for frequent, long-term sampling.

Manual recordings involved an experimenter placing each HD-MEA on the recording unit and initiating 10-minute recordings via software. In contrast, the hourly recordings (AFAR) featured the HD-MEA remaining on the headstage

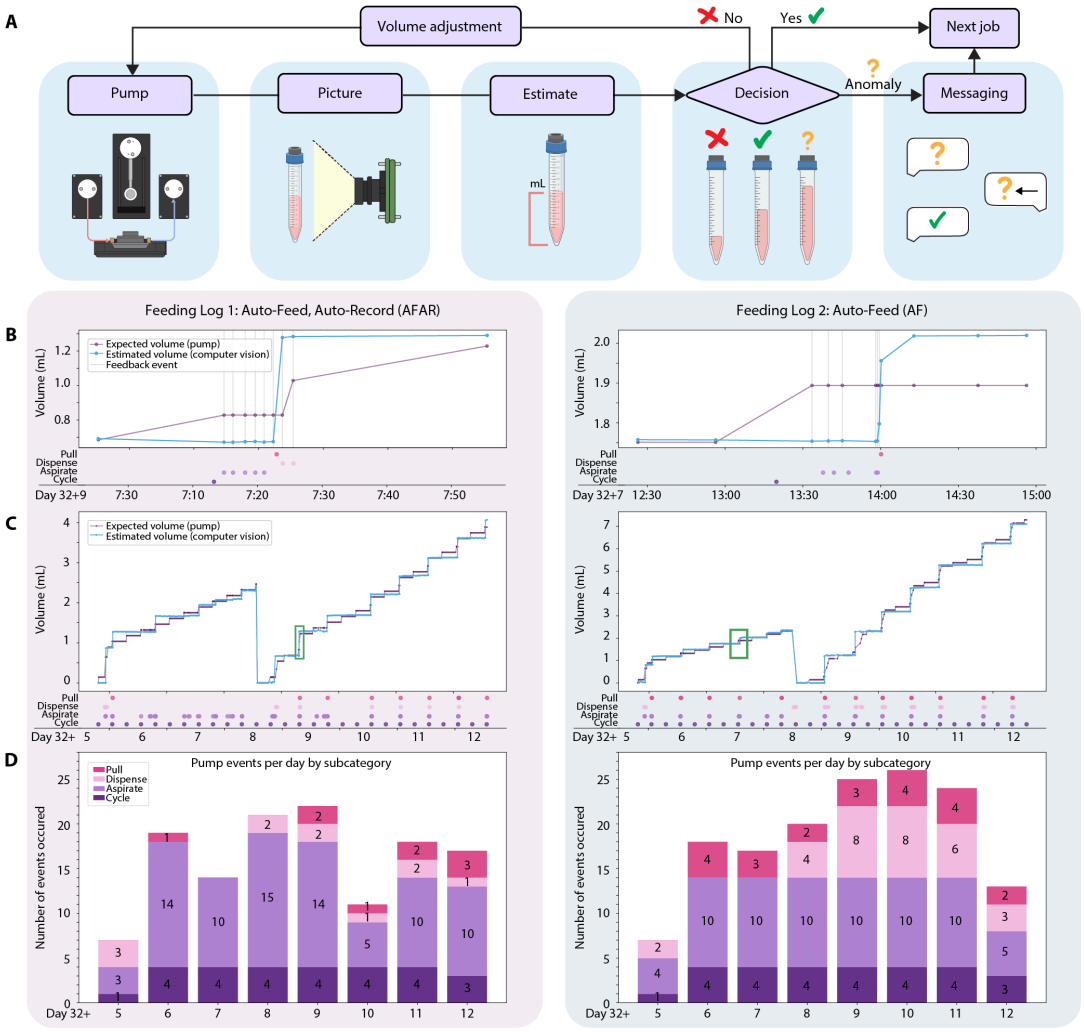

Figure 5.5: **Volume Feedback. (A)** Feedback loop for volume estimation: After a pump action, a camera captures the media reservoir image, and computer vision estimates the volume. Results are compared to the expected volume, leading to a decision: within tolerance (green check), adjustment needed (red "x"), or anomaly detected (yellow "?"). If within tolerance, the cycle ends; otherwise, an alert is sent. **(B-D)** Timeline summary and volume data: Organoids were plated on Day 32; automation began 5 days later and continued until 12 days later. Microfluidic event history, including feedback, is tracked underneath each volume plot. **(B)** Expected vs. estimated volumes during feedback events. **(C)** Volume traces over 7 days. **(D)** Histogram of daily pump events by type.

while automated software handled the entire process, from power management to data uploading. AFAR amassed 161 recordings, totaling 26.8 hours (560 GB) of electrophysiology data. Conversely, all manually recorded samples (Controls 1-3 and AF) accumulated 7 recordings, amounting to 1.2 hours of electrophysiology data.

From these data, we analyzed the effects of our automated microfluidic, imaging, and recording system on the neuronal activity of the brain organoids housed therein. Imaging of the chips from above (Figure 5.6A) allowed us to align the body of the organoid with neural units detected (Figure 5.6B). In some instances, such as in Control 1, neurite outgrowths were evident in the images and activity scans.

The initial activity scan was used to assign samples for the experiment. In the first activity scan, AFAR and Control 1 exhibited the highest activity, followed by AF, Control 2, and lastly, Control 3. This specific categorization of samples was designed to address potential biases introduced by varying levels of starting activity. To ensure robust analysis, each chip was treated as an average of the two organoids. Chips demonstrated similar trajectories in the number of units and firing rate frequency over the 7-day experiment, irrespective of feeding or recording schedules (Figure 5.6C-D). Figure 5.6C shows the distribution of neuronal firing rates as a violin plot for each chip over seven days, labeled with the number of

neurons detected in that recording. The number of detected units had a positive correlation over the 7-day study for all samples except Control 1, which also presented the highest number of units (Figure 5.6D, top). Similarly, the median firing rate was positively correlated with time for all samples except for Control 2 (Fig 5.6D, bottom). The fully integrated system, encompassing automated feeding, imaging, and recording, behaved like the controls, indicating minimal bias or distortion of data as a result of increased HD-MEA recording frequency.

5.3.2 Dynamic Neuronal Activity States in Organoids

The hourly recording condition (AFAR) unveiled dynamic and transient states, not apparent with single daily recordings (Figure 5.6E). While the trendlines for hourly and daily recordings (for both units and firing rates) have similar upward trends, hourly recordings show more prominent oscillations around the trendline not captured by the single daily recordings. Median firing rates fluctuated as much as 3-fold over the course of a day, sometimes within a few hours of each other.

To determine if feeding cycles influenced this activity, we aligned recordings to a six-hour 'time since feed' cycle (Figure 5.6F, top) and examined potential differences in the number of units and firing frequency. Figure 5.6F presents the composite graph of aggregated neuronal firing rates comprising 26 feeding

cycles with all 161 recordings binned with respect to their time since feeding. Our results showed no trend across all superimposed feeding cycles: neither the number of units nor firing rate changed in relation to feeding cycles. The oscillations presented in Figure 5.6E do not align with feeding and appear to be a temporal dynamic intrinsic to the network. In summary, these findings underscore the robustness and reliability of our feedback-driven microfluidic platform for brain organoid studies.

5.4 Materials and Methods

5.4.1 Embryonic Stem Cell Culture

All experiments were performed in the adapted C57/BL6 mouse embryonic stem cell (ESC) line (Millipore Sigma # SF-CMTI-2). This line is derived from a male of the C57/BL6J mouse strain. Mycoplasma testing confirmed lack of contamination.

ESCs were maintained on Recombinant Human Protein Vitronectin (Thermo Fisher Scientific # A14700) coated plates using mESC maintenance media containing Glasgow Minimum Essential Medium (Thermo Fisher Scientific # 11710035), Embryonic Stem Cell-Qualified Fetal Bovine Serum (Thermo Fisher Scientific # 10439001), 0.1 mM MEM Non-Essential Amino Acids (Thermo Fisher Scientific #

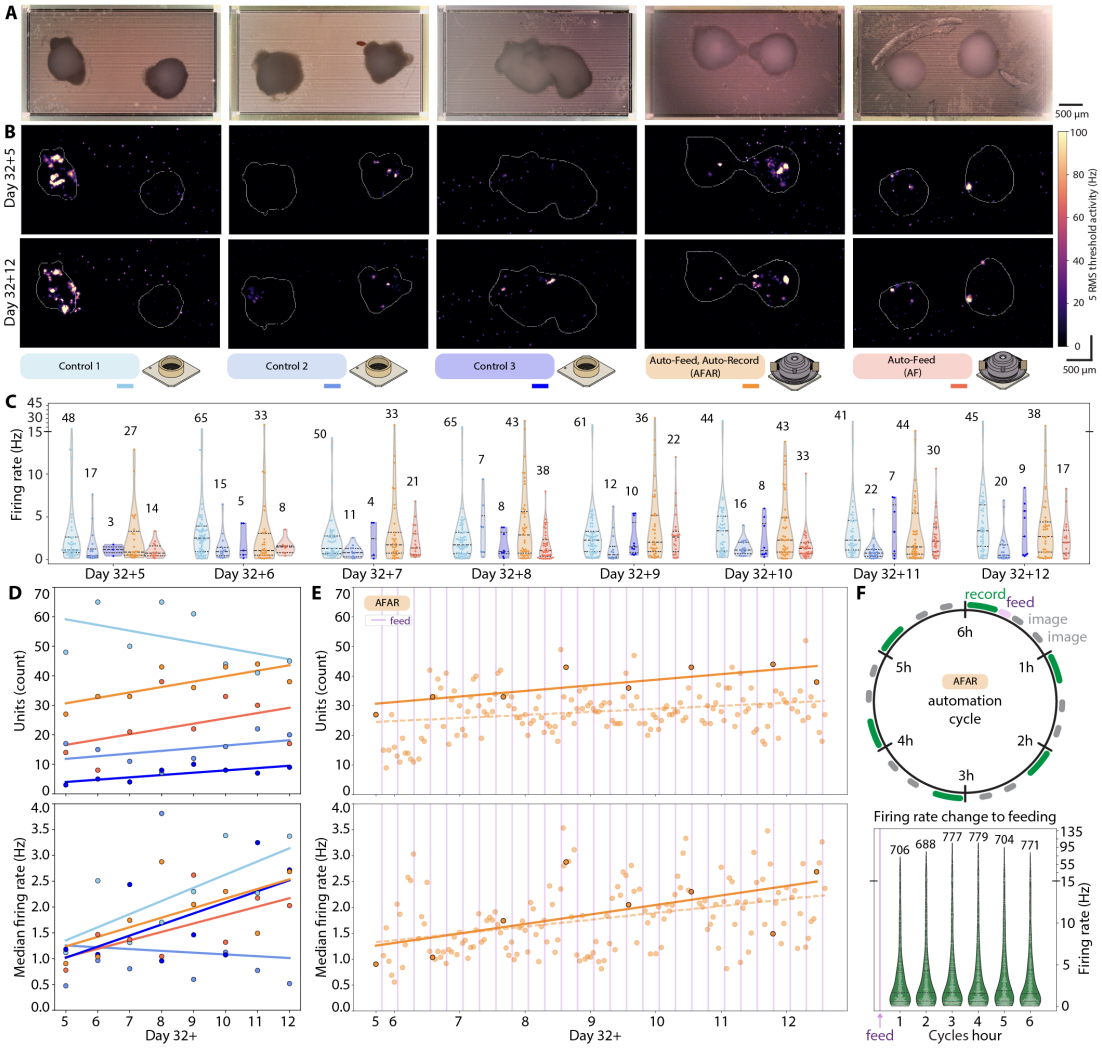

Figure 5.6: **Electrophysiology analysis of 7-day cerebral cortex organoid study.** (A) Organoid sample images. **(B)** Organoid boundaries on initial and final activity scans. **(C)** Spike sorting analysis from daily 10-min recordings quantifies neural units and their spiking frequency; violin plots indicate firing rates, lines denote the first (lowest) quartile, median, and third (highest) quartile. Total neural units labeled above each plot. **(D)** Daily detected units (top) and their median firing rates (bottom). **(E)** AFAR's 23 hourly recordings/day (translucent) show trends in units and firing rates over time, distinct from daily recordings (opaque); vertical lavender lines indicate feeds. **(F)** Dial schematic of AFAR's 6-hour automation cycle (top); hourly recordings are binned by 'hours since feed' with firing rates in violin plots (bottom).

11140050), 1 mM Sodium Pyruvate (Millipore Sigma # S8636), 2 mM Glutamax supplement (Thermo Fisher Scientific # 35050061), 0.1 mM 2-Mercaptoethanol (Millipore Sigma # M3148), and 0.05 mg/ml Primocin (Invitrogen # ant-pm-05). mESC maintenance media was supplemented with 1,000 units/mL of Recombinant Mouse Leukemia Inhibitory Factor (Millipore Sigma # ESG1107). Media was changed daily.

Vitronectin coating was incubated for 15 min at a concentration of 0.5 µg/mL dissolved in 1X Phosphate-buffered saline (PBS) pH 7.4 (Thermo Fisher Scientific # 70011044). Dissociation and cell passages were done using ReLeSR passaging reagent (Stem Cell Technologies # 05872) according to the manufacturer's instructions. Cell freezing was done in mFreSR cryopreservation medium (Stem Cell Technologies # 05855) according to the manufacturer's instructions.

5.4.2 Cerebral Cortex Organoids Generation

Mouse cortical organoids were grown as previously described by our group [172, 53] with some modifications. To generate cortical organoids we single cell dissociated ESCs using TrypLE Express Enzyme (ThermoFisher Scientific #12604021) for 5 minutes at 37°C and re-aggregated in lipidure-coated 96-well V-bottom plates at a density of 3,000 cells per aggregate, in 150 µL of mESC maintenance media supplemented with Rho Kinase Inhibitor (Y-27632, 10 µM, Tocris # 1254) and

1,000 units/mL of Recombinant Mouse Leukemia Inhibitory Factor (Millipore Sigma # ESG1107) (Day -1).

After one day (Day 0), we replaced the medium with cortical differentiation medium containing Glasgow Minimum Essential Medium (Thermo Fisher Scientific # 11710035), 10% Knockout Serum Replacement (Thermo Fisher Scientific # 10828028), 0.1 mM MEM Non-Essential Amino Acids (Thermo Fisher Scientific # 11140050), 1 mM Sodium Pyruvate (Millipore Sigma # S8636), 2 mM Glutamax supplement (Thermo Fisher Scientific # 35050061) 0.1 mM 2-Mercaptoethanol (Millipore Sigma # M3148) and 0.05 mg/ml Primocin (Invitrogen # ant-pm-05). Cortical differentiation medium was supplemented with Rho Kinase Inhibitor (Y-27632, 20 µM # 1254), WNT inhibitor (IWR1- ε , 3 µM, Cayman Chemical # 13659) and TGF-Beta inhibitor (SB431542, Tocris # 1614, 5 µM, days 0-7). Media was changed daily.

On day 5, organoids were transferred to ultra-low adhesion plates (Millipore Sigma # CLS3471) where media was aspirated and replaced with fresh neuronal differentiation media. The plate with organoids was put on an orbital shaker at 60 revolutions per minute. Neuronal differentiation medium contained Dulbecco's Modified Eagle Medium: Nutrient Mixture F-12 with GlutaMAX supplement (Thermo Fisher Scientific # 10565018), 1X N-2 Supplement (Thermo Fisher Scientific # 17502048), 1X Chemically Defined Lipid Concentrate (Thermo

Fisher Scientific # 11905031) and 0.05 mg/ml Primocin (Invitrogen # ant-pm-05). Organoids were grown under 5% CO2 conditions. The medium was changed every 2-3 days.

On day 14 and onward, we transferred the organoids to neuronal maturation media containing BrainPhys Neuronal Medium (Stem Cell Technologies # 05790), 1X N-2 Supplement, 1X Chemically Defined Lipid Concentrate (Thermo Fisher Scientific # 11905031), 1X B-27 Supplement (Thermo Fisher Scientific # 17504044), 0.05 mg/ml Primocin (Invitrogen # ant-pm-05) and 0.5% v/v Matrigel Growth Factor Reduced (GFR) Basement Membrane Matrix, LDEV-free.

5.4.3 Organoid Plating on Microelectrode Array

Mouse cerebral cortex organoids were plated, as previously described by our group [53], with two organoids per well. We plated the organoids at day 32 on MaxOne high-density microelectrode arrays (Maxwell Biosystems # PSM). Prior to organoid plating, the microelectrode arrays were coated in 2 steps: First, they were coated with 0.01% Poly-L-ornithine (Millipore Sigma # P4957) at 36.5°C overnight. Then, the microelectrode arrays were washed 3 times with PBS and coated with a solution of 5 µg/ml mouse Laminin (Fisher Scientific # CB40232) and 5 µg/ml human Fibronectin (Fisher Scientific # CB40008) prepared in PBS, at 36.5°C overnight.

After coating, we placed the organoids on the microelectrode arrays and removed excess media. The organoids were incubated at 36.5°C for 20 minutes to promote attachment. We then added prewarmed neuronal maturation media (described in the section above). We exchanged 1.0 mL of conditioned media for fresh every 2 days.

HD-MEAs containing the organoid cultures are stored in an incubator at 36.5 °C, 5% CO2, covered with membrane lids described in the section below, Assembled Devices and Custom 3D-printed Components.

5.4.4 Organoid Culture Using Automated Fluidics

The automated microfluidic pump system builds on previous work [210]. The microfluidic system was configured to support two chips (AF and AFAR) and their respective collection reservoirs (right and left) were imaged by the camera setup.

Fresh cell culture media is kept at 4°C refrigeration and accessed by the pump through flexible FEP tubing routed into a benchtop refrigerator and to a media bottled with a reagent delivery cap (Cole-Parmer VapLock). Fresh media is kept refrigerated to increase longevity and may be replaced during experimentation. To dispense, the syringe pump and distribution valves draw fresh media into the syringe vial and distribute the programmed volume into flexible FEP tubing

routed through an access port in the incubator. Here, the media is heated in incubator conditions prior to being delivered to the organoid inside the culture chamber. To keep media dispenses available on demand, a preheated 450 µL reserve (59% of the chamber's volumetric capacity) of fresh media remains idle in the FEP tubing so that upon dispensing, 37°C media is delivered to the well in less than 10 seconds. The FEP tubing is interfaced with the fluidic module with threaded ferrule lock and nut fittings (Cole-Parmer VapLock). Outflow from the fluidic module is drawn away with FEP tubing routed out of the incubator and into a refrigerator containing the collection reservoirs and computer vision camera setup.

For the collection reservoirs, we selected 15 mL Polyethylene Terephthalate (PET) conical tubes (430055, Corning) for high optical clarity, ease of replacement, and durability in downstream analysis and cold storage. To enhance visibility for computer vision imaging, we removed the factory-printed writing area on the conical PET tubes using generic, multipurpose tape. Flexible FEP tubing was interfaced with the PET tubes using a rubber cork plug (#6448K95, McMaster-Carr). The cork was pierced with 8-gauge steel needles that served as supportive conduits for the tubing. The tubing was secured inside the needle with glue (Loctite 4011) to create a hermetic seal at the point of interface. The steel encasing of the needles ensures a smooth, unobstructed flow within the flexible

FEP tubes. Each collection reservoir had two flexible FEP tubes: one for media coming from the fluidic module and one for pressurized operation connected to the syringe pump. This ensured that spent media never entered the syringe (only air). The air is expelled into a filtered (Millipore AA 0.22 µm syringe filter) safety container (not shown in Figure 5.1).

For the 7-day study described here, we designed for equivalent media exchange across conditions. The Controls 1-3 were fed 4 times at 1 mL per feed, totaling 4 mL of replacement media. AF and AFAR were fed 28 times at 143 µL per feed, totaling 4 mL of replacement media over the week. Summing the scheduled feeds and feedback adjustments, a single collection reservoir could store conditioned media for 2-3 weeks.

5.4.4.1 Priming the Experiment

On the 5th day on chip (Day 32+5), membrane lids for two HD-MEAs (AF and AFAR) were replaced with microfluidic culture chambers. During the replacement process, all media was aspirated from the HD-MEA's well with a P-1000 pipette. The microfluidic catch tray, followed by the culture chamber, was inserted inside the well, and 750 µL of the original media was added back to the microfluidic culture chamber. Excess media was discarded. The glass rod lid was placed on top.

Flexible FEP tubes (idling with DI water) were flushed with 1.0 mL of fresh

media. After priming the lines with media, the AF/AFAR chips were connected with fluidic fittings wrapped with Teflon tape. An initial aspiration leveled the media to the target fluidic operating range. The collection reservoirs were replaced with new empty conical tubes.

5.4.4.2 Running the Experiment

During the experiment, the media was exchanged using a feed cycle operation consisting of an aspiration followed by fresh media dispense. Here, we performed 143 µL aspirations and dispenses every 6 hours to match 1.0mL feeds every two days in the manual feeding controls. Feedback performed additional aspiration, dispense, and pull actions in addition to the basic feed cycle schedule to ensure the system stayed within normative error ranges. See section Feedback Interpreter.

5.4.4.3 Teardown of the Experiment

Once the experiment was stopped, chips were disconnected from the flexible FEP tubes by unscrewing the fittings. The flexible FEP tubes with fittings were sterilized in a flask containing disinfectant (Cydex) and covered with aluminum foil. The collection reservoirs with the experiment's conditioned media were disconnected and taken for analysis. New collection reservoirs were inserted for the cleaning cycle. The pump ran a cleaning solution (Cydex) through the entire internal cavity for 1 hour to disinfect the system. Following disinfection, DI water

and dry, sterile air were profused through the system for 12+ hours (overnight) to clear the disinfectant. The flexible FEP tubes were left resting with DI water until the next experiment.

5.4.5 Fluid Volume Estimation Using Computer Vision

The computer vision setup, located inside a 4°C refrigerator, included a support for the collection reservoir, a camera module, and an LED panel positioned behind the conical tubes. The LED panel served as backlighting to enhance the clarity and contrast of the images. The reservoir support was a two-plex 3D-printed system capable of multiplexity to tailor alternate experiments (see Assembled Devices and Custom 3D-printed Components). The camera and LED panel were both controlled by a Raspberry Pi.

To generate the calibration dataset, the camera module captured images of media in the collection reservoirs at select volumes over the entire range of the tube (0-12 mL), totaling 184 images. The volumes associated with each image were measured using a high-precision scale (30029077, Mettler Toledo). This approach enabled a correlation between the visual representation of media in the images and its actual volume (see Results).

To ensure image quality, our study introduced two checks to validate the integrity of the captured images: Lighting and blurriness. A region of interest (ROI)

was designated within the panel's area to verify the lighting conditions by checking that the average RGB color values each exceeded a minimum threshold of 20 out of 255. Blurriness was assessed by computing the variance of the Laplacian for the image, with a necessary threshold of 50 to pass. The thresholds were empirically determined using the calibration dataset.

Figure 5.3C illustrates the methodology applied to fluid segmentation, outlined in the Results section. The process begins with capturing an RGB image of the collection reservoirs that are fixed in place by the setup. To facilitate better segmentation and feature extraction, the RGB image is transformed into the HSV (Hue, Saturation, and Value) color space. A summation of the HSV values row-wise from the bottom to the top of the collection reservoir results in three distinctive profiles that allow differentiation between the liquid and background. Each profile, as illustrated in Figure 5.3C, presents a vertex at the boundary. A row value was established by averaging three rows identified in each HSV channel: an abrupt rise in the curve for the Hue channel, the absolute maximum for the Saturation channel, and the absolute minimum for the Value channel. From the average row value, the first segmentation was created. Everything below this row was set as white pixels, and everything above it was set as black pixels. A local evaluation around the average row was made to incorporate the meniscus in this segmentation. Utilizing HSV thresholds, the meniscus was accurately character-

ized and incorporated into the initial segmentation, culminating in the final image segmentation, in which white pixels represented the liquid portion.

The estimated volume was given by Equation 5.1, where x represents the segmented area in pixels, and the resultant volume is in microliters. Two different curves are used to account for the conical section for volumes under 1.5 mL (and pixel area less than 4446) and the cylindrical section for larger volumes.

$$V(x) = \begin{cases} 5.09 \times 10^{-9}x^3 + 2.39 \times 10^{-5}x^2 + 0.13x - 1.28 & \text{if } x < 4446 \text{ pixels} \\ 2.60 \times 10^{-11}x^3 + 5.38 \times 10^{-7}x^2 + 0.62x - 1288.37 & x \geq 4446 \text{ pixels} \end{cases} \tag{5.1}$$

The image segmentation and estimation based on the mathematical model (Equation 5.1) is carried out by a software program named the "Estimator." The process initiates with a feeding cycle, which triggers a picture request. Upon receiving the image of the collection reservoir, the "Estimator" analyzes the image and returns the estimated value of the fluid volume. The volume is relayed to the next module for feedback interpretation within the pump system (see Feedback Interpreter).

5.4.6 Feedback Interpreter

Computer vision volume estimations were compared to expectation values based on the sum total of pump action jobs. The feedback interpreter classified estimations into four categories: within tolerance, out-of-tolerance, anomaly, and tube change. Tolerance was a static volume selected at the start of the experiment. For the results shown here, the tolerance was 143 µL. If the volume estimation received was within the expectation value +/- the tolerance, the pump action was determined a success, and feedback ceased. If the volume estimation received was beyond the expectation value +/- the tolerance and also less than +/- 2000 µL, another cycle of feedback was engaged. When the volume was less than expected, for the first 5 iterations of feedback, aspiration jobs were sent to the pump with the difference of expectation and estimation. For iterations 6 to 19, pull jobs were sent to the pump, increasing by one for each subsequent interaction. A "pull" is a 1000 µL aspiration at 10x the standard syringe speed (applying a 1.1 x 103 mm/s flow rate), shown to generate the force required to break through variably high resistance in the conditioned media. At 20 iterations, the feedback interpreter requests manual intervention via the messaging application, and all further pump actions are suspended until the issue is resolved. When the volume was more than expected, dispense jobs were sent to the pump with the difference of expectation and estimation. Dispense actions were limited to 200 µL per action

and 2 iterations of feedback in total to prevent overflow. A volume estimation that was 2000 µL or more above the expectation value was determined as an anomaly and requested manual intervention via the messaging application, and all further pump actions were suspended until the issue was resolved. The feedback interpreter automatically detected collection reservoir tube changes when the volume estimation dropped by 2000 µL or more compared to the previous estimation and the total volume present was estimated as less than 2000 µL.

5.4.7 Organoid Culture Imaging

5.4.7.1 In-incubator Imaging

A 5MP digital microscope (AM7115MZTL, Dino-Lite) was placed over the organoid culture on the HD-MEA using holders described in Assembled devices and custom 3D printed components. Imaging was performed from the top through a glass rod (quartz drawn rod, 5mm ± 0.20mm dia x 15mm ± 0.20mm long, UQG Optics) (in AF/AFAR chips) or through a membrane lid (in control chips). The image is captured using reflected light from a built-in brightfield LED source next to the camera sensor. The 3D printed alignment trays handle most of the chip placement, with initial minor focal plane adjustment required. The microscope remains shut off until the software triggers it to turn on the lights and take a photo.

5.4.7.2 Image Segmentation for Organoids

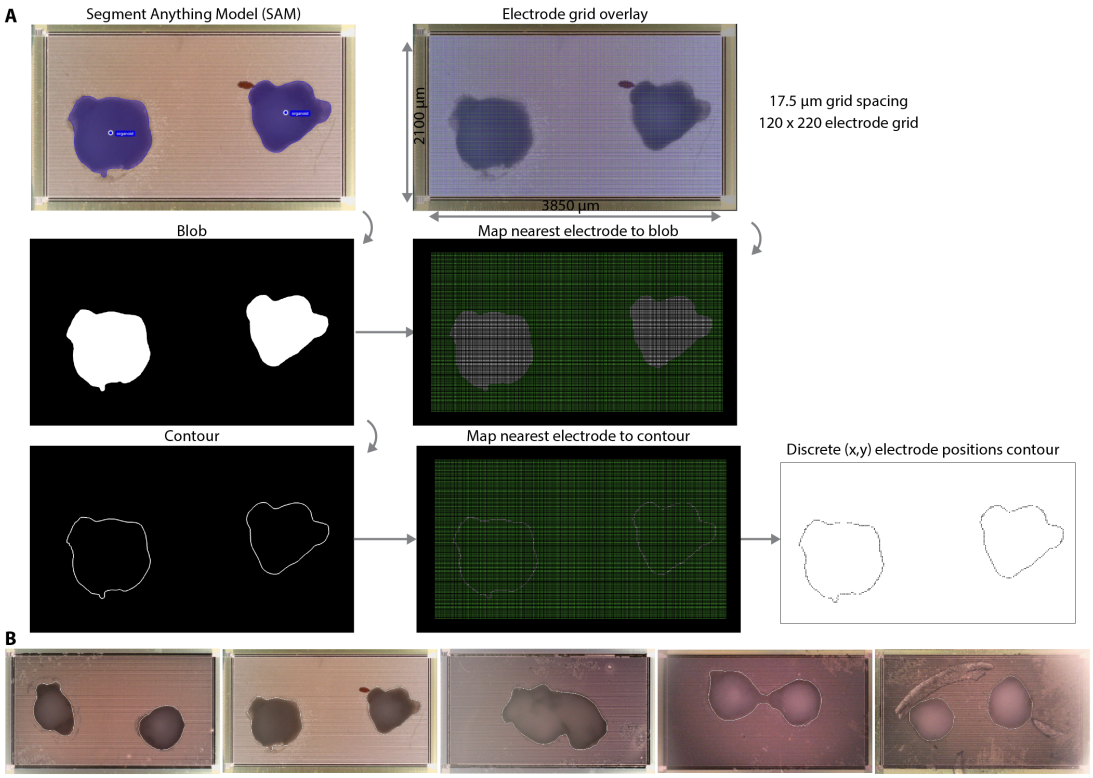

Figure 5.7: **(A)** Organoid boundary segmentation process. **(B)** Detected organoid boundaries for all chips.

.

In the process of image segmentation for organoid analysis, the first step involves applying an image calibration to correct any distortion. This procedure requires identifying four source points and four destination points. The former were manually selected from the distorted image. The latter were calculated based on an initial pixel (left corner of the HD-MEA), the size of the electrodes, and the spacing between them, both in millimeter units. This relationship between pix-

els and millimeters was established by using known dimensions of the HD-MEA border and electrode pitch in the image.

The organoid segmentation within the rectified image was accomplished using the Segment Anything Model (SAM) [110]. This model combines neural network architectures, allowing for precise and versatile image segmentation without requiring specialized training on new images. The segmented image is analyzed to detect variations in pixel intensity, which signify the presence of organoid contours. Both images with the organoid's contour and electrode grid are overlayed. Each electrode area is checked for the presence of the organoid's border. When a border is detected within an electrode's bounds, that particular electrode is marked prominently on the grid image to signify contact with the organoid (see Figure 5.6B). The step-by-step illustration of the analysis process is shown in Supplemental Figure 5.7.

5.4.7.3 Plotting & Alignment to Neural Activity Data

Electrode numbers as (x,y) position were plotted in matplotlib and exported as SVG. The SVG aligns over other plots, such as activity heatmaps, which follow the same x:3580 by y:2100 axis dimensions. Since electrophysiology plots use the electrode coordinate system with the same (x,y) positions, the image segmentation grid and neural activity plots are aligned on the same coordinate system.

5.4.8 Measuring Neural Activity

Extracellular field potential recordings were performed using CMOS-based high-density microelectrode arrays (HD-MEAs) (MaxOne, Maxwell Biosystems). Each HD-MEA contains 26,400 recording electrodes within a sensing area of 3.85 mm × 2.1 mm (each electrode has a diameter of 7.5 µm, spaced 17.5 µm apart center-to-center). A subset of up to 1020 electrodes (defined spatially by a configuration) can be selected for simultaneous recording [14]. Across one configuration, neuronal activity in microvolts was sampled over time at 20kHz and stored in HDF5 file format.

The experiment involved each chip's daily activity scans and recordings (described below). Each chip underwent an activity scan and subsequent recording every day, consistently conducted within the same one-hour time window. All chips shared the same recording unit and were recorded one at a time. For the AFAR condition, beyond the daily recordings and activity scans, the chip remained on the HD-MEA for automated hourly recordings.

The gain was set to 1024x with a 1 Hz high pass filter for both activity scans and recordings. The recording was set up to save 5 RMS thresholded spike times as well as all raw voltage data for downstream analysis and plotting.

All neural activity measurements were performed inside the incubator at 36.5°C, 5% CO2.

5.4.8.1 Activity scans

Activity scans were performed daily in the MaxLab Live Scope (Version 22.2.22, MaxWell Biosystems) to identify where the organoid's electrical activity is spatially distributed across the HD-MEA. The activity scan sequentially records from different configurations of up to 1020 electrodes, thereby sampling the microelectrode array for action potentials. We used the checkerboard assay consisting of 14 configurations, with 30 seconds of recording per configuration. The resulting activity heatmap (see Activity heatmaps) for each chip is shown in Figure 5.6B and Supplementary Figure C.3. Based on the assay results, 1020 most active electrodes were selected for simultaneous activity recordings.

5.4.8.2 Recordings

Each recording lasted 10 minutes. Initial recording configurations were created on the first day, and configurations were updated on the second day to match shifting activity. Afterward, we chose to keep the configurations constant across the final 5 days since the activity did not shift dramatically, and keeping the same configuration allowed for more consistent monitoring of the same region.

5.4.8.3 Smartplugs

A smartplug was connected to the recording system to automatically manage the duration of the recording system running. The smartplug (S31, SONOFF) running Tasmota 13.2.0 was connected to the MQTT broker (see MQTT) and received MQTT commands over WiFi to turn on and off.

The smartplug facilitated the automated recordings every hour: on the computer connected to the MEA recording system, a script running in Python (3.10) triggered the smartplug via MQTT to turn on the recording system, performed a recording using MaxLab Python API (MaxWell Biosystems), and afterward triggered the smartplug to turn off the recording system.

5.4.8.4 Spike sorting and curation

To know how automated culture affects the neuron's electrophysiology, each MaxWell recording is spike sorted into single unit activity using Kilosort2 [168]. By using a template-matching algorithm, Kilosort2 can cluster neurons based on their waveform shape. The settings for spike sorting are a bandpass filter of 300 to 6000 Hz for the raw data and voltage thresholding with 6 RMS above the baseline.

The sorting output is curated by an automatic algorithm that checks the signal-to-noise ratio (SNR), firing rate, interspike interval (ISI) violation, and the spike footprint for each putative neuronal unit. As a result, units that had SNR above

5, firing rate above 0.1 Hz, ISI violation below 0.1 and footprint on more than one channel are kept for analysis. Spike sorting was performed on the National Research Platform (NRP) computing cluster with an NVIDIA GeForce GTX 1080 Ti GPU.

5.4.8.5 Activity heatmaps

Activity heatmaps in Figure 5.6A depict the spatial distribution of significant voltage events. MaxWell software provides thresholded event identification based on moving root-mean-square (rms) value for each electrode, identifying events exceeding 5 times an electrode's rms value. We created a 2D grid of spike counts per second and applied a 2D Gaussian blur for visual smoothness, normalizing each grid point by dividing it by $2\pi r^2$ to re-scale back to the original Hz values. These values were then plotted as the activity heat maps. The heatmaps use warmer colors for higher firing frequency and darker colors for lower activity.

5.4.9 Cloud Infrastructure

The cloud infrastructure, including S3, MQTT messaging, and cloud processing within the IoT system, has been previously described [174]. Additionally, we added a database service and defined a consistent organizational structure for MQTT messages and topics across devices and cloud jobs.

We use a combination of self-hosted services running on a server, and large data storage and analysis are performed on the National Research Platform (NRP) cloud compute cluster [223] [1]. The devices are integrated with these cloud services:

- S3 cloud data storage: file storage using S3 object store, hosted on NRP cloud.
- Database: Strapi database stores device states, is self-hosted on our server, and is backed up to S3.
- MQTT messaging: EMQX MQTT broker, self-hosted on the server, and a Python messaging library (braingeneers.iot.broker) utilized by all software endpoints to send and receive messages from the broker.
- Cloud jobs/processing: utilizes a Kubernetes cluster on NRP and launches jobs. Employs software modularized by Docker containers and orchestrated by Kubernetes.
- User interfaces: features a website and integration with messaging apps (e.g., Slack) for interaction with devices, self-hosted on the server.

All custom software functionalities run in Docker containers and operate in a microservice architecture: specialized to a specific task and interface with minimal dependencies. A reverse proxy shields all web services from direct exposure to the

[1] `https://nationalresearchplatform.org/`

internet. For example, webpages are configured through a reverse NGINX proxy, which not only assigns a specific domain to each service but also handles SSL and authentication services.

5.4.10 Security

Devices initiate communication with the server and can be locked down to incoming traffic. Devices take MQTT commands in a specific format and are limited to the set of their defined commands, making them robust to command injection attacks. Accessing all cloud services requires authentication with user/device credentials. All web, MQTT messages, database, and S3 storage operations are encrypted. Access to the user interface website is restricted through the proxy with a login authentication step. On the server side, all web-based microservices are secured through an NGINX proxy. The proxy allows web-based services to be relatively untrusted by providing security (https, authentication, internet visible network listener) and keeping all other web-based services on an internal docker network inaccessible from the internet. This simplifies security for services that will change often and be written by programmers with minimal security training.

5.5 Conclusion

We integrated the custom-built and commercially available instruments using the IoT *device-class* framework. This system ensures faster, consistent, and always available operations, increasing the overall throughput while allowing the researchers to focus on formulating questions and data interpretation. Running on a distributed IoT network offers dual benefits. Using a local MQTT broker ensures reliable performance even during internet outages. Cloud integration enables global collaboration across distant labs for shared or complementary research. This setup enhances both the continuity of individual experiments and the integration of worldwide scientific efforts. The reduction of human intervention enabled by the microfluidic feeding system reduces the risk of contamination and other human-introduced mishaps. This is particularly valuable in months-long organoid experiments, where the accumulation of small variations in sample handling can accumulate to generate large differences between experimental batches.

Our system has the capacity to increase the frequency of media collections, morphology assessments, and electrophysiological measurements beyond what is feasible under standard conditions. Feedback in experimental setups becomes essential for maintaining target operating zones in the absence of direct physical observation. In this paper we demonstrated one method of feedback, which was needed to maintain a consistent volume in the organoid growth chamber. Dur-

ing our 7-day run, the system achieved this feedback autonomously and did not experience break-downs or need to use the messaging alert system to overcome anomalies.

How frequently should data be collected? By providing the ability to record as frequently as desired, our system can uncover the optimal frequency for meaningful data capture for rare but significant events. Neural processes unfold with remarkable complexity and variability, yet for practical reasons, many experimental paradigms are limited to daily recordings at most [64, 55, 208, 212]. Researchers can thereby miss crucial events that occur between observation points. From our results, the high-frequency recordings presented trends not captured in the once-a-day sampling. Hourly recordings like those conducted here can enable the detection of patterns, oscillations, and interactions that may be overlooked in sporadic recordings [200, 127]. These benefits are particularly relevant to researchers wishing to study phenomena with a more immediate timescale, such as neuroplasticity [236]. Additionally, many neurodevelopmental disorders have been hypothesized to be 'connectopathies,' characterized by abnormal connectivity [239]. Frequent recordings can provide a nuanced view of the underlying changes in activity patterns during neurodevelopment, contributing to a better understanding of the etiology of neurodevelopmental disorders.

In the future, devices can use the flexibility of MQTT messaging to allow the

creation of additional feedback loops to control the experiment. The computer vision techniques we applied to volume estimation could be extended to further applications such as colorimetric and absorbance sensing using the same setup to interrogate biochemical properties of the media. Such measurements could provide a more detailed and accurate analysis of organoid cultures and can lead to a more nuanced understanding of their behavior and responses to different stimuli.

The more the number and different kinds of measurements taken in an experiment, the more automation becomes essential to coordinate and manage the different modalities. The use of 3D printing technology enhances this flexibility, allowing for the seamless combination of multiple systems, such as the integration of our custom media exchange setup with the commercial HD-MEA and portable microscope. We foresee the integration of various sensory data and feedback mechanisms to analyze cell culture conditions. Our platform's consistency and reliability are ideal for comparative studies involving organoids of different genotypes or subjected to various pharmacological manipulations. This capacity to facilitate direct comparisons between diverse experimental conditions holds promise for advancing our understanding of neurodevelopment and neurodevelopmental disorders.

Chapter 6

Evaluation of Network Activity and Optogenetic Interventions

The following content in this Chapter 6 is adapted from a journal article in press at Nature Neuroscience, co-first authored with John P. Andrews and Jinghui Geng. I was responsible for designing the optogenetic system and software to stimulate the samples, helping conduct the experiments, contributing to several of the figures, and revising the manuscript with the team.

6.1 Introduction

Seizures are made up of the coordinated activity of networks of neurons, suggesting that control of neurons in the pathologic circuits of epilepsy could allow

for control of the disease. Optogenetics has been effective at stopping seizure-like activity in non-human disease models by increasing inhibitory tone or decreasing excitation, though this effect has not been shown in human brain tissue. Many of the genetic means for achieving channelrhodopsin expression in non-human models are not possible in humans, and vector-mediated methods are susceptible to species-specific tropism that may affect translational potential. Here, we demonstrate AAV-mediated, optogenetic reductions in network firing rates of human hippocampal slices recorded on high-density microelectrode arrays under several hyperactivity provoking conditions. This platform can serve to bridge the gap between human and animal studies by exploring genetic interventions on network activity human brain tissue.

6.2 System Design

6.2.1 Human Hippocampus Slice Culture and Transduction

To model human epileptiform activity, we established human organotypic tissue slices from hippocampus tissue (Fig.6.1a) donated to research by patients with drug-refractory epilepsy. Tissues were obtained from patients both with and without hippocampal sclerosis as defined by ILAE criteria [26] (Table E.1). Resected

tissue was sliced to 300µm and cultured on cell inserts at the air-liquid interface in serum-free media as previously described [40, 231]. Slices were transduced with AAV9 carrying a HcKCR1 [67] transgene driven by a CAMK2A promoter and a fluorescent tag (eYFP). Fluorescent reporter expression was observed in live imaging with an epifluorescent microscope by day 4-6 (transduced on day 0). On the day of experiments, the slice is plated with neuron-dense areas of interest positioned over the HD-MEA recording surface (Fig. 6.1b). A scan of the recording area electrodes is performed immediately after plating the slice to observe areas of spontaneous activity (Fig. 6.1c). After experiments, slices are fixed and reporter expression is confirmed by immunohistochemistry (Fig. 6.1d). Reporter expression was enriched in neurons of the granule cell layer and the dentate gyrus as well as pyramidal cells (Fig. 6.1e). The proportion of neurons expressing eYFP in areas of high transduction ranged from 10 – 54% (Table E.2). This variability may be the result of focal micropipette injection. Slices that did not show detectable eYFP were excluded from the analysis of transduction rates (see Methods). Together, these results indicate that we established organotypic tissue slice cultures of the human hippocampus and reproducibly delivered genetic payloads into hippocampal glutamatergic neurons using a combination of AAV9 and CAMK2A promoter-driven transcript.

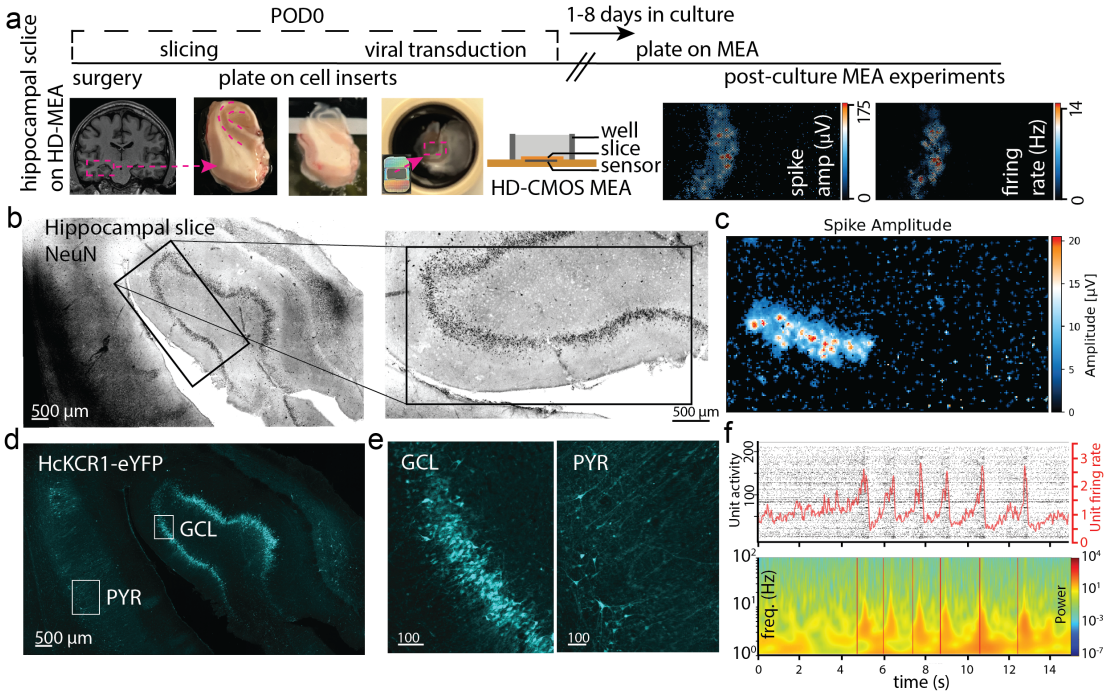

Figure 6.1: **High-density microelectrode array recordings of human hippocampal slices.** **(a)** Workflow of hippocampal slice recordings of high-density microelectrode arrays (HD-MEAs). Hippocampus specimens are collected on postoperative day 0 (POD0 = day of surgery), sliced, and plated on cell-culture inserts. Viral transduction is done on the same day as surgery. After 5-8 days in culture, slices are plated on HD-MEAs for recording experiments. **(b)** NeuN staining of a slice with a black rectangle overlaying the HD-MEA recording area (left) and higher magnification of the same image with black rectangle denoting HD-MEA recording surface. **(c)** Activity scan showing amplitude of spike activity in the area denoted by the rectangle in b. **(d)** Colocalization of eYFP with neuron-dense areas of the same hippocampal slice from b (slice 10F), 1 of 8 slices transduced with AAV9-HcKCR1 with correlative electrophysiologic data. **(e)** Insets of areas shown in d. Left: granule cell layer (GCL) of the dentate gyrus. Right: area of CA1 showing areas of pyramidal cell (PYR) morphology. Scale bars in microns. **(f)** Top: raster plot of unit activity with average unit firing rate (Hz) overlaid in red, demonstrating a sample of rhythmic bursting activity after adding kainic acid to a hippocampal slice (slice 10F). Bottom: local field potential from select electrodes from recording above, showing discrete increases in LFP frequency bands strongest in the theta range. Scale bars are shown in microns.

6.2.2 Optogenetic Control of Human Hippocampal Network

HcKCR1 encodes a kalium channelrhodopsin, a potassium-selective, light-sensitive ion channel that hyperpolarizes the neuronal membrane, thus reducing the probability of spiking when activated by 530nm light [67, 242]. Unlike a more traditional Channelrhodopsin-2 (ChR2), which encodes a sodium selective ion channel, inhibitory channelrhodopsin has never been applied to human tissue. To confirm that HcKCR1 illumination drives membrane hyperpolarization, we conducted intracellular voltage clamp recordings. Consistent with our expectations, HcKCR1 activation results in hyperpolarizing currents in human hippocampal neurons. To assess whether AAV-based transduction of human neurons with optogenetic constructs is specific to HcKCR1, we transduced additional slices with an excitatory channelrhodopsin (AAV9-CAMK2A-ChR2-eYFP) packaged in the same viral vector. In this case, we observed similar extent of expression, suggesting that our methods are not limited to HcKCR1. Together, these results demonstrate the feasibility of applying inhibitory optogenetics to human neurons.

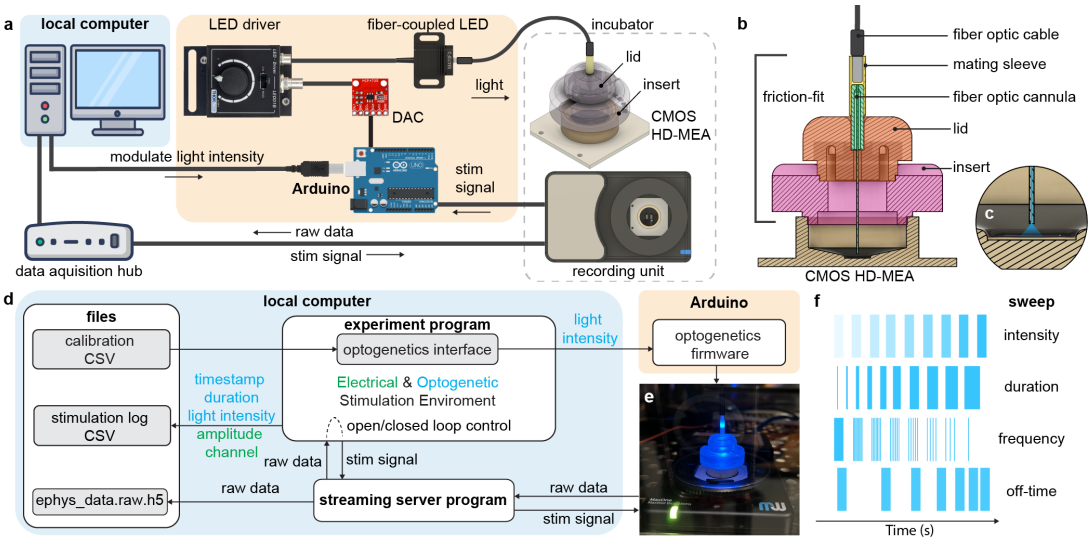

Figure 6.2: **Optogenetic device for multi-electrode array.** **(a)** Hardware components: the MaxWell CMOS HD-MEA system is augmented with an optogenetic platform consisting of an Arduino with a Digital to Analog Converter (DAC) controlling an LED driver to modulate light timing and intensity delivered to the biological sample on the HD-MEA. The optogenetic platform uses off-the-shelf optoelectronic equipment and 3D printable components (the lid and insert) for reproducibility. The MaxWell natively supports electrical stimulation. **(b)** Cross-section of optogenetic well insert showing main components. **(c)** Close-up of the optical fiber creating illumination. **(d)** Software modules: Code and data flow supporting optogenetic and electrical stimulation wrapped into Python libraries. Additional files store calibration for the expected LED power outputs, a log of stimulations delivered during an experiment with respective parameters, and MaxWell voltage recording data. Cyan elements are specific to optogenetic stimulation. Green elements are specific for electrical stimulation. All other software elements are shared. **(e)** Experimental setup inside the incubator showing the MaxWell chip with the optogenetic insert during an optical stimulation event. **(f)** Configurable stimulation templates are part of the software modules.

6.2.3 HD-MEA Integration with Optogenetic Activation

To test the effects of optically activating channelrhodopsins in our slice model, we integrated the HD-MEA recording system with fiber-coupled LED drivers to illuminate organotypic slices plated on the recording array. The hardware platform was designed using off-the-shelf components, so the design is easily reproducible and does not require custom circuit boards or soldering. The interface allows containing the sample in a tissue culture incubator (Fig. 6.2). While closed in the incubator, the system is controllable from external computers. Custom software was created to allow for real-time analysis of spike event data, allowing for observation of electrophysiological activity and the impact of optogenetic perturbations with minimal delay. The system allows software control of light intensity, duration, frequency, and off-time.

6.3 Results

Figure 6.3: **Optogenetic inhibition of human hippocampal activity. (a)** Stacked raster plot of single unit activity from a hippocampal slice expressing HcKCR1. On the y-axis are 5 trials (t1 – t5) of continuous 10s illumination, stacked to line up the phase immediately preceding illumination (pre), the light-ON phase (green), and the 10s following the end of illumination (OFF). The average firing rate (fr) of all units overlaid (red). **(b)** Heat maps of the electrode arrays showing 5-rms spike activity across the electrode recording surface during the 10s bins shown in a (both a and b from slice 3C). Black represents HcKCR1-eYFP staining. **(c)** Similar stacked raster plot with firing rate overlay of a single slice recorded in 0-mg media, followed by **(d)** recordings after addition of KA to the slice (c – h are from slice 10F). **(e)** Expanded picture of one of the series of rhythmic bursts of activity seen in the stacked raster of d. **(f)** Local field potential frequency spectrum over time from a selected unit during the panel e time period. **(g)** Expanded region of e, showing non-random coherence (see KLD methods) in the theta frequency band (pink) with firing rate (red) overlaid. **(h)** Rose plots (on a 2 pi radian phase circle) showing non-random phase distribution of theta coherence in subsets of the highlighted burst of coordinated activity in gI. **(i)** random theta phase distribution in gII. **(j)** Stacked raster of a slice showing optogenetic inhibition of activity after GABAergic blockade with bicuculline (j – k from slice 5C). **(k)** Heat maps of the electrode arrays showing 5-rms spike activity across the electrode recording surface during the 10s bins shown in j. Black represents HcKCR1-eYFP staining. **(l)** Schematic of closed-loop, responsive optogenetic illumination. **(m)** Example of using closed-loop optogenetic silencing of bicuculline-provoked activity. Shaded red outline of red firing rate line in a, c, d, and j represents standard error of the mean of firing rate.

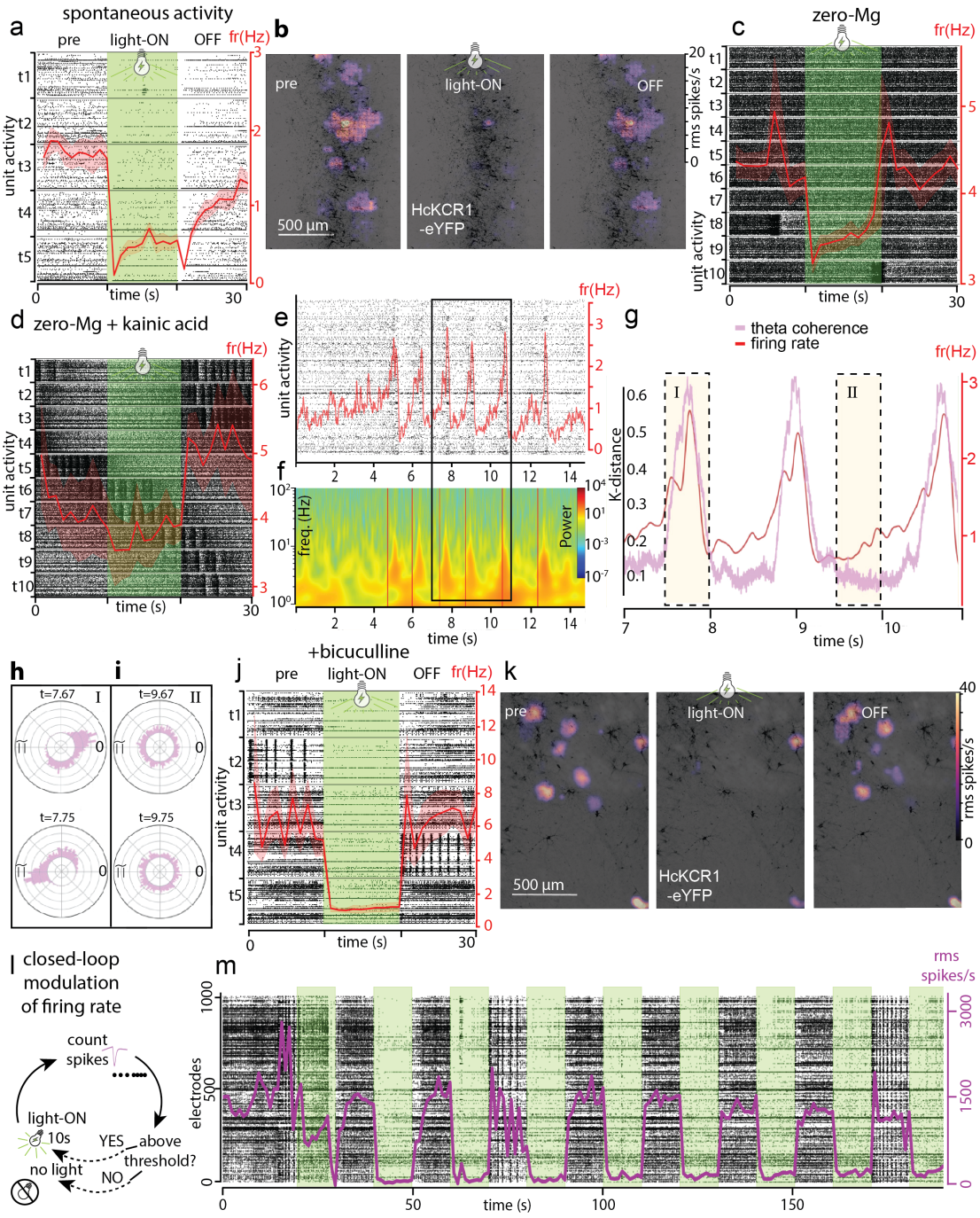
a
spontaneous activity
pre
light-ON
OFF
fr(Hz)
unit activity
t1
t2
t3
t4
t5
time (s)
b
pre
light-ON
OFF
500 µm
HcKCR1
-eYFP
c
zero-Mg
fr(Hz)
rms spikes/s
unit activity
t1
t2
t3
t4
t5
t6
t7
t8
t9
t10
time (s)
d
zero-Mg + kainic acid
fr(Hz)
unit activity
time (s)
e
unit activity
f
freq. (Hz)
Power
time (s)
g
theta coherence
firing rate
fr(Hz)
K-distance
I
II
time (s)
h
i
t=7.67
t=9.67
t=7.75
t=9.75
+bicuculline
j
pre
light-ON
OFF
fr(Hz)
unit activity
time (s)
k
pre
light-ON
OFF
500 µm
HcKCR1
-eYFP
rms spikes/s
l
closed-loop
modulation
of firing rate
count
spikes
light-ON
10s
YES
above
threshold?
no light
NO
m
rms
spikes/s
electrodes
time (s)

6.3.1 Optical HcKCR1-mediated Inhibition of Network Activity

HcKCR1 activation suppressed activity in human hippocampal neurons across all experimental conditions of spontaneous and provoked activity (Fig. 6.3, Table E.2). Illumination with 530nm light [67] resulted in rapid silencing of hippocampal activity (Fig. 6.3 and E.1, E.2, E.3). Constant illumination for 10 seconds reduces spontaneous firing rates (Fig. 6.3a). Changes in spike amplitude were less consistent (Fig. E.1). The reduction in neuronal spiking was consistent and evident in raw data (Fig. 6.3a, Fig. E.1). Intensity scans across the full range of light intensity produced by the LED driver were carried out to determine the dynamic range of the control of neuronal firing rates as a function of illumination power (Fig. E.4). The intensity threshold was typically between (26.2 mW/mm^2 - 31.2 mW/mm^2), correlating to 40-50% of the possible output from our drivers. For experiments, we utilized one step above the minimum threshold (i.e., 50 - 60% intensity, translating to 31.2 – 35.8 mW/mm^2). Decreases in neuronal firing rates during HcKCR1 optogenetic activation were obtained from n=8 ex vivo hippocampal slices (Table E.2). AAV-mediated of HcKCR1 is sufficient to enable optogenetic modulation of network-wide spontaneous activity despite incomplete transduction (Table E.2). Spontaneous activity arises from networks perched in a balanced regime that is neither prone to silence nor saturation [136]. As a result,

relatively small increases in inhibitory tone at a cellular level may be insufficient to offset the imbalance necessary to generate epileptiform activity at a network level.

6.3.2 Optogenetic Suppression in Provoked Hyperexcitability

Next, we tested HcKCR1-mediated optical inhibition in the context of hyperexcitable conditions. Under all these conditions, HcKCR1 activation reduced firing rates in large portions of units recorded (Table E.2). We used a magnesium-free (0-mg) media, a long-standing approach used to increase neuronal excitability and induce epileptiform activity in hippocampal preparations [9, 145, 149]. Clear, spontaneous bursts of activity were observed 2/4 slices bathed with 0-mg media (Fig. 6.3c). These bursts of activity were <1s in duration and several minutes apart, reminiscent of interictal epileptiform spikes [106]. Overall firing rates of slices were reduced in slices bathed in 0-mg media during periods without spike activity. Average firing rate reduction of the grouped unit activity in two slices did not meet statistical significance in the zero-magnesium media conditions (Fig. E.2). However, on a unit-level analysis (and in raster plots of Fig. E.2g and j), 15 – 40% of units in these slices had a decrease in firing rate of at least 90% during light-ON conditions (Table E.2, 11G and 12G), demonstrating that not

all units in each slice respond uniformly. Spike events during 0-mg recording conditions were not completely absent during optical inhibition of two separate slices (Fig. 6.3 c, t10, Fig. E.2 d and g). The spikes were far enough apart in time to prevent strong conclusions about the effects of optical inhibition on these events. Addition of kainic acid (KA) has been used in various epilepsy models [101, 135, 241, 98]. Based on other groups reporting the effectiveness of combining multiple pro-convulsant pharmacologic interventions to induce epileptiform activity [101, 91], we tested whether adding kainate to 0-mg bathed slices would lead to epileptiform activity. The addition of KA resulted in acute elevations in firing rate, and in 2/4 slices recorded with KA, rhythmic bursts of activity occurred (Fig. 6.3d). Slices exhibiting this rhythmic bursting of unit activity also showed increased coherence across most frequency power bands, most clearly in the theta band (Fig. 6.3 f-g). Repeated 10s periods of illumination clearly showed reduced firing rates during light-ON conditions (Fig. 6.3d), but a causal effect of illumination on the coordinated bursts is less clear in the absence of more comprehensive characterization of the typical effects and expected frequency of rhythmic bursting with addition of KA.

To explore this platform's ability to perform closed-loop illumination, we used a $GABA_AR$ blockade via the application of bicuculline to elevate firing rates above their baseline levels (Fig. 6.3 j-k). We utilized the reproducible increases in firing

rate with $GABA_AR$ blockade to detect and disrupt elevations in network firing. We use automated, real-time spike event detection to trigger LED illumination by crossing a firing rate threshold. (Fig. 6.3h-k). The closed-loop illumination software is activated following bicuculline application, and firing rates surpassing the threshold triggers 10-seconds of continuous illumination. This dramatically reduced the firing of recorded units (Fig.3h-k). This was replicated in n=3 HcKCR1-expressing slices derived from n=2 patients. These results demonstrate a potential benefit of optogenetic interventions in epilepsy: modulation of brain activity restricted precisely to time and anatomy in which pathologic elevations in neuronal firing occur.

In these three distinct methods of provoking a hyperexcitable state (0-mg, 0-mg+KA and $GABA_AR$ blockade), HcKCR1 activation in a subset of glutamatergic CAMK2A-expressing neurons reduced network firing rates. Fraction of neurons transduced in a recording area did not completely explain different fractions of neurons exhibiting reduced firing rates in light-ON conditions (Table E.2). The magnitude of firing rate reductions in 0-mg and 0-mg+KA conditions was less than that observed in physiologic media and GABAergic blockade. While several variables may contribute to this, HcKCR1-mediated inhibition of presynaptic CAMK2A-expressing neurons may be partially offset by post-synaptic glutamatergic receptor activation in 0-mg and 0-mg+KA conditions. Whether HcKCR1 acti-

vation of CAMK2A-expressing neurons effectively interrupts provoked coherence seen in 0-mg + KA conditions will require additional experiments to thoroughly characterize the effects of the rhythmic burst activity induced with 0-mg + KA.

Figure 6.4: **Waveform clustering (a)** UMAP of waveform clusters of all HD-MEA extracellular unit activity recorded from all slices (Table E.2). **(b)** All waveforms combined into clusters (colors), with the average waveform of each cluster (black). **(c)** Violin plots showing trough-to-peak and FWHM features for each cluster. For box and whisker plots, the box extends from the first quartile to the third quartile of the data, with a line at the median. The whiskers extend from the box to the farthest data point, lying within 1.5x the interquartile range from the box. To determine whether clusters were significantly associated with areas of GCL coverage, Neuronal units were dichotomized as being recorded from GCL on histology or not, and logistic regression (see methods) was used to estimate the odds ratio of GCL localization for units in each cluster of N=12 clusters. *Comparisons significant if P¡0.05 after correction for multiple comparisons (cluster 5 OR 10.2, CI 5.8-18.3, P=2.67E-15; cluster 6 OR 8.3, CI 4.4-15.7, P=1.24E-10; cluster 8 OR 8.4 CI 4.6-15.3, P=5.95E-12; cluster 9 OR 2.3 CI 1.5-3.5, P=7.78E-05; cluster 10 OR 2.3 CI 1.5-3.7, P=3.63e-04). **(d)** Overlay of all waveforms analyzed. **(e)** UMAP from a, with units represented by slice 10F, consisting of granule cell layer (GCL) coverage, colored by waveform cluster. **(f)** units from 10F projected spatially onto the MEA recording area. Density histograms show the distribution of units in the slice assigned to each waveform cluster. **(g)** Units and recording area from f overlaid onto histology of the slice, showing GCL anatomic correlation. **(h,j)** Similar analysis for slice 3C, representing Cornu Ammonis (CA) 1 area with no GCL coverage. OR = odds ratio, CI = 95% confidence interval.

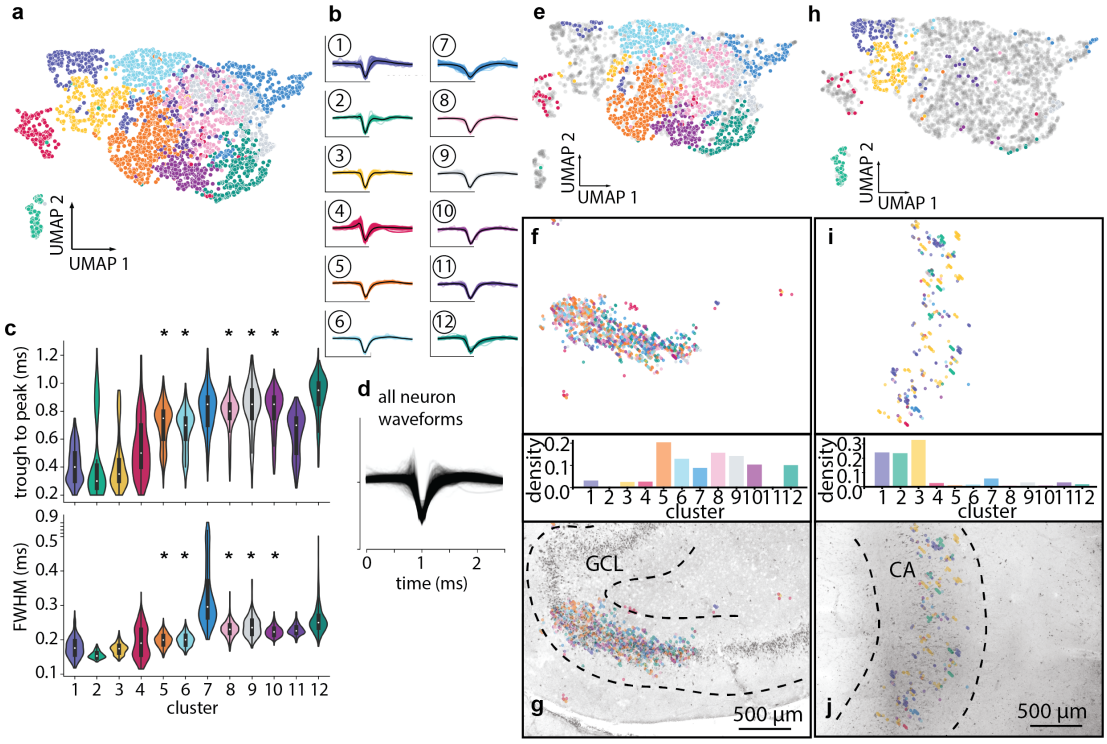
a
UMAP 2
UMAP 1
b
c
trough to peak (ms)
FWHM (ms)
cluster
d
all neuron
waveforms
time (ms)
e
UMAP 2
UMAP 1
h
UMAP 2
UMAP 1
f
density
cluster
g
GCL
500 µm
i
density
cluster
j
CA
500 µm

6.3.3 Waveform and Opto-response Clustering

Reduced unit firing with HcKCR1 activation was not uniform across recorded units (Fig. 6.3, and E.1, E.2, E.3), ranging from complete silencing to more subtle or no apparent firing rate changes in other units. Given that AAV9 transduction was not uniform across the tissue, this may partially explain such a spectrum of response, but there was not a clear correlation between transduction rate and fractions of units with reduced firing (Table E.2). However, cell type is another variable that could affect a unit's response to HcKCR1 activation even in the presence of similar transduction. To investigate whether the response parameters of the units are uniform [67, 81], we investigated whether unit cell-type differences could be inferred from the HD-MEA extracellular recordings.

We applied a waveform clustering method [123, 126] to group units based on features extracted from the extracellular action-potential waveform (Fig. 6.3.2). This analysis yielded 12 separate clusters (Fig. 6.3.2). To validate whether the distribution of putative cell types identified by waveform clustering is consistent with anatomy, we aligned the recording array electrodes with histology to approximate the anatomic slice area from which each electrode is recorded. If waveform clusters correlate with putative cell types, then recordings over an anatomic area with a relatively homogenous cell type should be enriched for waveform clusters underrepresented in anatomic areas without such cells. We analyzed waveform

clustering in areas of the dentate gyrus granule cell layer (GCL) versus recordings without granule cell layer representation. We compared the distribution of unit waveform cluster in 3 slices with clear GCL coverage to 6 slices recorded where active recording electrodes did not overlap with GCL. Five waveform clusters were significantly over-represented in the GCL recordings (Fig. 6.3.2, Table E.3). Next, to characterize the heterogeneity of unit responses to optogenetic activation, we used an HDBSCAN-based clustering technique [143, 144]. We analyzed peri-stimulus histograms of neuronal firing rate spanning time segments before and during optogenetic activation. We found 5 distinct opto-response clusters (Fig. 6.3.3 a, b), 4 of which showed statistically significant reductions in mean firing rate and firing rate distribution with optogenetic activation (Fig. 6.3.3 c). Since our waveform clustering suggested that 5 of the waveform clusters were associated with recordings of the GCL, we treated these waveform clusters as a single category when testing whether opto-response clusters were associated with any putative cell types from waveform clustering. There was indeed a significant association between the GCL waveform cluster and the opto-response cluster 3 (Table E.3), in addition to associations between several other waveform and opto-response clusters. While this is far from definitive for stipulating cell type as the only or most prominent factor in neuronal response to HcKCR1 activation, it is consistent with the hypothesis that response to optogenetic activation may differ

between cell types. Moreover, it suggests the need for further clarification of how optogenetic interventions in different cell-types may affect those cell-types and networks differently.

Figure 6.5: **Optogenetic response clustering. (a)** UMAP of units clustered through an HDBSCAN pipeline of a 20s period of time correlating with 10s of time prior to light-ON and 10s during light-ON. **(b)** Average firing rates for units in each cluster over the course of the analyzed 20s period. **(c)** Firing rate (left) and standard deviation of firing rate (right) of each cluster showing the distributions during light-OFF and light-ON periods. *significant differences in firing rate or firing rate standard deviation between light-ON and light-OFF conditions. Mean and standard deviation distributions were compared via a two-sided Kolmogorov-Smirnoff test, considered statistically significant if P¡0.05 after correction for multiple comparisons. P-values for firing rate light-OFF vs light-ON comparisons (left 2 columns): Cluster 1 p=2.5E-45, Cluster 2 p=0.0014, Cluster 3 p=7.29E-24, Cluster 4 p=1.36E-16, Cluster 5 p=0.0741. P-values for firing rate standard deviation light-OFF vs light-ON comparisons (right 2 columns): Cluster 1 p=6.43E-25, Cluster 2 p=0.0002, Cluster 3 p=1.28E-21, Cluster 4 p=9.38E-13, Cluster 5 p=0.174. **(d & e)** Recording areas covering 2 distinct hippocampal regions known to have disparate cell types. Density histograms represent the fraction of units in the slice assigned to each cluster. **(d)** the granule cell layer of the dentate gyrus (GCL) in slice 10F and **(e)** Cornu Ammonis (CA) in slice 3C. Opto-response cluster identity color is overlaid onto their respective unit locations. Unit locations are shown without (top) and with (bottom) histology underlaid. White immunohistochemistry demonstrates HcKCR1-eYFP expression. Cluster 3 was found to be positively correlated with GCL waveform clusters (z-score 3.28, Table E.3) via a Chi-square test with analysis of standardized residuals (see Methods: Waveform cluster association with opto response clusters). This standardized residual was considered significant if greater in magnitude than a critical value of 3.23 calculated for a two-tailed test with the Bonferroni-adjusted significance level.

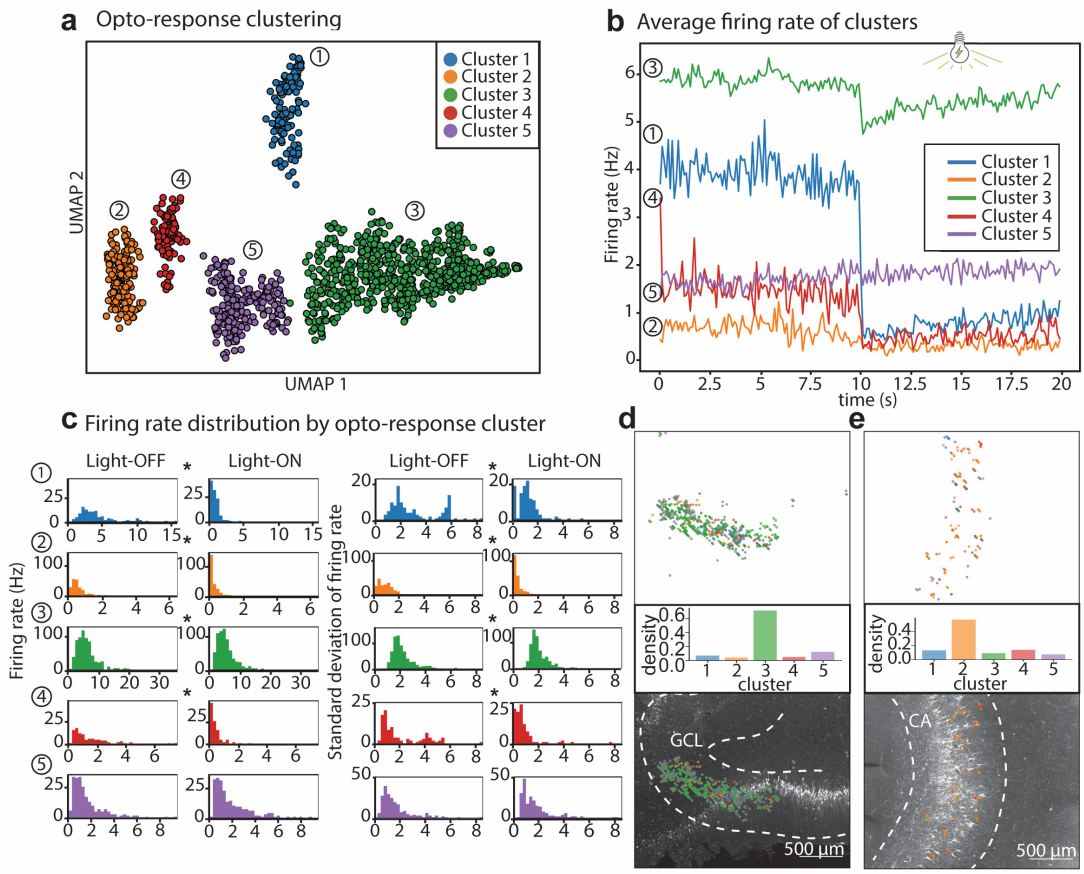
a Opto-response clustering
Cluster 1
Cluster 2
Cluster 3
Cluster 4
Cluster 5
UMAP 2
UMAP 1
b Average firing rate of clusters
Firing rate (Hz)
time (s)
c Firing rate distribution by opto-response cluster
Light-OFF
Light-ON
Firing rate (Hz)
Standard deviation of firing rate
d
density
cluster
GCL
500 µm
e
density
cluster
CA
500 µm

6.4 Materials and Methods

This research complies with all relevant ethical regulations and was approved by the University of California-San Francisco institutional review board. Informed consent was obtained by patients prior to surgical resections for refractory epilepsy. There was no participant compensation. The sex, number, and age of participants are detailed in Table E.1.

6.4.1 Tissue Preparation and Culture for Recordings

Human hippocampal specimens were obtained from patients undergoing temporal lobectomy with hippocampectomy for refractory epilepsy with University of California-San Francisco IRB approval. Tissue was transported in artificial cerebrospinal fluid (aCSF) bubbled with carbogen, then sliced into 300µM sections and recovered sequentially in HEPES buffered aCSF and culture media. The slices are plated on cell-culture inserts to allow for long-term culture at the air-liquid interface. Viral transduction was performed on the day of plating with glass micro-pipets. Slices were subsequently plated on HD-MEAs with minimal culture media. For optogenetic recordings, a custom, open-source hardware platform was used with off-the-shelf optoelectronic equipment and 3D-printed components.

Human tissue samples were collected from select neurosurgical cases at UCSF with signed patient consent and approval from the UCSF Institutional Review

Board.

Tissue transport and preparation were adapted from Ting et al [231]. Briefly, tissue was collected in the operating room and put in sterile artificial cerebrospinal fluid (aCSF) of the composition (in mM): 92 NMDG, 2.5 KCl, 1.25 NaH2PO4, 30 NaHCO3, 20 4-(2-hydroxyethyl)-1-piperazineethanesulfonic acid (HEPES), 25 glucose, 2 thiourea, 5 Na-ascorbate, 3 Na-pyruvate, 0.5 CaCl2·4H2O and 10 MgSO4·7H2O. Before collection, the pH of the aCSF was titrated to 7.3–7.4 with hydrochloric acid, and the osmolality was 300–305 mOsmoles/Kg. The solution was pre-chilled to 2–4°C and thoroughly bubbled with carbogen (95% O2/5% CO2) gas before collection.

Tissue was cut into 300 µM slices submerged in carbogen-bubbled aCSF using a vibratome. Slices were briefly recovered in aCSF warmed to 33°C before plating on cell culture inserts at the air-liquid interface and incubating at 37°C in 5% CO2 incubators.

Tissue was cultured and recorded in a media formulation adapted from prior studies [40, 231], referred to in the manuscript as physiologic media. 15% BME, 15% DMEM/F12 + Glutamax, 0.65% % PBS, 3% H2O, 0.91 mM CaCl2, 1.96 mM KCl, 0.81 mM MgSO4, 81.90 mM NaCl, 0.84 mM NaH2PO4, 14.0 mM NaHCO3, 0.5 µM ZnSO4, 0.01 µM CuSO4, 0.63 mM d-Glucose, 0.14 mM Sodium Pyruvate, 0.58 mM Ascorbic acid, 1.0 mM Oxalo-acetic acid, 4.0 mM Sodium lactate, 0.57

mM Citric acid, 4 mM Sodium lactate, 0.27% BSA, 0.001 µM 17-b-Estradiol, 2.28 µM a-Tocopherol, 2.10 µM a-Tocopherol-acetate, 0.06 µM Corticosterone, 5 mM Creatine, 1 mM Sodium b-hydroxybutyrate, 5 mM Mannitol, 0.2 mM Phosphate creatine, 0.5% N-2 supplement, 1250 U/mL Heparin, 0.01 mM ATP, 0.41 µM Insulin, 0.0003 µM Tri-iodo-I-thyronine sodium, 0.08 µM Superoxide dismutase (SOD), 0.05 mM Glycerol (10x), 0.5 mM Glutamax, 1 µM MnCl2, 1 µM g-Amino-butyric acid, 3 µM Glutathione, 8 µM Taurine.

6.4.2 Plating Slices on HD-MEA

To plate tissue plated on MaxWell high-density MEAs, MEAs were incubated with Matrigel for 1 hour, and subsequently filled with culture/recording media described above. Slices were floated into the MEA wells and the media was then aspirated slowly such that the slice descended onto the recording surface. The slice was kept in minimal media for the 2 hours during which recordings were carried out. For $GABA_AR$ blockade, bicuculline dissolved in recording media to a concentration of 2µM was dripped directly on the tissue slice. For Low magnesium media, the physiologic media was made without any magnesium (MgSO4) added. For Kainic acid experiments, 100nM kainic acid was dripped directly onto the slice.

Examples are shown of large areas of dense activity recorded in Figure 6.1

and Figure 6.3 and overlaid on Figure 6.3.2 g & j and Figure 6.3.3 d & e. Slices that did not show electrophysiologic evidence of unit activity after plating were excluded from electrophysiologic analyses.

6.4.3 Immunohistochemistry

Immunohistochemistry for NeuN and eYFP in the manuscript was performed with the following antibodies. NeuN: guinea pig anti-NeuN, (Millipore, ABN90, dilution 1:1000, lot#4077530), eYFP: Chicken anti-GFP antibody (Aves, GFP-1020, dilution 1:1000, lot# GFP3717982).

6.4.4 Adeno-associated Viruses

AAV9-CAMK2A-HcKCR1-eYFP: titer 5.00E+13 GC/mL (PackGene, Lot# 12109T). Purity analyzed according to PackGene company protocols by SDS-PAGE finding no other significant bands. Endotoxin assay analyzed by Quantitative LAL assay with <10EU/ml.

AAV9-CAMK2A-ChR2-eYFP: titer 2.40E+13 GC/mL (Addgene, Lot# v113177). Purified by Iodixanol gradient ultracentrifugation. The purity of AAV preparation was assayed according to Addgene company protocols by comparing the relative stoichiometric ratios of the viral capsid proteins VP1, VP2, and VP3. Samples of viral preparations were subjected to polyacrylamide gel electrophoresis (PAGE)

followed by silver staining or SYPRO Red staining, and the molecular weight and relative intensity of the viral capsid proteins were analyzed. Endotoxin assay analyzed by Quantitative LAL assay with <5EU/ml.

6.4.5 Design of Optogenetic System

The purpose of the designed hardware platform is to trigger an optogenetic stimulation pulse and observe the response of neurons on a high-density electrode array. The optogenetic system was designed to be easy to replicate and does not require custom PCBs or soldering.

To run an experiment, the user must specify a calibration CSV file, which contains data on an LED's power output (see section Optogenetic power density measurement and calculation). The user also connects to the Arduino over a USB serial port. Afterward, the program creates a stimulation log CSV file into which the stimulation events with their parameters are recorded. Now, the user can construct their own stimulation sequences and use several helper functions with configurable stimulation pattern templates (Fig. 6.2f).

As the user runs the experiment, stimulation events are logged in both the stimulation log CSV file and the MaxWell voltage recording .hdf5 file. The MaxWell .hdf5 file has a field that stores a single bit value representing the GPIO pin signal ('1' for on, '0' for off) for every frame of the recording (every 0.05 ms assuming

20kHz sampling). Therefore, we can extract at which recording frame the light turned ON, and at which recording frame the light returned to being OFF. The CSV log file stores a timestamp of each event, as well as the intensity of light used and the duration of ON and OFF requested by the user.

6.4.6 Software Low-level Functionality

The computer sends the Arduino an integer value over USB serial connection corresponding to the desired intensity. While the intensity is represented to the user as a decimal number between 0 and 1, it is converted to the nearest proportional integer in the range of the 12-bit DAC (0 to 4095). The range 0 to 4095 was chosen instead of the full 12-bit integer range 0 to 4096 because it more closely corresponded to 0 to 5V DAC output when measured on an oscilloscope. The computer also sends the electrophysiology recording system a signal to set GPIO high. GPIO high is +2.0 - 3.3V; anything less or near zero is considered GPIO low. When the GPIO signal is high, the Arduino sends a value to the DAC. Thus, to turn the light on, the computer needs to send a non-zero intensity value to the Arduino, and also trigger the MaxWell recording system to set GPIO high.

6.4.7 Optogenetic 3D Printed Insert and Lid

The optogenetic insert and lid (Fig 6.2b,e) were designed to hold the optical fiber in place inside the MEA recording well while keeping an enclosed environment around the tissue culture.

The insert has a tight transition fit with the round MEA well. The lid slots into the insert and is easy to remove but does not rotate because there are alignment groves between the insert and lid. This combination allows having a sturdy interface with the MEA well while being able to gently remove the lid (i.e., to add a drug during the experiment) and keep the fiber in the same relative position after re-inserting.

The lid is designed for a fiber optic component with a 2.5mm diameter fiber optic cannula, Ø200 µm core fiber with 0.22 NA, and a fiber length of 20 mm (CFM22L20, Thorlabs). The optical fiber is estimated to be 0.95mm above the MEA sensor based on MEA well measurements and computer-aided design (CAD) model of the assembled components.

The optogenetic insert and lid were 3D printed (on Form 3B+, Formlabs) with BioMed Clear V1 material (RS-F2-BMCL-01, Formlabs). Prior to use in tissue culture, the 3D printed parts, along with the optical fiber (CFM22L20, Thorlabs) and ceramic mating sleeve (ADAF1-5, Thorlabs) were individually sealed in autoclavable bags (RIT-3565, PlastCare USA) and steam sterilized either at 134°C

for 20 minutes or 121°C for 30 minutes.

6.4.8 Activity Detection and Closed-loop Optical Intervention

We implemented an algorithm that monitors spike activity in real-time, using data from the HD-MEA (Fig. 6.3). This algorithm is meant to demonstrate a therapeutic use case scenario. When a pre-defined spike-threshold is detected, the algorithm triggers illumination of the slice. Spike activity was measured by counting the total number of 5-rms spikes that occurred in 10 seconds across all the electrodes on the HD-MEA.

Experimentally, this threshold was to be 2 to 4 times above the average baseline 5-rms spike activity for 1 minute prior to application of bicuculline. After the drug was applied, activity quickly surpassed this threshold. After the threshold is surpassed for a 10-second window, the algorithm triggers 10 seconds of illumination. Afterward, the algorithm goes back to monitoring activity. This algorithm is intentionally simple in nature to provide a proof of concept that user-defined signals can be detected in real-time using the HD-MEA interface with this *ex vivo* model in a closed-loop process.

6.4.9 Optogenetic Power Density Measurement and Calculation

Power output for the optical fiber was measured with Thorlabs meter PM100D with sensor S130C. The power density (mW/mm^2) values of the light presented here were calculated by dividing the measured power by the cross-sectional area of the fiber, using this formula:

$$\begin{aligned} &\text{For multimode fiber with } 200\,\mu\text{m core:} \\ &\text{Beam radius } r = \tfrac{200\,\mu\text{m}}{2} = 100\,\mu\text{m} = 0.100\,\text{mm} \\ &\text{Average power } P_{\text{avg}} \\ &\text{Surface power density } = \tfrac{P_{\text{avg}}}{\pi r^2}\,\text{mW/mm}^2 \end{aligned} \tag{6.1}$$

where P_{avg} is measured power and r is 1/2 the fiber core diameter.

A Python script was used to automatically control the light intensity with the Arduino, take samples with the Thorlabs PM100D, and plot the calibration curves for output power. The calibration data along with parameters of the hardware (the fiber core diameter, LED wavelength, LED driver max current limit, etc.) are saved in a separate calibration CSV file. The user must import the calibration data CSV file to start an experiment. Power density (mW/mm^2) is calculated each time by the Python script using the formula. The user can measure different LEDs and use the calibration files to convert between intensity (0-1 value) and

mW/mm^2 values during experiments and analysis.

6.4.10 Data Acquisition

Neuronal activity was sampled simultaneously at 20kHz from multiple electrodes on the HD-MEA for both action potential and local field potential bandwidth. During the experiment, an activity scan assay using MaxLab Interface across all 26,400 electrodes was performed first, and then a maximum of 1,024 available channels were manually selected to record from the most active areas spread across the MEA. Closed-loop seizure detection and optical intervention started after the assay from a custom Python script. After the experiment, raw activity data and optical stimulation timestamps were saved to an hdf5 file on local memory. The optical light protocol was written into a separate CSV logging file pairing with the raw data (see section Design of Optogenetic System).

6.4.11 Spike Sorting

Kilosort [168] was used for sorting the raw data into single unit activity. Since the high-density MEA can record one neuron from tens of channels, it is common that the spikes from many neurons overlap in time for a single channel. The template matching and clustering algorithm in Kilosort2 can distinguish spikes between different neurons based on their waveform and assign them to individ-

ual clusters. Raw data were bandpass filtered with 300 - 6000Hz and sorted in Kilosort2 with a voltage detection threshold of 6 RMS over the baseline. Spike sorting was performed on the Pacific Research Platform computing cluster with an NVIDIA GeForce GTX 1080 Ti GPU. For spike sorting, both manual and auto-curation techniques were applied. Kilosort2's result was manually curated using Phy GUI [199] by experienced electrophysiology researchers. The quality metrics [216] for saving high-quality units are based on the shape of the spike waveform, firing rate, and interspike interval distribution.

6.4.12 Activity Heatmaps

Activity heatmaps in Figure 6.1 and Figure 6.3 show the spatial distribution of significant voltage events and were generated using the same method in Chapter 5, Section 5.4.8.5.

6.4.13 Statistics and Reproducibility

Sample sizes were maximized based on the availability of human brain tissue samples. There was no randomization. Samples were processed and experiments run in the order that patient tissue became available. No statistical method was used to predetermine sample size, but our sample sizes are similar to those reported in previous publications [116, 254, 91]. The experiments were not ran-

domized. Data collection and analysis were not performed blind to the conditions of the experiments. Much of the statistical analyses involved comparing neuronal activity during a time period during which light was shone on the slice and comparing that data to periods of time immediately preceding and following this "light ON" time period. As such, knowing these exact time-points was necessary for accurate analysis. Data distribution was assumed to be normal but this was not formally tested.

6.4.13.1 Firing Rate and Amplitude

To compare firing rate and amplitude (Fig. 6.3 and E.1, E.2, E.3) across multiple trials for the groups "pre", "light-ON," and "OFF" we calculated the mean firing rate (and spike amplitude) of each recorded neuronal unit across trials in each slice for their respective experimental conditions. We then used a two-tailed, paired t-test with the t.test() function in R. To correct for multiple comparisons, Holm-bonferroni correction for multiple comparisons p.adjust with method= "holm". The N for each individual trial comparison was calculated from the number of units recorded per trial and is listed in figure legends. This was done in RStudio 2022.07.1 Build 554.

6.4.13.2 Waveform Cluster Association with GCL

To assess the association between identified waveform clusters (Fig. 6.3.2) and their anatomical localization within the granule cell layer (GCL) of the dentate gyrus, we used R (Version 2022.07.1, Build 554). Given the binary nature of our dependent variable (presence vs. absence of a unit within GCL), we used logistic regression analysis. This choice was predicated on the need to understand the extent to which belonging to a specific cluster could predict the likelihood of a neuronal unit being located in the GCL, with clusters serving as categorical predictor variables in the model. Prior to analysis, neuronal unit data were rigorously cleaned and formatted. Each unit was classified into one of 12 clusters based on waveform features, with this classification serving as independent variables in our subsequent logistic regression model. The dependent variable was binary, denoting the anatomical attribution of each unit to either the GCL (1) or other hippocampal regions (0). Logistic regression was then performed using the glm function in R, specifying a binomial family to accommodate our binary dependent variable. The model included one intercept and individual coefficients for each cluster, allowing us to estimate the odds ratio of GCL localization for units in each cluster relative to the baseline condition (absence from GCL). To address potential Type I errors due to multiple comparisons—given the 12 clusters analyzed—we implemented a p-value adjustment using the Benjamini-Hochberg

method. Adjusted Confidence intervals and p-values were calculated and reported in Table E.3.

6.4.13.3 Waveform Cluster Association with Opto Response Clusters

To examine the association between neuronal unit classifications based on waveform cluster identity (Fig. 6.3.2) and opto-response cluster identity (Fig. 6.3.3), we employed a two-step statistical approach. Initially, a Chi-square test of independence was applied to a contingency table representing the distribution of units across the predetermined cluster identities (RStudio function: chisq.test). This test assesses the null hypothesis that waveform and opto-response cluster identities are independent of each other across the entire dataset. Given the categorical nature of our data, where each unit is classified into discrete clusters based on spike waveform morphology and optogenetic response, the Chi-square test provides a suitable framework for detecting overall patterns of association between these two classification methods. However, the Chi-square test alone does not indicate which specific cluster associations contribute to the overall significance. Thus, we conducted a post-hoc analysis using standardized residuals, which in this context function analogously to z-scores. For each cell in the contingency table, the standardized residual calculates the number of standard deviations the observed frequency is from the expected frequency, under the assumption of independence. These residuals thus provide a measure of the magnitude and direction

of deviation for each cluster association, enabling us to identify specific pairs of waveforms and opto-response clusters that are associated more or less frequently than would be expected by chance alone. Standardized residuals are computed as follows:

$$\text{Standardized Residual } = \left(\frac{O-E}{\sqrt{E}}\right) \tag{6.2}$$

Where O represents the observed frequency in each cell, and E denotes the expected frequency, calculated based on the marginal totals under the assumption of independence. We applied a Bonferroni correction to control for the family-wise error rate. This correction adjusts the significance threshold by dividing the conventional alpha level (0.05) by the number of comparisons made. A comparison is considered statistically significant if its absolute standardized residual exceeds the critical value derived from the Bonferroni-adjusted alpha of 0.05.

6.4.14 Kullback-Liebler Divergence and Phase Coherence (KLD)

To represent phase coherence events in time of the Local Field Potentials (Fig. 6.3g-i), we first constructed an analytic (complex-valued) time series using the Hilbert transform extension. We then extracted the instantaneous phase distributions at each instant and measured the divergence between these and a uniform

null hypothesis using the Kullback-Liebler divergence (KLD). Let X be a binning of the interval $[0, 2\pi]$. Furthermore, let $P_X(t)$ be the probability distribution of the phase angle values at time t, and let Q_X be the uniform distribution with respect to X. Our Entropy-based metric of coherence across time is defined as

$$K(t) = D\left(P_\chi(t) \| Q_\chi\right) = \sum_{x \in \chi} P_\chi(x) \log\left(\frac{P_\chi(x;t)}{Q_\chi(x)}\right) \tag{6.3}$$

By inspection of the polar histograms, it was determined that, in many cases, the nature of the distribution deviated considerably from a von Mises distribution, making the p-value a misleading measure of coherence. In the field of mathematical statistics, the KLD serves as a statistical distance, quantifying the discrepancy between a given probability distribution P and a reference probability distribution Q, making it a better indicator of phase coherence when the reference Q is chosen to be uniform.

6.5 Conclusion

We describe an approach for using human organotypic brain tissue as an experimental research platform for optimizing approaches to modulate neural activity at the network level in human hippocampus. Building on advances in culture techniques for maintaining viable human organotypic brain slices *ex vivo*, we eval-

uated the effectiveness of AAV-mediated delivery of inhibitory channelrhodopsins expressed in a subset of glutamatergic neurons to exert network-level effects in hyperexcitable conditions. By integrating HD-MEA recordings with a custom system for optogenetic control, our experiments demonstrate a robust platform for high-resolution analysis of network activity and cell type-specific optogenetic manipulation in human hippocampus.

Optogenetics enables high spatiotemporal control over neural activity. Targeting local circuits has been shown to decrease epileptiform activity in non-human model systems [116, 115, 254, 255, 237], but the application of optogenetics to human neurons has been limited. Two studies have used patch-clamp recordings from single neurons to show excitatory optogenetic control of human neurons at a single cell level [8, 231]. Hyperpolarizing, potassium-specific, kalium channelrhodopsins are a new tool in the optogenetic armamentarium [67, 242]. Their inhibiting effects may be relevant to diseases of neuronal hyperactivity, such as epilepsy. This study demonstrates that optogenetic inhibition of human neurons can be used to modulate network-wide neuronal activity in human hippocampal slices.

The ability to record dozens to hundreds of neurons simultaneously is one of the advantages of the HD-MEA recording platform described here. Such high-throughput methods may be effective for hypothesis generation about the neu-

ronal ensemble and cell-type responses that can be validated with patch clamp or patch-seq[28] based experiments. We used clustering techniques to leverage these advantages of the platform described here. We probed whether differences in neuronal cell type might contribute to differences in optogenetic response in our data since many factors can affect neuronal responses, even to the same ligand [194]. The waveform clustering method distinguishes putative neuronal cell types based on extracellular spike-waveform features (Fig. 6.3.2) [123, 126]. To test whether the clustering results were reasonable, we used the anatomic localization of our slice recordings. The granule cell layer is composed mostly of granule cell neurons, which are not typically found elsewhere in the hippocampus [261, 152, 96, 154]. Comparing the distribution of waveform clusters from recordings over the GCL to recordings not over the GCL, 5 clusters were significantly associated with localization over the GCL (Fig. 6.3.2), suggesting these may represent GCL neurons.

We used an unsupervised clustering (HDBSCAN [143, 144, 70, 29]) approach to distinguish patterns of neuronal response to optogenetic HcKCR1 activation that may not be captured by firing rate averages. Rather than simply clustering into responders and non-responders to slice illumination, this approach yielded 5 clusters (Fig. 6.3.3). The GCL waveform clusters were overrepresented in opto-response cluster 3 (Table E.3), which had on average high baseline firing rate and modest reduction during slice illumination (Fig. 6.3.3b,c). This sug-

gested that cell-type –in this case granule cell identity – may play a role in optogenetic response to HcKCR1 activation, although activity-state at the time of slice-illumination cannot be ruled out based on these analyses [67]. Single nucleus sequencing data suggests that granule cells typically express CAMK2A at high levels compared to other hippocampal neurons [10], such that promoter gene expression does not completely explain this modest reduction in firing rate seen during HcKCR1 activation in putative GCL neurons. These clustering techniques explain some of the heterogeneity of network and neuronal response to HcKCR1 activation in a subset of excitatory neurons, but there are limits to the conclusions that can be drawn from them. Our initial hypothesis was that the HDBSCAN analyses of firing rate response would yield two distinct clusters of responders and non-responders to light-ON conditions that might serve as a surrogate for HcKCR1-expression. The results, however, present a more complicated picture. Cell-type, HcKCR1-expression, and connectivity between neurons expressing and not expressing HcKCR1 are all likely contributing to the larger picture. Additional analyses of how individual neurons respond and influence one-another will be necessary to make conclusions of how manipulating a subset of neurons in a hippocampal slice affects network activity.

The present work utilizes hippocampi resected en bloc from patients with drug-resistant temporal lobe epilepsy. Clinically, these hippocampi have been de-

termined to be likely or definitively involved in generating seizure activity. By this definition, the hippocampi recorded may have physiologic differences from what might be considered normal physiology or connectivity in non-epileptic human tissue. While this caveat should be noted when making biological conclusions about hippocampal function, it should also be noted that the intended target for prospective epilepsy therapies is epileptogenic hippocampi. This makes the preparation presented here an optimal model for pathologic insights but perhaps limited in regard to normal hippocampal physiology.

Emerging strategies to develop AAVs with improved fidelity and robustness [269] harness methods for screening synthetic libraries of capsid proteins, as well as enhancer elements [268, 269, 146, 46, 49]. AAV gene delivery studies have thus far focused on visualizing transduced neurons and describing their relevance with regard to normal CNS physiology [65, 146, 46, 49, 38]. Such investigations would benefit from characterizing how these tools can be utilized in pathologic circuits. *Ex vivo* cultures of human brain slices may both accelerate the development of such tools and serve as a platform for investigating the circuit-level effects of AAV-mediated, gain-of-function gene delivery. The techniques described herein allow for a layer of functional screening of AAVs for gene delivery by combining validation of human brain tissue expression with the potential to measure electrophysiologic activity and circuit-level effects.

In conclusion, primary human tissue can serve as an experimental platform for optimizing and testing strategies to modulate network activity with the long-term goal of de-risking potential therapeutic interventions. Emerging technologies could enable rapid and scalable genetic access into cell types that could be tested in such ex vivo preparations. Here, we describe a scenario whereby AAV-mediated delivery of inhibitory channelrhodopsin into a subset of glutamatergic neurons can be used to demonstrate network-wide activity modulation in the human hippocampus. These techniques were previously relegated to animal modeling experiments. This study highlights the potential for human brain tissue method to serve as a viable model for illuminating human brain neurophysiology.

Chapter 7

Conclusion

7.1 Summary

This thesis captures platform development progression and experiments for *in vitro* electrophysiology on the Internet of Things (IoT). The progression includes creating lightweight and low-cost IoT-based hardware and recruiting off-the-shelf hardware to work with IoT, designing an IoT Cloud Laboratory infrastructure, and applying it to run multimodal integrated experiments.

This work aimed to increase the reproducibility of experiments through automation, standard data management and analysis workflows, and combining different measurement and perturbation techniques. We demonstrated this paradigm with experiments screening optogenetic interventions for epilepsy and observing

longitudinal organoid neuronal activity.

7.2 Future Work

Current work in progress focuses on disseminating the technology by applying the IoT Cloud Laboratory paradigm to new devices and experiments. New devices may include custom-built microscopes, ion and drug delivery systems, and fluidic feeding supporting more significant numbers of organoids (i.e., 24 or 96 per plate).

The modular nature of the IoT Cloud Laboratory ecosystem allows for endless integrations and combinations of experiments and protocols. Feedback loops enable equipment to function and compensate for errors, which is critical for long-term automation to maintain target operating conditions. Due to the networked nature of IoT devices, remote programs can analyze data and optimize experimental conditions by sending MQTT commands to devices to adjust the flow and progression of experiments as motivated in Figure 1.2. Large Language Models can also translate human speech and commands to device commands, increasing the accessibility of controlled experiments without users needing to write code or navigate menus. Integrating artificial intelligence systems with this IoT platform could accelerate scientific discovery by allowing computers to interact with live biology, advancing our data collection and helping rapidly test hypotheses in neuroscience.

Appendix A

Electrophysiology Platforms Review

Comparing electrophysiology platforms side by side is challenging because each system fits a specific niche and requirements for a particular workflow. Different platforms arose as solutions to different problems, challenges, and user needs. Piphys arose due to the need for automation of experiments, integration with other IoT sensors, and flexible recording equipment that can be used in a fleet for longitudional study of many *in vitro* replicates.

Table A summarizes electrophysiology systems comparable to Piphys. The Axion Maestro Edge is designed as an out-of-the box bench top electrophysiology system with maximum comfort and usability. Although it has the highest price

per channel, it is also an incubator. The MaxWell MaxOne has a CMOS sensor with a high density of electrodes [265, 163] [1]. The Intan RHS controller and Intan RHD USB interface board with headstages require more effort to calibrate, ground, and shield. Unlike Axion and MaxWell, Intan designs and code are open source. Intan bioamplifier chips have been used in many open source systems, including Intsy, Willow, Open Ephys, and now Piphys. Intsy was designed for measuring gastrointestinal (EGG), cardiac (ECG), neural (EEG), and neuromuscular (EMG) signals [54]. Willow was designed for high channel count neural probes and resolves the need for many computers by writing data directly to hard drives [109]. Open Ephys is an alternative system to Intan integrating more features into their GUI for closed-loop experiments and plugin-based workflows [217] [2]. Noise measurements for Piphys, Intan, and Axion were experimentally recorded, while noise measurements for Intsy, Willow, MaxWell, and Open Ephys were cited. Intan claims 2.4μV RMS as typical in the datasheet for their chips [3] which was likely inherited into Open Ephys documentation. The whole system noise for Open Ephys is not explicitly mentioned in documentation.

[1] https://www.mxwbio.com/products/maxone-mea-system-microelectrode-array/
[2] https://open-ephys.org
[3] https://intantech.com/files/Intan_RHD2000_series_datasheet.pdf

Closed-loop feedback is currently possible on the MaxWell MaxOne, the Intan RHS Controller, and Open Ephys on the order of 10-200 ms. NeuroRighter [197] [4] is not featured in the table, but was one of the first inspirations for closed-loop feedback platforms [198, 162, 161]. Key authors from NeuroRighter eventually joined the Open Ephys project, which is the most up to date. NeuroRighter has not been updated or published with for more than 5 years and many of the components listed on the Wiki [5] are not longer for sale (for example, the company providing the key bioamplifier chips no longer exists). However, NeuroRighter did use PCI-6259 or PCIe-6259 interfaces providing 4 ms closed loop delay [162] [6]. Closed-loop systems inside FPGAs can achieve very small propagation delays (ns), but the interface speed is limited by the chip sampling rate, which still provides around sub-millisecond delay performance in FPGA-based closed-loop systems [184].

Future versions of Piphys could include closed-loop feedback. The delay time could aim for sub-millisecond range due to use of more modern PCIe interfaces.

While feedback within a time window of 10-20 ms is generally effective for the induction of long-term potentiation (LTP) and long-term depression (LTD) [24, 142, 31, 57], the saved time with a quick interface enables the computer to fit in more complex calculations.

[4] http://rzellertownson.github.io/neurorighter/
[5] https://sites.google.com/site/neurorighter/
[6] https://sites.google.com/site/neurorighter/user-manual/closed-loop-guide

Piphys is the only electrophysiology device collection that supports Internet of Things (IoT) software integration out of the box. The IoT hardware modules and cloud software allow for horizontal scalability, enabling long-term observations of development, organization, and neural activity at scale, and integration with other IoT sensors. Piphys RHD has a low entry cost, and the cost per channel can also be significantly lowered by increasing the number of channels supported per device. This would be accomplished by engineering an inexpensive FPGA into the controller shield, as planned in the Piphys FPGA designs, to sample multiple bioamplifier chips and buffer those readings for the Pi. Piphys can have a large cost reduction if extra specialty connectors and adapters are removed and Intan chips are planted directly into the main circuit board.

Table A.1: **Electrophysiology platforms review.** Comparison of Piphys features to several commercial and open source electrophysiology systems. Sampling Rate and Channels columns show the maximum numbers for all systems. Stimulation is assumed to be electrical (optogenetic add-on modules not counted). Closed-loop delay is an average delay across multiple trials. *Noise shown on Open Ephys website is the amplifier input noise for Intan RHD2132 bioamplifier chip, not the whole system noise. ¶The Piphys Pilot is deprecated and will not be highlighted in comparison discussions due to its high system noise which is unacceptable for neural recording. †RMS noise recorded experimentally. ††Expected experimentally for a future design. **Based on MaxWell organoid demo presentation. ‡ With PulsePal [205] stimulation module limited to 2 triggers and 4 external stimulation electrodes. §Possible but has not been implemented or tested yet.

Platform	**System Noise (μV RMS)**	**Sample Rate (kHz)**	**Channels**	**Cost (USD)**	**Cost per Channel**	**Open Source**	**IoT**	**Stim**	**Closed-Loop Delay**
Piphys Pilot ¶	>1,000 †	15	15	$819	$55	Yes	Yes	No	N/A
Piphys RHD [244]	2.36 ± 0.4 †	15	32	$1,545	$48	Yes	Yes	No	N/A
Intsy [54]	6-8	2	64	$2,500	$39	Yes	No	No	N/A
Intan RHD Interface[1]	3.21 ± 0.66 †	30	256	$10,295	$40	Yes	No	No	N/A
Intan RHS Controller[2]	3.21 ± 0.66 †	30	128	$14,660	$115	Yes	No	Yes	200 ms
Open Ephys [217]	2.4 *	30	512	$15,545	$30	Yes	No	Yes ‡	11 ms ‡
Willow [109]	3.9	30	1024	$20,480	$20	Yes	No	No	N/A
MaxWell MaxOne [265, 163][3]	4-6 **	20	1024	$68,000	$66	No	No	Yes	105 ms
Axion Maestro Edge[4]	1.12 ± 0.18 †	12.5	384	$70,000	$182	No	No	Yes	N/A

[1] https://intantech.com/RHD_USB_interface_board.html
[2] https://intantech.com/stim_record_controller.html
[3] https://www.mxwbio.com/products/maxone-mea-system-microelectrode-array/
[4] https://www.axionbiosystems.com/products/systems/maestro-edge

Appendix B

Piphys Supplementary Materials

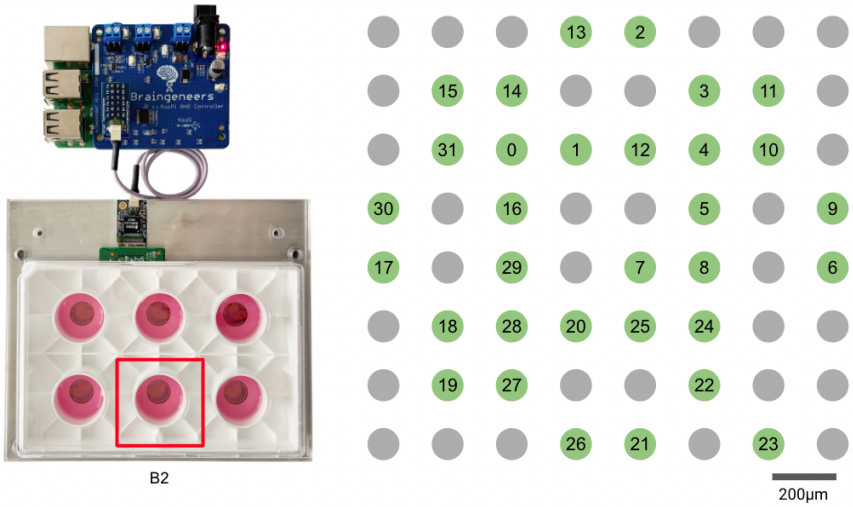

Figure B.1: **Piphys Axion plate mapping.** The Piphys electrode adapter for Axion connects to a 32 channel subset in well B2. The right panel shows the channel numbering in the recorded data with respect to electrode position. Electrodes inside the well have a 30 µm diameter, 200 µm center-to-center spacing.

Many electrode probes have been designed to interface with tissues to provide

measurement points for voltage recordings [259, 130, 190, 125, 170]. Piphys can be used with 3D Flexible MEAs [170], tetrodes [79], silicon probes [259], and MEA plates shown in Figure B.2. Future work with research collaborators could expand the number of different electrodes types for long-term culture of the biological sample.

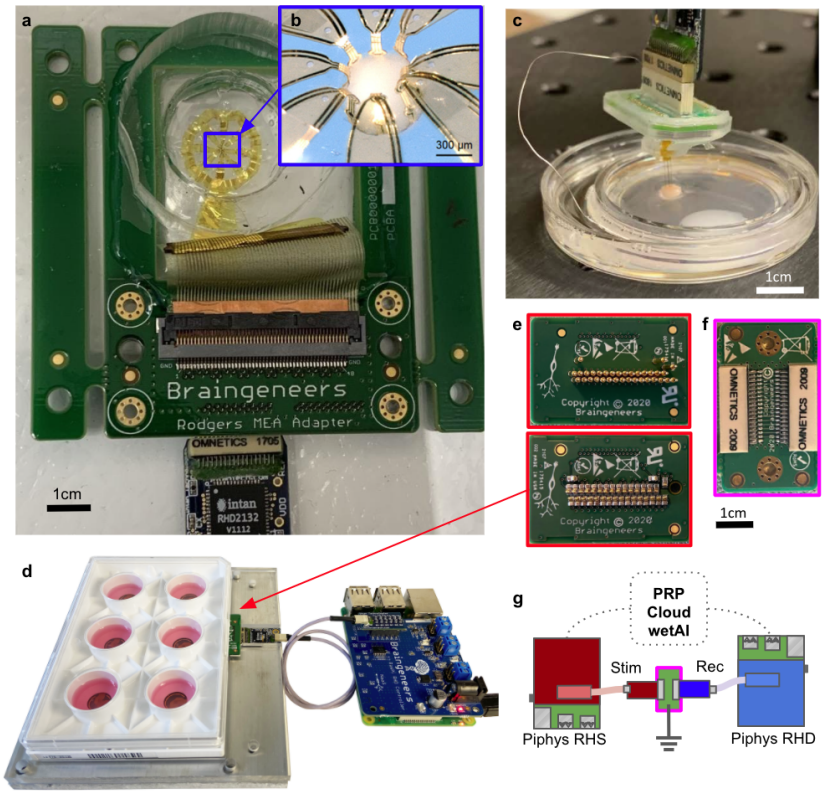

Figure B.2: **Piphys is compatible with any Omnetics electrode probes.** **(a)** Collaboration with Rogers Lab. Adapter is built to interface flexible 3D electrode arrays with Intan headstages. **(b)** Organoid positioning inside the flexible 3D electrode array by Park, Y. et al [170]. **(c)** Collaboration with Hengen Lab. Tetrode electrode probes directly interface with Intan headstages. The tetrodes are shown during an experiment with an organoid and mouse brain slice. **(d, e)** Adapter built for Axion plate, featured in two pin varieties: pogo (**e**, top) and finger (**e**, bottom). **(f, g)** The loopback adapter (outlined pink) is useful for testing stimulation and recording functionality of Piphys devices working in a closed loop.

Appendix C

Integrated System

Supplementary Materials

C.0.1 Computer Vision for Fluid Level Detection

C.0.1.1 Camera details

A 16MP camera (B0290, Arducam) and a set of conical tubes are fixed 12 mm apart from each other on an optical breadboard (SAB10x30-M, Base Lab Tools). The camera was specifically configured without autofocus, with its focus statically set at 344 on a scale from 1 to 1023. A two-second warm-up period stabilizes the focus setting before a picture is taken. Exposure was set at 45 on a scale from 1 to 5000.

C.0.1.2 LED panel details

A 16x16 LED matrix (WS2812B-16x16ECO, BTF-LIGHTING) covered with 0.1mm thick polyester diffusion film (B08PTCGTX9, RENIAN) creates a uniformly illuminated background (we used 8 sheets of diffuser film spaced 1 mm apart by double-sided foam mounting tape). The LED panel is approximately 5 mm behind the conical tubes.

The LED matrix was set to display a color gradient to best contrast fluid contents inside the conical tube, particularly in the cone-shaped lower area of the conical tube, which is thinner and appears lighter in color. The red color component of each LED matrix pixel was set based on its row position within the matrix, beginning with an initial red value of 221 out of 255. The red color intensity was reduced by two units for each row upwards, creating a gradient effect. Thus, the final color of each pixel was a combination of this dynamically adjusted red value and fixed green and blue values of 140 and 180, respectively. Furthermore, the LED panel's brightness was set to 50% to prevent overexposure in the captured images.

C.0.2 Assembled Devices and Custom 3D-printed Components

All custom accessories were 3D printed (Form 3B+, Formlabs) with Biomed Clear V1 material (RS-F2-BMCL-01, Formlabs), except for the collection tube and camera stand in the refrigerator printed in BioMed Black V1 (RS-F2-BMBL-01, Formlabs). The parts were printed flat on the build plate to reduce support material. Alignment grooves between the insert and lid described in the Microfluidic culture chamber form a hole which also facilitates 3D printing by removing the formation of suction cups to the resin tank.

C.0.3 Microfluidic Culture Chamber

The microfluidic culture chamber assembly allows media to be exchanged inside the HD-MEA well. The chamber assembly consists of a microfluidic module, glass rod lid, and catch tray (Figure 5.2B, C).

The microfluidic module is placed inside the HD-MEA well, creating a media chamber and fluid path into and out of the chamber. Media from outside the incubator travels to the fluidic insert along 0.030" ID and 0.090" OD Tygon tubing (AAD02119-CP, Cole Parmer); the length of the tubing is approximately 100 cm. The tubing attaches to the fluidic insert using PEEK fittings (EW-02014-97, Cole Parmer) wrapped (counter-clockwise) in PTFE thread seal tape around twice the

fitting's circumference. The inlet and outlet are raised inside the fluidic insert to create a pool following a geometry published in previous work [210].

The fluidic insert, glass rod lid, and catch tray use silicone O-rings (5233T543, 5233T479, 5233T297, and 5233T585, McMaster) to provide seals against contaminations and leakage. O-rings were rubbed with a minimal quantity of canola oil for lubrication to facilitate installation and enhance sealing performance. The canola oil can be autoclave-sterilized, but it is unnecessary if the O-rings are sterilized post-lubrication (see Sterilization and assembly).

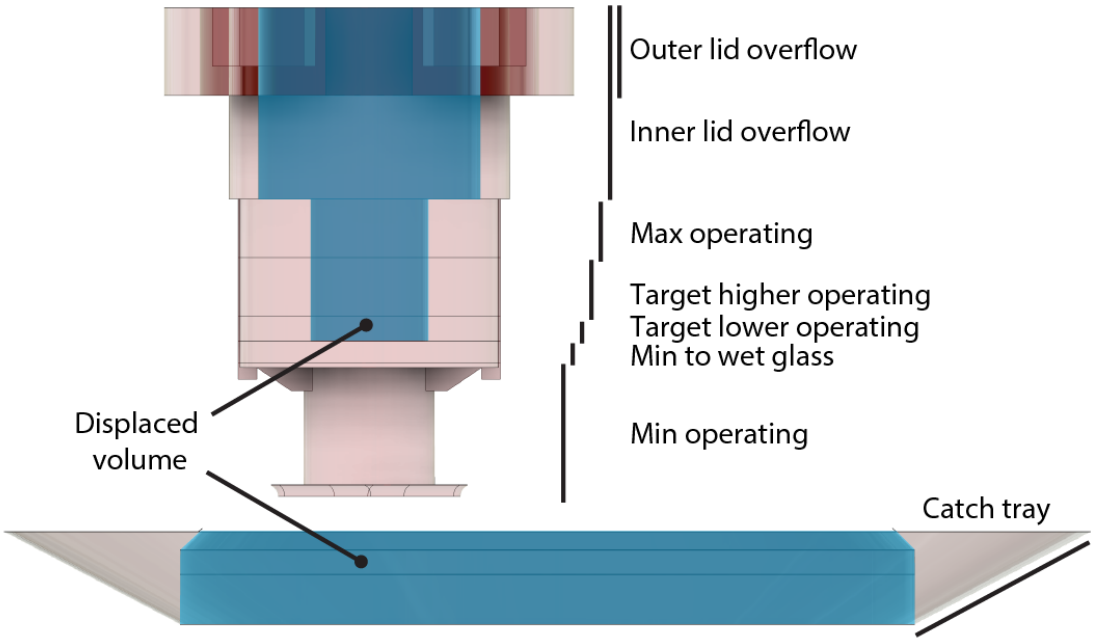

Figure C.1: **Diagram of operating ranges of the microfluidic culture chamber.** Shaded pink areas represent volumes where media is collected. Shaded blue areas mark displaced volumes (where there is no media stored). The numerical volumes for each operating range are listed in Supplementary Table C.1.

Feature	Delta (µL)	Running Total (µL)
Min operating	172.2	172.2
Min to wet glass	94.0	266.2
Target lower operating	88.1	354.3
Target higher operating	204.9	559.2
Max operating	204.9	764.1
Total operating capacity:		**764.1**
Inner lid overflow	345.1	1109.2
Outer lid overflow	464.1	1573.3
Total chip capacity:		**1573.3**
Catch tray	1539.5	3112.8
Total overflowed capacity:		**3112.8**

Table C.1: Numerical operating volume ranges based on the microfluidic culture chamber's 3D model (CAD) measurements. Illustrations of operating ranges are shown in Supplementary Figure C.1. The Feature column lists critical points in the microfluidic culture chamber. The Delta column is the volume space between each feature, and the Running Total column is the volume from the floor to the feature.

C.0.4 Membrane Lid

The membrane lid used for experimental control conditions follows established designs [188], with adjusted dimensions to improve grip, matching material to the microfluidic culture chamber, and high-temperature silicone O-rings instead of rubber. The outer O-ring (5233T683, McMaster) holds the breathable FEP film (23-1FEP-2-50, CS Hyde Company) stretched over the top of the lid. The inner O-ring (5233T585, McMaster) seals the lid and well. The inner O-ring is also rubbed with a minimal quantity of canola oil as described in the Microfluidic culture chamber section.

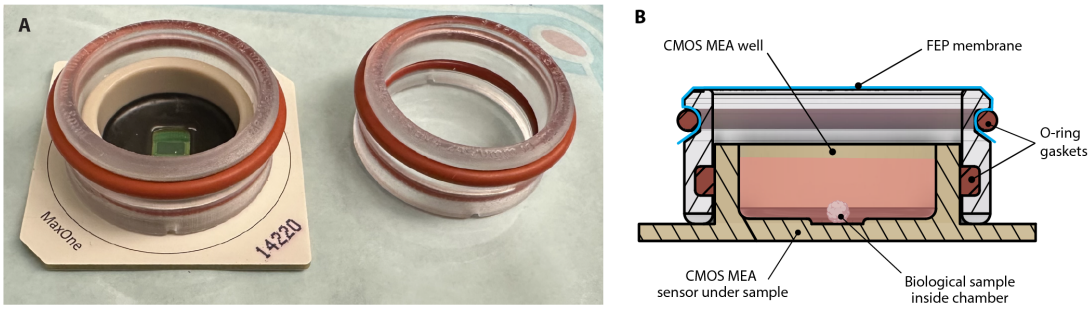

Figure C.2: **3D printed breathable membrane lid used for Controls modeled after designs by Potter (49). (A)** Picture of the membrane lid and HD-MEA. The chamber is comprised of biocompatible 3D-printed parts, sealed by O-rings to the HD-MEA, and imaged through the FEP membrane stretched over the top with an O-ring. **(B)** Cross-sectional rendering depicting the fluid path and position of the sample.

C.0.5 In-incubator Imaging Alignment Holders

The custom alignment holders, designed for two configurations, center a digital microscope over the biological sample on the HD-MEA. Components are screw mounted (91292A134, McMaster) to optical breadboards (SAB10X15-M, SAB15X15-M, Base Lab Tools Inc.) to ensure stability and maintain accurate spacing.

C.0.5.1 HD-MEA off the headstage

The microscope is held over a single HD-MEA by a post and clamp (MS08B, Dino-Lite) mounted with a setscrew and base (SS6MS10, TH15/M, Thorlabs). The custom HD-MEA holder centers it for imaging. Throughout the experiment, HD-MEAs were left resting on each holder. The holder has cut-outs for handling

the chip and also avoids the chip's contact pads to decrease scratching and avoid moist surfaces. The holder also has indicators for the chip's proper rotation with respect to the microscope.

C.0.5.2 HD-MEA on the recording headstage

The custom holder on a post assembly (SS6MS10, TH15/M, TR250/M-JP, Thorlabs) mounts the microscope over the chip on the recording headstage. The custom headstage holder centers both the recording headstage with its attached chip to the microscope.

C.0.5.3 Sterilization and assembly

Before use in tissue culture, components were placed in autoclavable bags (RIT-3565, PlastCare USA) and steam-sterilized at 134°C for 20 minutes or 121°C for 30 minutes based on Formlabs material datasheet specifications. Components were autoclaved, disassembled, and then assembled in a sterile tissue culture hood to avoid deformation or cracking during temperature cycling. Components were transported in an enclosed petri dish (small items) or a sterile autoclaved bag (large items) before being released into the incubator. Components that could not be autoclaved (such as electronics, i.e., recording headstage, microscope) have their enclosures sterilized with hydrogen peroxide disinfecting wipes (100850922, Diversey) before entering the incubator.

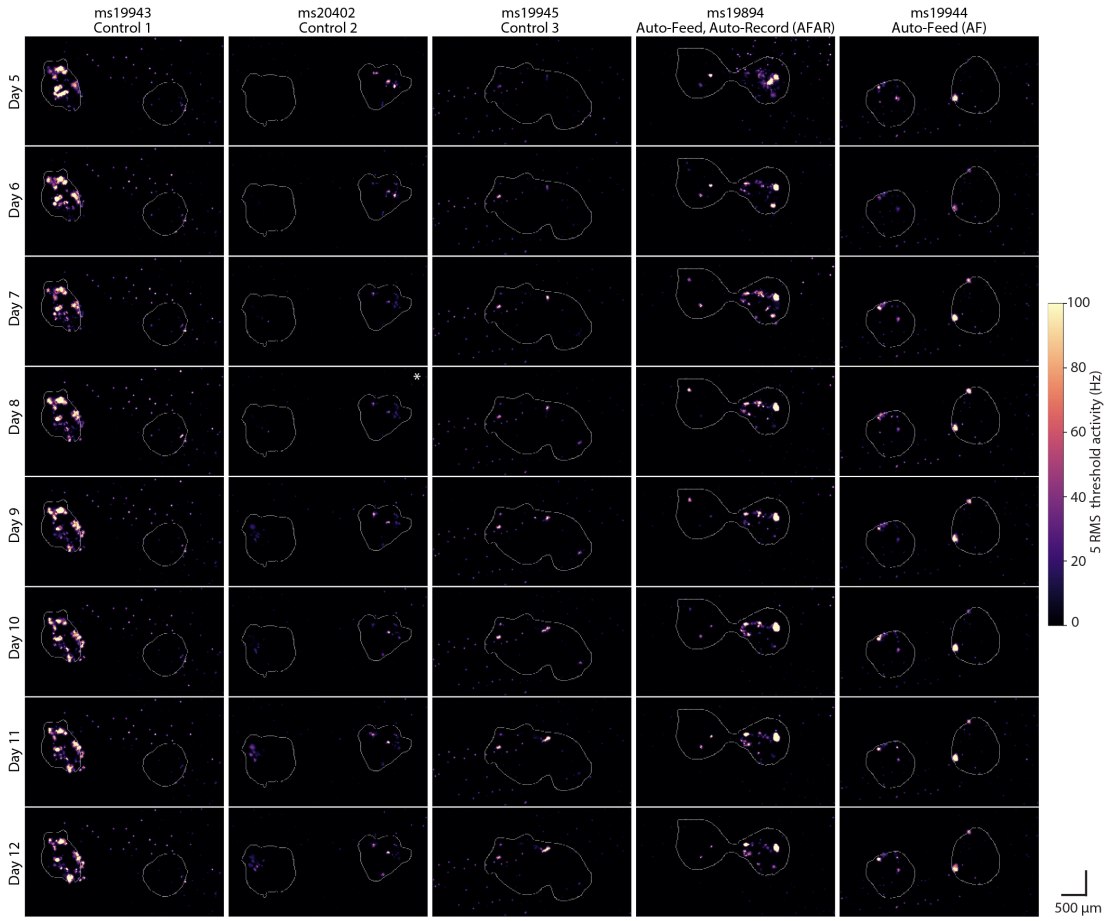

Figure C.3: **Daily activity scans of all chips over all days.** Boundaries of each organoid were outlined and overlaid for orientation.

Appendix D

IoT Device and Messaging Conventions

D.0.0.1 MQTT

Message Queueing Telemetry Transport (MQTT) messages serve as the standard unit of communication in the ecosystem (Figure 5.4B, orange). MQTT allows devices and services to communicate without direct dependencies between each other by using a common publish/subscribe medium. MQTT clients are the devices or software entities that connect to the broker to send (publish) or receive (subscribe to) messages. Devices and services send messages on MQTT topics, which are hierarchical strings that allow listeners to capture a wide or narrow scope of information. Messages contain a payload with a list of key-value pairs

to structure information. For example, a message requesting a microelectrode array to record has a key for recording duration with a value in minutes. Examples of MQTT topic structure and message JSON payloads are summarized in Supplementary Table D.2; see GitHub for more information[1].

The MQTT broker is the central communication facilitator in the network and coordinates messages between clients. The MQTT broker receives all messages from the clients, filters these messages based on their topics, and then distributes them accordingly to other clients who have subscribed to those specific topics. This setup enables efficient message routing and ensures that messages reach the intended recipients without the senders needing to know the specific details of the recipients.

Clients can be sensors, actuators, applications, and services (like UIs or analysis), or any other devices capable of network communication. The organization is future-proof because MQTT allows the creation of new services and devices and uses information available without changing any services (logging, UI, dashboards, analysis of traffic, etc.). Furthermore, message bridges can be employed to convert MQTT messages to other messaging APIs such as text messaging, email, or work chat applications like Slack (see Messaging bridge).

[1] `https://github.com/braingeneers/integrated-system-v1-paper`

D.0.0.2 IoT device-class

The primary function of a *device-class* involves listening for job requests, executing them, and saving the resulting data to the cloud. This data includes measurements (e.g., images, voltage recordings) and log entries detailing device actions (e.g., cell culture feeding events). By consolidating features, the *device-class* framework simplifies the creation of new devices and enables easy control, updating, and interoperability. The Python *device-class* provides standard features across all IoT devices:

- a state machine defining standard behavior for a device (i.e., defined states and transitions between states triggered by defined events)
- listening, processing, and responding to MQTT request messages
- updating the database to reflect current device state (shadow)
- executing jobs immediately or on a recurring schedule with timing accurate to network time protocol (NTP)
- data upload/download with queueing and retry mechanisms
- optimizations: threading for multi-tasking and enhanced responsiveness, error handling

A child of the parent *device-class* will inherit all basic functionality, and may add additional features. For instance, a camera *device-class* child performs all actions that a *device-class* can, plus it knows how to handle a request to take a picture.

Having a common parent class consolidates similar features for different devices and allows for easier updates because all devices use the same core code library. The *device-class* code is available within the Braingeneerspy Python package on GitHub[2]. For state machine states and request commands see Supplementary Tables D.1 and D.2.

Devices can work in a fleet. As each device has the same core software with complementary behaviors, they integrate seamlessly, similar to how uniform building blocks can easily snap together. Devices can ask each other to yield while they perform sensitive actions (Figure 5.4D). Similarly, devices can perform services for each other in a coordinated manner. For example, midway through a recording, a microelectrode array device could ask the pump to deliver a drug. Devices can perform rudimentary decision-making to simplify overarching management. Devices post status and information to an open MQTT topic, allowing services and devices to build on and interface with those devices without altering existing devices and services. Devices can use each other to make sure the experiment is on track across multiple modes of sensing, for example the pump using the eyes

[2]`https://github.com/braingeneers/braingeneerspy`

of the camera to ensure pumping succeeded.

D.0.0.3 Pre-experiment workflow

Figure 5.4A illustrates the state transitions of a generic device during operation. It begins in the SHUTDOWN state, moving to IDLE, where it waits for user setup verification. Post-setup, it transitions to PRIMED, ready for experimental involvement. In the READY state, the device listens for experiment-specific MQTT messages, ignoring external recruitment until released with an END message. Devices can communicate collectively via MQTT topics for coordinated actions. Transitioning to WAITING occurs upon receiving a pause command, halting job execution. The device moves to EXEC when starting a job, returning to READY upon completion. Data uploads are managed independently of state changes, ensuring continuity even during outages. Devices can exit an experiment at any stage, reverting to IDLE or SHUTDOWN, with data upload tasks resuming upon restart. Figure 5.4A describes a generic device (e.g. a scientific instrument) and how it transitions between states during operation. On device start, the device transitions from SHUTDOWN state to IDLE. In the IDLE state, the device is waiting for a user to verify or install physical prerequisites. The IDLE state ensures the user performs the necessary setup of their device to maintain safety and usability. For example, a pump may wait in IDLE state until a user checks and confirms that the pump is clean and proper reagent bottles are connected. On

the other hand, a camera may not have any prerequisites and would immediately transition to the next state, PRIMED. In the PRIMED state, the device has all the prerequisites to perform its job and waits to be called into an experiment. Devices listen on their default device MQTT topic. Once it receives a correctly formatted 'start' MQTT message (see 'START' message in Supplementary Table D.2), it can transition to READY.

D.0.0.4 Experimental workflow

When the device transitions to READY state, when it listens to an MQTT topic for the experiment. It will refuse requests to be recruited to other experiments until it is released from the current experiment by an END message (see END message in Table D.2). This ensures other users don't accidentally disturb or recruit an occupied device into a parallel experiment. Switching MQTT topics also ensures exclusivity in incoming messages. The experiment topic structure (see MQTT) allows devices to send a group message addressing all devices. For example, a device or user could send a message to roll-call all devices on the topic (see PING message in Table D.2) or pause all devices while it performs a sensitive action (see PAUSE message in Table D.2). Upon receiving a message to pause, the device transitions to WAITING state, where it does not perform any jobs.

Once a device returns to READY state, it can transition into EXEC state if it receives a job request or has a job request from its schedule. If the device

is in WAITING or EXEC while receiving a job request, it will put the request on the schedule to be executed as soon as possible. During EXEC state, the device is actively executing a job request. Once the job finishes or is stopped (see STOP message in Table D.2), the device transitions back to READY state. Any data produced is queued for upload, protected from internet outages by upload retries with exponential backoff. Uploads occur in the background, independent of device state. A device can begin EXEC on a new job immediately after queueing the previous data for upload. From any state, a device can be terminated from an experiment and return to the IDLE state. At any point in the experiment, if a device is gracefully requested to turn off, it performs a final transition to SHUTDOWN state before halting the program. The device keeps the upload queue saved on disk and will continue unfinished uploads upon restart.

D.0.0.5 Data uploading

Data is saved to a 'diskcache' in memory. Once a file is produced, it is put on the upload queue. The upload queue contains references to files within diskcahe. Typical devices have at least 32 GB of disk memory, far larger than a single file. The queue is restricted to grow up to 80% of the device's memory. Once the memory of the device fills up, older files that were uploaded can become overwritten.

D.0.0.6 Messaging bridge

The messaging bridge serves as an intermediary for communication between different platforms. It is a service that listens to MQTT messages in the IoT environment and translates them into other APIs like Slack.

The Slack bridge allows IoT devices to send notifications to individuals in designated Slack channels. The messaging bridge uses the message broker API and Slack API [220]. The Slack API requires an API key to be registered with Slack and an API bot to be added to the Slack channels of interest. The message bridge listens to an MQTT channel dedicated to Slack messages. When devices want to post a message to Slack, they publish a message on the dedicated Slack MQTT topic with a JSON payload containing the message. The payload can include text and image data. To support images, a link to an S3 object can be passed in the message, and the messaging bridge will then download and attach it to the Slack message. An image can also be sent directly inside the MQTT message, this requires modifying the message broker service's configuration to increase the MQTT message buffer size to accommodate larger KB-sized files. The Slack bridge is a relatively simple service that decouples devices from dependencies on a specific API by communicating using the common message format MQTT.

D.0.0.7 Website

The website's front end is developed using React, a JavaScript library for building dynamic and responsive user interfaces. For the backend, Flask, a lightweight Python web framework, is employed. Flask's simplicity and flexibility make it ideal for our web services. It handles server-side operations, data processing, and interaction with databases.

The system's structure incorporates a message broker API, which is established on the backend side of the architecture. This message broker is responsible for the asynchronous communication and management of all IoT devices connected to the cloud. Additionally, Flask's compatibility with Python enables seamless integration with Python APIs, including the braingeneerspy MQTT message broker.

Through the front end, users can issue commands to the devices, and the message broker API in the backend efficiently manages these requests. The user interface encompasses three main components: the initialization page for entering initial experiment data, the control page for managing devices and monitoring their status, and the visualization page for analyzing experimental data through various graphs. All three pages require a specified experiment UUID (see Figure 5.4).

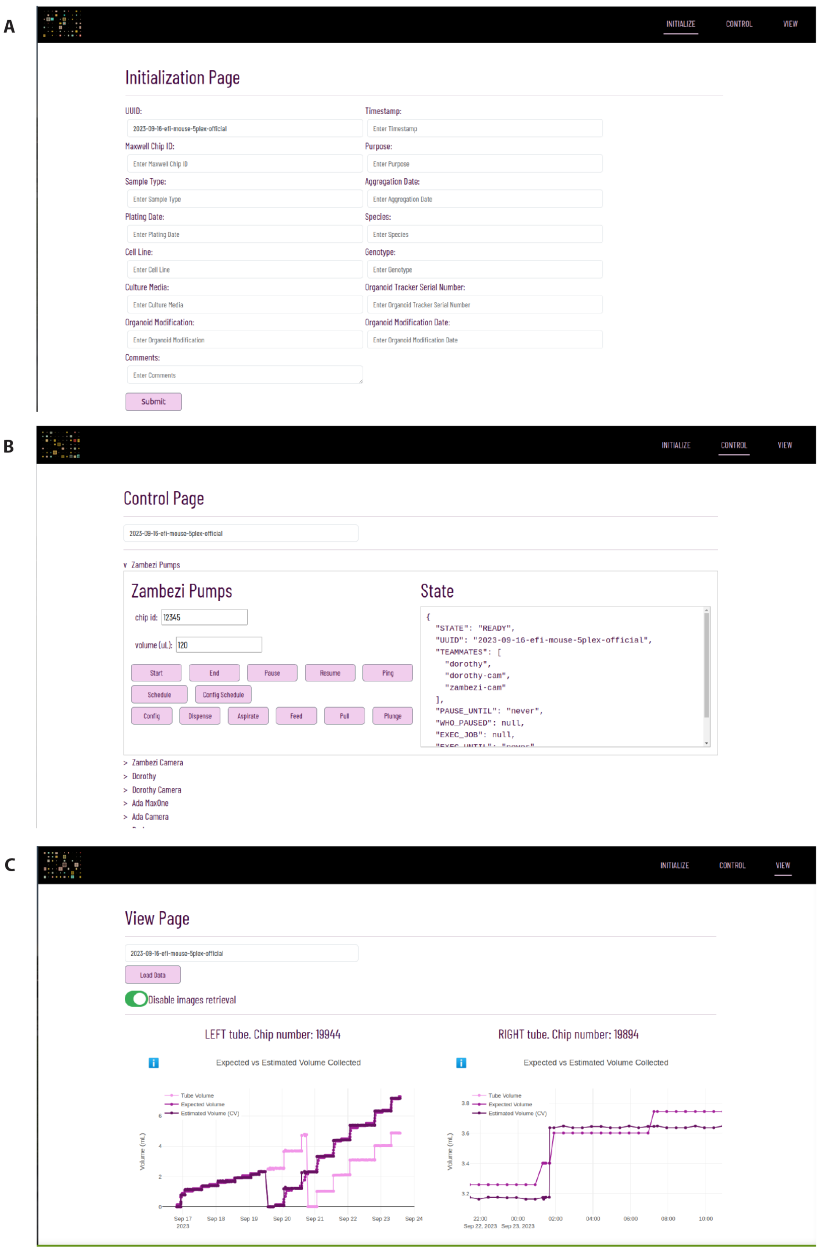

Figure D.1: **Webpage user interface screenshots.** **(A)** Initialization page: Users can input details about the experiment and the biological samples. **(B)** Control page: Users can access and control every device involved in the experiment. **(C)** Visualization page used to track experiment metrics, such as the volume of used media.

Both frontend and backend components are containerized using Docker, ensuring consistency and isolation in different environments. Integration of Cross-Origin Resource Sharing (CORS) is crucial for allowing the React frontend to securely interact with the Flask backend hosted on a different domain.

Initialization page: On the initialization page, users can enter metadata containing experiment and biological sample details, which are compiled into a JSON file and uploaded to cloud storage, serving as a centralized repository for all experimental data.

Control page: On the control page, users can access all the devices involved in the experiment associated with a specific UUID. For each device, users can request the execution of all the commands listed in Table D.2, such as starting, stopping, and pausing the device, as well as scheduling tasks. Additionally, on the control page, users can monitor the real-time status of the device, as outlined in Table D.1.

Visualization page: On the visualization page, users can load data related to the volume estimator from current or previous experiments of a specific UUID. It is also possible to download images on a specific timestamp, allowing for manual monitoring of reservoir tubes.

State	Description
SHUTDOWN	The device has been turned off gracefully and won't respond until it's turned back on.
IDLE	The device is not assigned to any experiments and not doing anything at the moment, and is missing physical prerequisites (i.e., a reagent or piece of hardware) to be able to perform its job.
PRIMED	The device is not assigned to any experiments and not doing anything at the moment, but it has all the physical prerequisites to perform its job.
READY	The device is assigned to an experiment and is ready to execute a command.
WAITING	The device has received a command to PAUSE and is waiting until a given time to resume performing jobs.
EXEC	The device is actively executing a job command.

Table D.1: **Device states.** The *device-class* is structured as a finite-state machine, with a defined set of states (SHUTDOWN, IDLE, PRIMED, READY, PAUSED, EXEC) that describe its status. The finite-state machine reads a set of inputs and changes to a different state based on those inputs. The inputs can be user physical interactions (i.e., button press, linkage of consumables, etc.), MQTT messages containing job requests, or scheduled events.

Command	Description
START*	Initiates an experiment process on a specified device. The device must not be engaged in another experiment and should be in a PRIMED state. If successful, the device acknowledges the request and changes its state to READY.
END†	Ends an ongoing experiment on a device or all devices associated with an experiment UUID. The device(s) will drop current tasks and reset to the IDLE state.
STATUS†	Retrieves the current status, state, associated experiment UUID, teammates, and job schedule. Works in any device state.
PAUSE†	Temporarily halts the device's ability to start working on new commands for a specified duration. If the device is already paused or not part of an experiment, it will return an error. Otherwise, the device will successfully change its state to WAITING.
RESUME†	Requests the device to continue execution after a pause. Only the device that initiated the pause can send a resume command. The PAUSED device will successfully change its state to WAITING.
SCHEDULE†	Adds, clears, or retrieves scheduled tasks for the device. The device will execute the specified task payload at the specified time every X hours or minutes (unless it's WAITING, then it will do backlogged tasks at the easiest convenience). Works in any state.
STOP†	Requests the cancellation of a running task. If there is no task running, an error message is returned.
PING†	Requests the device to respond with a ping message. This is used to check if the device is online and listening to a given topic. Works in any state.
SLACK‡	Posts a message to Slack. The message can contain text and/or an image.

Table D.2: **Generic commands.** The parent *device-class* responds to a generic set of commands. Commands are sent on hierarchical MQTT topics that allow widening and narrowing of scope. We used each experiment's Universal Unique Identifier (UUID) and each device's name as part of the topic. If a device is not part of an experiment, the default UUID is NONE.
* Use MQTT topic: `NONE/device` because no experiment assigned yet
† Use MQTT topic: `UUID/device` or just `UUID` to address all
‡ Use MQTT topic: `TOSLACK`

Command	Device	Description
RECORD	HD-MEA	Performs an electrophysiology recording for a defined period of time.
PICTURE	Camera(s)	Takes a picture from the camera.
FEED	Pump	Performs a cycle of aspirating spent and dispensing fresh media of the pre-configured volume.
ASPIRATE	Pump	Aspirates a specified volume of liquid (mL) from the culture chamber.
DISPENSE	Pump	Dispenses a specified volume of liquid (mL) to the culture chamber.
PULL	Pump	A rapid, full-syringe aspiration to assist pulling media through high resistance or clogs.
SPIKESORT	Spike sorting	Spike sorts a specified dataset stored in S3 using the analysis pipeline.
ESTIMATE	Estimator	Estimates the amount (mL) of media in a collection reservoir by applying computer vision analysis to a specified image of the collection reservoir stored in S3.

Table D.3: **Application-specific commands.** The child *device-classes* extend the top level *device-class*, respond to all genetic commands as well as their instrument-specific commands. New commands can be easily defined and implemented for a specific experimental application by extending *device-class* child. For all commands above, use MQTT topic: `UUID/device_name`.

Appendix E

Optogenetics Platform

Supplementary Materials

PT ID	Age	Sex	ILAE HS† Type	Slice ID	Units	Opsin	Perturbation
A	20	M	type 3	1A	44	n/a	none
B	44	F	type 1	2B	36	ChR2	none
C	40	F	type 3	3C	72	HcKCR1	none
				4C	40	ChR2	none
				5C	65	HcKCR1	bic
				6C	31	n/a	none
D	46	F	No HS	7D	80	HcKCR1	bic
				8D	13	HcKCR1	bic
E	46	F	type 2	9E	57	HcKCR1	0-mg +/- KA
F	52	F	type 1	10F	351	HcKCR1	0-mg +/- KA
G	35	M	No HS	11G	55	HcKCR1	0-mg +/- KA
				12G	17	HcKCR1	0-mg +/- KA

Table E.1: **Patient and characteristics of patients undergoing anterior temporal lobectomy for refractory temporal lobe epilepsy, from whom hippocampal samples were obtained.** PT ID is a patient designated letter for identifying which slices are from which patient. Age in years and sex (M=male, F=female) are also shown. Hippocampal sclerosis is designated on a binary scale, where y = pathologically confirmed hippocampal sclerosis and n = no pathologically confirmed hippocampal sclerosis. Slice ID uses the letter PT ID designation combined with a numerical identifier of separate slices. A different number with the same paired letter in Slice ID designates that a slice was derived from the same patient. Units refers to the maximum number of individual units recorded during experimental recordings after spike sorting and curation. Opsin designates whether HcKCR1 or ChR2 was the channelrhodopsin transduced, n/a = no channelrhodopsin transduced. Perturbations refers changes to recording media used in experiments with the designated slice. bic = bicuculline, 0-mg +/- KA = zero magnesium media with and without addition of kainic acid. *HS = hippocampal Sclerosis †ILAE HS = International League Against Epilepsy classification of hippocampal sclerosis

Slice ID	Transduction %	≥ 25% FR Decrease	≥ 50% FR Decrease	≥ 75% FR Decrease	≥ 90% FR Decrease
3C	45	83%	81%	70%	65%
5C	36	96%	93%	86%	72%
7D	12	82%	66%	49%	36%
8D	19	100%	100%	100%	100%
9E	24	56%	51%	44%	40%
10F	54	39%	23%	13%	8%
11G	22	47%	39%	28%	15%
12G	10	46%	46%	44%	40%

Table E.2: Transduction %: Percent of NeuN-expressing neurons co-expressing HcKCR1-eYFP in immunohistochemistry where transduction rates are calculated in areas approximating the area of slice over the recording array. %FR decrease where each column represents the % of recorded neurons whose firing rate was reduced by greater-than or equal-to 25, 50, 75, and 90% compared to the 10s mean firing rate before Light-ON conditions shown in Figure 6.3, E.1, E.2, E.3. The value in each column is the percentage of recorded units with a % decrease by greater-than or equal-to the threshold designated by the column header. FR = firing rate.

Cluster	odds_ratio	CI_lower	CI_upper	p.adjusted
Cluster 1	0.164	0.113	0.236	1.851e-21
Cluster 2	0.005	0.001	0.021	7.376e-13
Cluster 3	0.085	0.057	0.127	3.005e-33
Cluster 4	0.431	0.296	0.629	1.863e-05
Cluster 5*	**10.235**	**5.810**	**18.030**	**2.658e-15**
Cluster 6*	**8.294**	**4.386**	**15.685**	**1.238e-10**
Cluster 7	1.129	0.773	1.651	0.53
Cluster 8*	**8.395**	**4.614**	**15.273**	**5.951e-12**
Cluster 9*	**2.317**	**1.537**	**3.493**	**7.781e-05**
Cluster 10*	**2.327**	**1.471**	**3.682**	**3.634e-04**
Cluster 11	0.028	0.014	0.055	3.893e-23
Cluster 12	0.736	0.516	1.050	0.099

Table E.3: **Cluster association with GCL of the dentate gyrus.** *Positive associations with GCL localization

Figure E.1: **Optogenetic inhibition in physiologic and bicuculline media.** **(a)** Hippocampal slice 3C expressing HcKCR1, illuminated with 10s of continuous 530nm LED light. On the y-axis are 5 trials (t1 – t5) of continuous 10s illumination, stacked to line up the phase immediately preceding illumination (pre), during illumination (light-ON) in green, and the 10s following the end of illumination (OFF). The average firing rate of all units overlaid (red) demonstrates the drop in firing rate during illumination. **(b)** Average firing rate (Hz) of all recorded units in slice 3C during the 10 seconds prior to illumination (Pre), during illumination (light-ON), and following illumination (OFF). The unit firing rates from the 10s periods were significantly different between of Pre vs light-ON (P= 3.682866e-49), light-ON vs OFF (P= 1.996102e-19) and pre vs light-OFF (P= 4.833599e-12) in this slice (Wilcoxon signed-rank test and P-values adjusted by Bonferroni correction). **(c)** Average spike amplitude (µV) of all recorded units in slice 3C showing no significant difference among the 3 conditions. **(d-f)** Same parameters as shown in a-c, are shown for slice 5C, recorded with bicuculline. **(g-i)** same parameters for slice 7D and **(j-l)** for slice 8D.

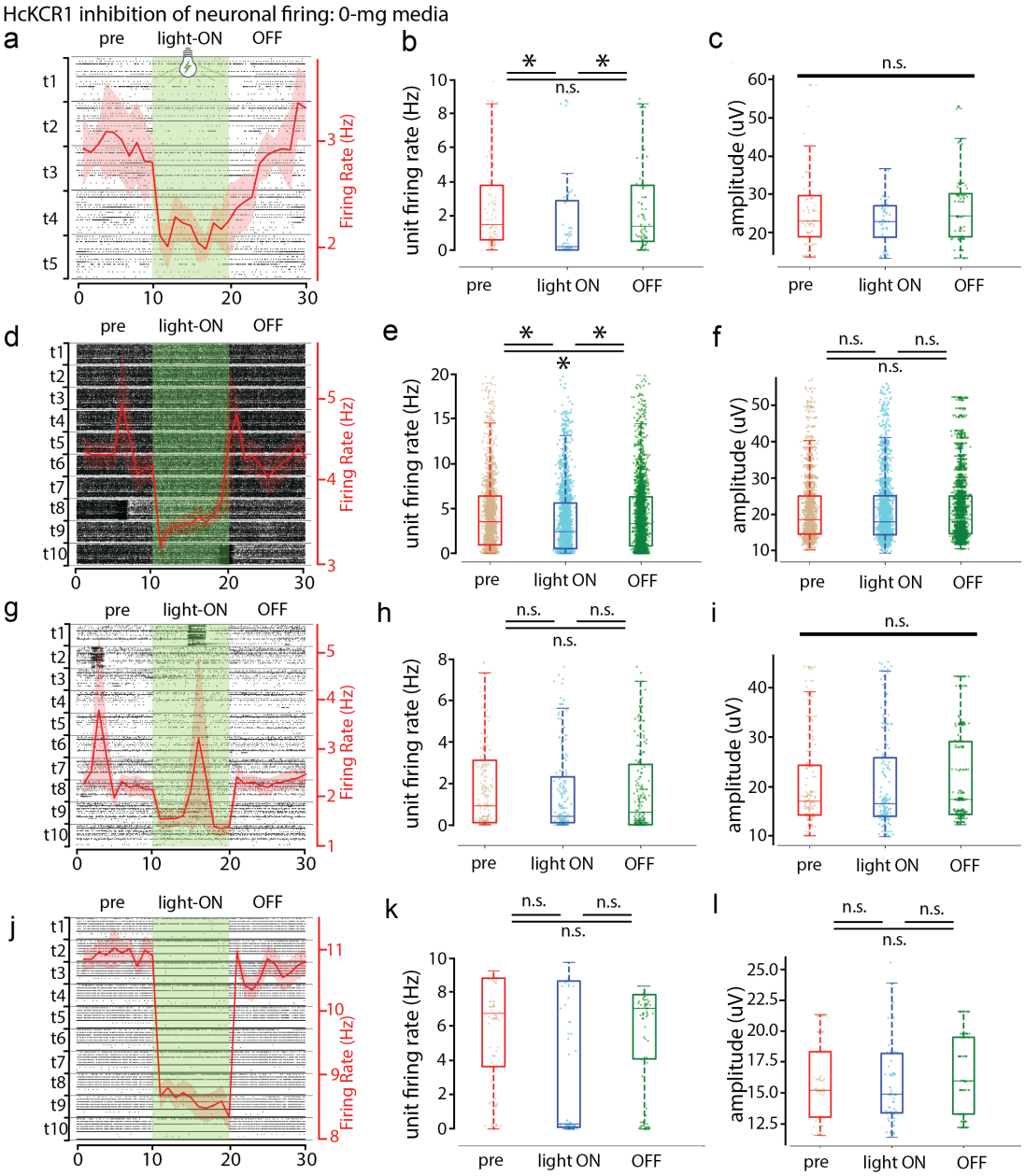

Figure E.2: **Optogenetic inhibition in media without magnesium.** Same parameters as described for Figure E.1, for 4 slices recorded under 0-mg conditions.

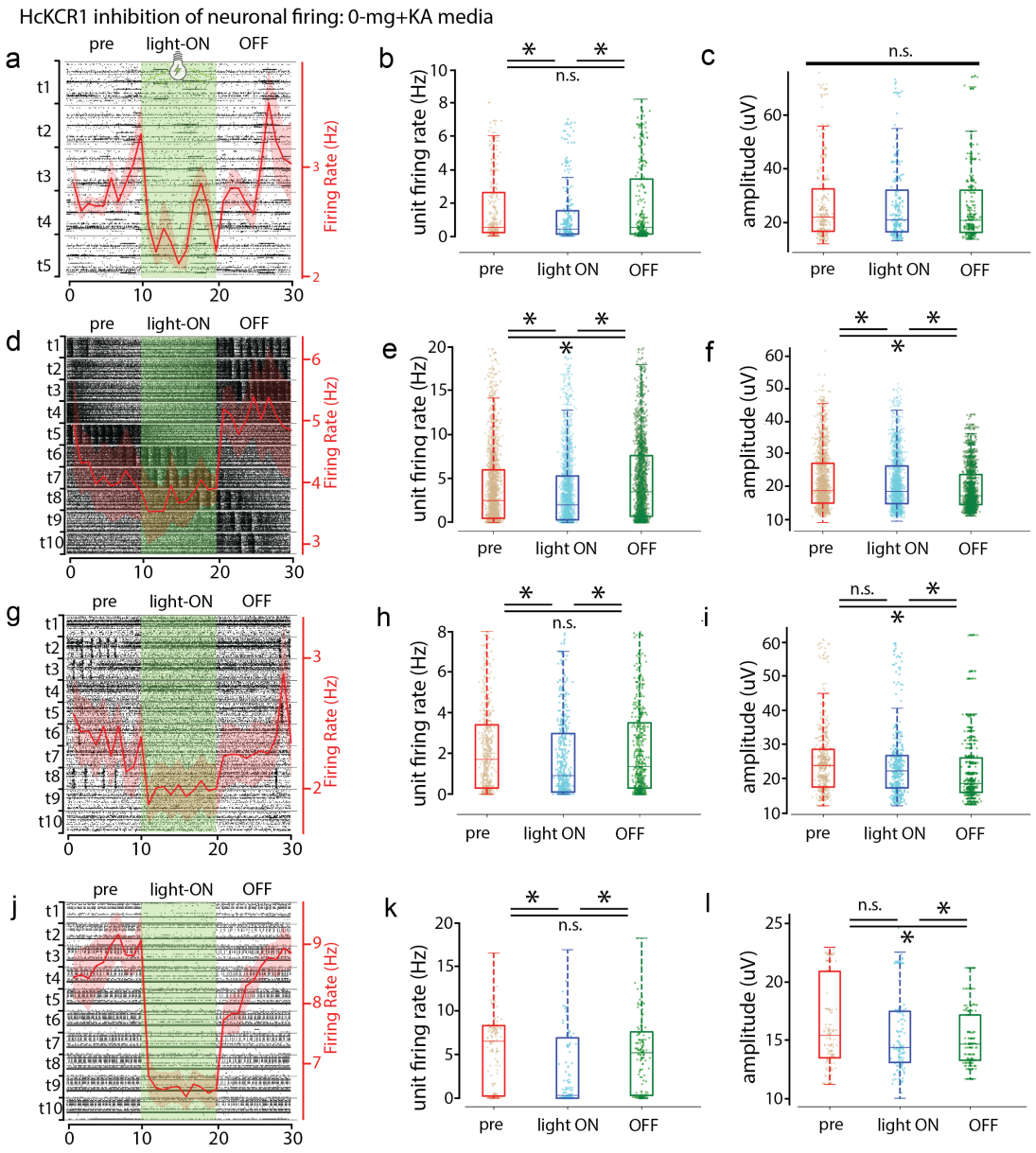

Figure E.3: **Optogenetic inhibition in media without magnesium with kainic acid.** Same parameters as described for Figure E.1 and E.2, for 4 slices recorded under 0-mg+KA conditions.

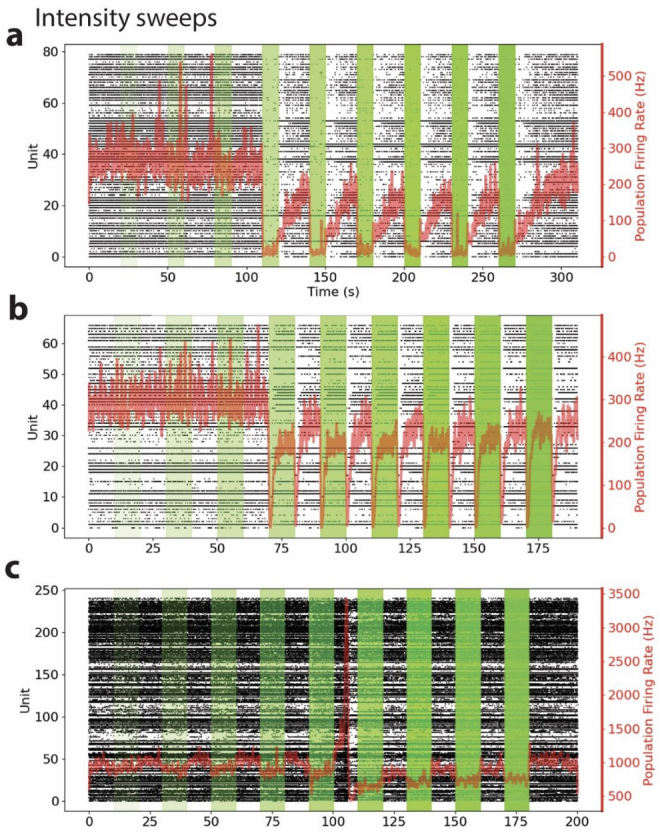

Figure E.4: **Optogenetic intensity sweep.** Unit activity with firing rate overlaid during the activity sweep for 3 separate slices. **(a & b)** Intensity sweep of 2 slices (a = slice 3C, b = slice 5C) recorded in physiologic media. **(c)** Intensity sweep of a slice (c = slice 10F) recorded in 0-mg media.

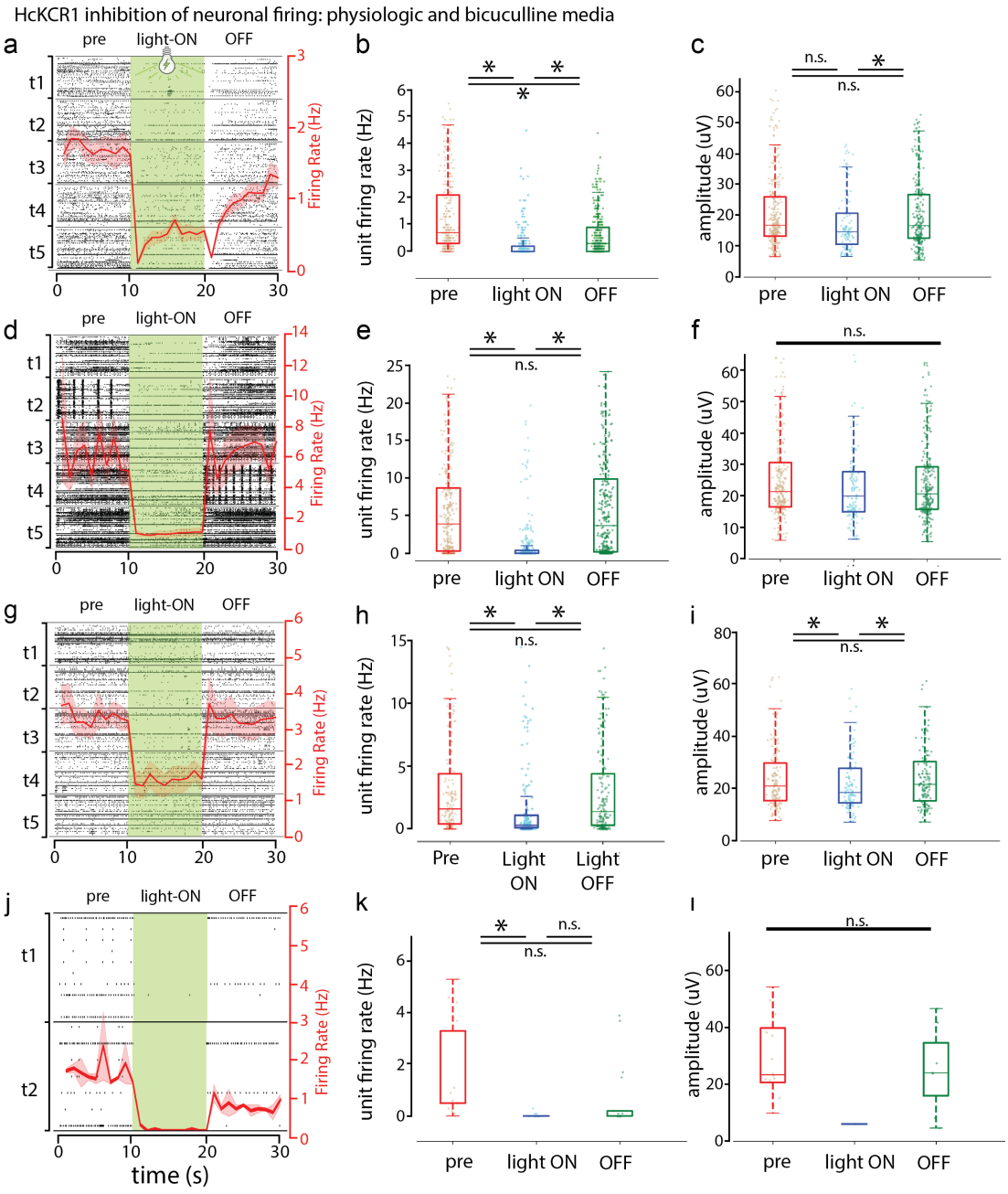
HcKCR1 inhibition of neuronal firing: physiologic and bicuculline media
a
pre
light-ON
OFF
t1
t2
t3
t4
t5
Firing Rate (Hz)
b
unit firing rate (Hz)
pre
light ON
OFF
c
amplitude (uV)
n.s.
d
e
f
g
h
Pre
Light ON
Light OFF
i
j
time (s)
k
l

Bibliography

[1] Saadullah Farooq Abbasi, Mohammad Awais, Xian Zhao, and Wei Chen. Automatic denoising and artifact removal from neonatal EEG. In *BIBE 2019; The Third International Conference on Biological Information and Biomedical Engineering*, pages 1–5, June 2019.

[2] Taiga Abe, Ian Kinsella, Shreya Saxena, Liam Paninski, and John P Cunningham. Neuroscience Cloud Analysis As a Service. page 32.

[3] Ahsan Adeel, Mandar Gogate, Saadullah Farooq, Cosimo Ieracitano, Kia Dashtipour, Hadi Larijani, and Amir Hussain. A Survey on the Role of Wireless Sensor Networks and IoT in Disaster Management. pages 57–66. 2019. arXiv:1909.10353 [cs].

[4] Misha B. Ahrens, Michael B. Orger, Drew N. Robson, Jennifer M. Li, and Philipp J. Keller. Whole-brain functional imaging at cellular resolution using light-sheet microscopy. *Nature Methods*, 10(5):413–420, May 2013. Publisher: Nature Publishing Group.

[5] Matthieu Ambroise, Stefano Buccelli, Filippo Grassia, Antoine Pirog, Yannick Bornat, Michela Chiappalone, and Timothée Levi. Biomimetic neural network for modifying biological dynamics during hybrid experiments. *Artificial Life and Robotics*, 22(3):398–403, September 2017.

[6] Peter Amstutz, Michael R. Crusoe, Nebojša Tijanić, Brad Chapman, John Chilton, Michael Heuer, Andrey Kartashov, Dan Leehr, Hervé Ménager, Maya Nedeljkovich, Matt Scales, Stian Soiland-Reyes, and Luka Stojanovic. Common Workflow Language, v1.0. July 2016. Publisher: figshare.

[7] Jimena Andersen, Omer Revah, Yuki Miura, Nicholas Thom, Neal D. Amin, Kevin W. Kelley, Mandeep Singh, Xiaoyu Chen, Mayuri Vijay Thete, Elisabeth M. Walczak, Hannes Vogel, H. Christina Fan, and Sergiu P. Paşca. Generation of Functional Human 3D Cortico-Motor Assembloids. *Cell*, 183(7):1913–1929.e26, December 2020.

[8] My Andersson, Natalia Avaliani, Andreas Svensson, Jenny Wickham, Lars H. Pinborg, Bo Jespersen, Søren H. Christiansen, Johan Bengzon, David P. D. Woldbye, and Merab Kokaia. Optogenetic control of human neurons in organotypic brain cultures. *Scientific Reports*, 6(1):24818, April 2016. Publisher: Nature Publishing Group.

[9] M. Avoli, C. Drapeau, J. Louvel, R. Pumain, A. Olivier, and J. G. Villemure. Epileptiform activity induced by low extracellular magnesium in the human cortex maintained in vitro. *Annals of Neurology*, 30(4):589–596, October 1991.

[10] Fatma Ayhan, Ashwinikumar Kulkarni, Stefano Berto, Karthigayini Sivaprakasam, Connor Douglas, Bradley C. Lega, and Genevieve Konopka. Resolving cellular and molecular diversity along the hippocampal anterior-to-posterior axis in humans. *Neuron*, 109(13):2091–2105.e6, July 2021.

[11] Frederico A.C. Azevedo, Ludmila R.B. Carvalho, Lea T. Grinberg, José Marcelo Farfel, Renata E.L. Ferretti, Renata E.P. Leite, Wilson Jacob Filho, Roberto Lent, and Suzana Herculano-Houzel. Equal numbers of neuronal and nonneuronal cells make the human brain an isometrically scaled-up primate brain. *The Journal of Comparative Neurology*, 513(5):532–541, April 2009.

[12] Brendon M. Baker and Christopher S. Chen. Deconstructing the third dimension: how 3D culture microenvironments alter cellular cues. *Journal of Cell Science*, 125(Pt 13):3015–3024, July 2012.

[13] Douglas J. Bakkum, Milos Radivojevic, Urs Frey, Felix Franke, Andreas Hierlemann, and Hirokazu Takahashi. Parameters for burst detection. *Frontiers in Computational Neuroscience*, 7, 2014. Publisher: Frontiers.

[14] Marco Ballini, Jan Müller, Paolo Livi, Yihui Chen, Urs Frey, Alexander Stettler, Amir Shadmani, Vijay Viswam, Ian Lloyd Jones, David Jäckel, Milos Radivojevic, Marta K. Lewandowska, Wei Gong, Michele Fiscella, Douglas J. Bakkum, Flavio Heer, and Andreas Hierlemann. A 1024-Channel CMOS Microelectrode Array With 26,400 Electrodes for Recording and Stimulation of Electrogenic Cells In Vitro. *IEEE Journal of Solid-State Circuits*, 49(11):2705–2719, November 2014. Conference Name: IEEE Journal of Solid-State Circuits.

[15] Pouya Bashivan, Kohitij Kar, and James J. DiCarlo. Neural population control via deep image synthesis. *Science*, 364(6439), May 2019.

[16] Danielle S. Bassett and Edward T. Bullmore. Small-World Brain Networks Revisited. *The Neuroscientist*, 23(5):499–516, October 2017. Publisher: SAGE Publications Inc STM.

[17] Maxwell Bates, Aaron J. Berliner, Joe Lachoff, Paul R. Jaschke, and Eli S. Groban. Wet Lab Accelerator: A Web-Based Application Democratizing Laboratory Automation for Synthetic Biology. *ACS Synthetic Biology*, 6(1):167–171, January 2017. Publisher: American Chemical Society.

[18] Pierre V. Baudin, Victoria T. Ly, Pattawong Pansodtee, Erik A. Jung, Robert Currie, Ryan Hoffman, Helen Rankin Willsey, Alex A. Pollen, Tomasz J. Nowakowski, David Haussler, Mohammed A. Mostajo-Radji, Sofie R. Salama, and Mircea Teodorescu. Low cost cloud based remote microscopy for biological sciences. *Internet of Things*, page 100454, September 2021.

[19] John M. Beggs and Dietmar Plenz. Neuronal Avalanches in Neocortical Circuits. *Journal of Neuroscience*, 23(35):11167–11177, December 2003. Publisher: Society for Neuroscience Section: Behavioral/Systems/Cognitive.

[20] Hugo J. Bellen, Chao Tong, and Hiroshi Tsuda. 100 years of Drosophila research and its impact on vertebrate neuroscience: a history lesson for the future. *Nature Reviews Neuroscience*, 11(7):514–522, July 2010. Number: 7 Publisher: Nature Publishing Group.

[21] Marie Bernert and Blaise Yvert. Fully unsupervised online spike sorting based on an artificial spiking neural network. *bioRxiv*, page 236224, December 2017. Publisher: Cold Spring Harbor Laboratory Section: New Results.

[22] Marie Bernert and Blaise Yvert. An Attention-Based Spiking Neural Network for Unsupervised Spike-Sorting. *International Journal of Neural Systems*, 29(08):1850059, December 2018. Publisher: World Scientific Publishing Co.

[23] Ivan Bertoncello. Optimizing the Cell Culture Microenvironment. In Ivan Bertoncello, editor, *Mouse Cell Culture: Methods and Protocols*, Methods in Molecular Biology, pages 23–30. Springer, New York, NY, 2019.

[24] G. Q. Bi and M. M. Poo. Synaptic modifications in cultured hippocampal neurons: dependence on spike timing, synaptic strength, and postsynaptic cell type. *The Journal of Neuroscience: The Official Journal of the Society for Neuroscience*, 18(24):10464–10472, December 1998.

[25] Anna Birgersdotter, Rickard Sandberg, and Ingemar Ernberg. Gene expression perturbation in vitro—A growing case for three-dimensional (3D) culture systems. *Seminars in Cancer Biology*, 15(5):405–412, October 2005.

[26] Ingmar Blümcke, Maria Thom, Eleonora Aronica, Dawna D. Armstrong, Fabrice Bartolomei, Andrea Bernasconi, Neda Bernasconi, Christian G. Bien, Fernando Cendes, Roland Coras, J. Helen Cross, Thomas S. Jacques, Philippe Kahane, Gary W. Mathern, Haijme Miyata, Solomon L. Moshé, Buge Oz, Çiğdem Özkara, Emilio Perucca, Sanjay Sisodiya, Samuel Wiebe, and Roberto Spreafico. International consensus classification of hippocampal sclerosis in temporal lobe epilepsy: A Task Force report from the ILAE Commission on Diagnostic Methods. *Epilepsia*, 54(7):1315–1329, 2013. _eprint: https://onlinelibrary.wiley.com/doi/pdf/10.1111/epi.12220.

[27] György Buzsáki, Costas A. Anastassiou, and Christof Koch. The origin of extracellular fields and currents — EEG, ECoG, LFP and spikes. *Nature Reviews Neuroscience*, 13(6):407–420, June 2012. Number: 6 Publisher: Nature Publishing Group.

[28] Cathryn R. Cadwell, Athanasia Palasantza, Xiaolong Jiang, Philipp Berens, Qiaolin Deng, Marlene Yilmaz, Jacob Reimer, Shan Shen, Matthias Bethge, Kimberley F. Tolias, Rickard Sandberg, and Andreas S. Tolias. Electrophysiological, transcriptomic and morphologic profiling of single neurons using Patch-seq. *Nature Biotechnology*, 34(2):199–203, February 2016. Publisher: Nature Publishing Group.

[29] D. J. Caldwell, J. A. Cronin, R. P. N. Rao, K. L. Collins, K. E. Weaver, A. L. Ko, J. G. Ojemann, J. N. Kutz, and B. W. Brunton. Signal recovery from stimulation artifacts in intracranial recordings with dictionary learning. *Journal of Neural Engineering*, 17(2):026023, April 2020. Publisher: IOP Publishing.

[30] Christophe Cariou, Laure Moiroux-Arvis, François Pinet, and Jean-Pierre Chanet. Internet of Underground Things in Agriculture 4.0: Challenges, Applications and Perspectives. *Sensors*, 23(8):4058, January 2023. Number: 8 Publisher: Multidisciplinary Digital Publishing Institute.

[31] Tansu Celikel, Vanessa A. Szostak, and Daniel E. Feldman. Modulation of spike timing by sensory deprivation during induction of cortical map plasticity. *Nature Neuroscience*, 7(5):534–541, May 2004.

[32] M. Chalfie, J. E. Sulston, J. G. White, E. Southgate, J. N. Thomson, and S. Brenner. The neural circuit for touch sensitivity in Caenorhabditis ele-

gans. *Journal of Neuroscience*, 5(4):956–964, April 1985. Publisher: Society for Neuroscience Section: Articles.

[33] Rosemary C. Challis, Sripriya Ravindra Kumar, Ken Y. Chan, Collin Challis, Keith Beadle, Min J. Jang, Hyun Min Kim, Pradeep S. Rajendran, John D. Tompkins, Kalyanam Shivkumar, Benjamin E. Deverman, and Viviana Gradinaru. Systemic AAV vectors for widespread and targeted gene delivery in rodents. *Nature Protocols*, 14(2):379–414, February 2019.

[34] Zenas C. Chao, Douglas J. Bakkum, and Steve M. Potter. Shaping Embodied Neural Networks for Adaptive Goal-directed Behavior. *PLOS Computational Biology*, 4(3):e1000042, March 2008. Publisher: Public Library of Science.

[35] Tsai-Wen Chen, Trevor J. Wardill, Yi Sun, Stefan R. Pulver, Sabine L. Renninger, Amy Baohan, Eric R. Schreiter, Rex A. Kerr, Michael B. Orger, Vivek Jayaraman, Loren L. Looger, Karel Svoboda, and Douglas S. Kim. Ultrasensitive fluorescent proteins for imaging neuronal activity. *Nature*, 499(7458):295–300, July 2013. Publisher: Nature Publishing Group.

[36] Yu Chen, Robert H. Austin, and James C. Sturm. On-chip cell labelling and washing by capture and release using microfluidic trap arrays. *Biomicrofluidics*, 11(5):054107, September 2017.

[37] Zhe Chen, Garrett J. Blair, Chengdi Cao, Jim Zhou, Daniel Aharoni, Peyman Golshani, Hugh T. Blair, and Jason Cong. FPGA-Based In-Vivo Calcium Image Decoding for Closed-Loop Feedback Applications. *IEEE Transactions on Biomedical Circuits and Systems*, 17(2):169–179, April 2023. Conference Name: IEEE Transactions on Biomedical Circuits and Systems.

[38] Miguel R. Chuapoco, Nicholas C. Flytzanis, Nick Goeden, J. Christopher Octeau, Kristina M. Roxas, Ken Y. Chan, Jon Scherrer, Janet Winchester, Roy J. Blackburn, Lillian J. Campos, Kwun Nok Mimi Man, Junqing Sun, Xinhong Chen, Arthur Lefevre, Vikram Pal Singh, Cynthia M. Arokiaraj, Timothy F. Shay, Julia Vendemiatti, Min J. Jang, John K. Mich, Yemeserach Bishaw, Bryan B. Gore, Victoria Omstead, Naz Taskin, Natalie Weed, Boaz P. Levi, Jonathan T. Ting, Cory T. Miller, Benjamin E. Deverman, James Pickel, Lin Tian, Andrew S. Fox, and Viviana Gradinaru. Adeno-associated viral vectors for functional intravenous gene transfer throughout the non-human primate brain. *Nature Nanotechnology*, 18(10):1241–1251, October 2023. Publisher: Nature Publishing Group.

[39] Jason E. Chung, Jeremy F. Magland, Alex H. Barnett, Vanessa M. Tolosa, Angela C. Tooker, Kye Y. Lee, Kedar G. Shah, Sarah H. Felix, Loren M. Frank, and Leslie F. Greengard. A Fully Automated Approach to Spike Sorting. *Neuron*, 95(6):1381–1394.e6, September 2017.

[40] Ivan Cohen, Vincent Navarro, Stéphane Clemenceau, Michel Baulac, and Richard Miles. On the origin of interictal activity in human temporal lobe epilepsy in vitro. *Science (New York, N.Y.)*, 298(5597):1418–1421, November 2002.

[41] Steven J. Cook, Travis A. Jarrell, Christopher A. Brittin, Yi Wang, Adam E. Bloniarz, Maksim A. Yakovlev, Ken C. Q. Nguyen, Leo T.-H. Tang, Emily A. Bayer, Janet S. Duerr, Hannes E. Bülow, Oliver Hobert, David H. Hall, and Scott W. Emmons. Whole-animal connectomes of both Caenorhabditis elegans sexes. *Nature*, 571(7763):63–71, July 2019. Number: 7763 Publisher: Nature Publishing Group.

[42] D. Kacy Cullen, Wisberty J. Gordián-Vélez, Laura A. Struzyna, Dennis Jgamadze, James Lim, Kathryn L. Wofford, Kevin D. Browne, and H. Isaac Chen. Bundled Three-Dimensional Human Axon Tracts Derived from Brain Organoids. *iScience*, 21:57–67, November 2019.

[43] Karl Deisseroth. Optogenetics. *Nature Methods*, 8(1):26–29, January 2011. Number: 1 Publisher: Nature Publishing Group.

[44] THOMAS B. DeMARSE, DANIEL A. WAGENAAR, AXEL W. BLAU, and STEVE M. POTTER. The Neurally Controlled Animat: Biological Brains Acting with Simulated Bodies. *Autonomous robots*, 11(3):305–310, 2001.

[45] Jiyeon K. Denninger, Xi Chen, Altan M. Turkoglu, Patricia Sarchet, Abby R. Volk, Joshua D. Rieskamp, Pearlly Yan, and Elizabeth D. Kirby. Defining the adult hippocampal neural stem cell secretome: In vivo versus in vitro transcriptomic differences and their correlation to secreted protein levels. *Brain Research*, 1735:146717, May 2020.

[46] Benjamin E. Deverman, Piers L. Pravdo, Bryan P. Simpson, Sripriya Ravindra Kumar, Ken Y. Chan, Abhik Banerjee, Wei-Li Wu, Bin Yang, Nina Huber, Sergiu P. Pasca, and Viviana Gradinaru. Cre-dependent selection yields AAV variants for widespread gene transfer to the adult brain. *Nature Biotechnology*, 34(2):204–209, February 2016. Publisher: Nature Publishing Group.

[47] Ashesh K Dhawale, Rajesh Poddar, Steffen BE Wolff, Valentin A Normand, Evi Kopelowitz, and Bence P Ölveczky. Automated long-term recording and analysis of neural activity in behaving animals. *eLife*, 6:e27702, September 2017. Publisher: eLife Sciences Publications, Ltd.

[48] Paolo Di Tommaso, Maria Chatzou, Evan W. Floden, Pablo Prieto Barja, Emilio Palumbo, and Cedric Notredame. Nextflow enables reproducible computational workflows. *Nature Biotechnology*, 35(4):316–319, April 2017. Number: 4 Publisher: Nature Publishing Group.

[49] Jordane Dimidschstein, Qian Chen, Robin Tremblay, Stephanie L. Rogers, Giuseppe-Antonio Saldi, Lihua Guo, Qing Xu, Runpeng Liu, Congyi Lu, Jianhua Chu, Joshua S. Grimley, Anne-Rachel Krostag, Ajamete Kaykas, Michael C. Avery, Mohammad S. Rashid, Myungin Baek, Amanda L. Jacob, Gordon B. Smith, Daniel E. Wilson, Georg Kosche, Illya Kruglikov, Tomasz Rusielewicz, Vibhakar C. Kotak, Todd M. Mowery, Stewart A. Anderson, Edward M. Callaway, Jeremy S. Dasen, David Fitzpatrick, Valentina Fossati, Michael A. Long, Scott Noggle, John H. Reynolds, Dan H. Sanes, Bernardo Rudy, Guoping Feng, and Gord Fishell. A viral strategy for targeting and manipulating interneurons across vertebrate species. *Nature Neuroscience*, 19(12):1743–1749, December 2016. Publisher: Nature Publishing Group.

[50] J. Dragas, V. Viswam, A. Shadmani, Y. Chen, R. Bounik, A. Stettler, M. Radivojevic, S. Geissler, M. E. J. Obien, J. Müller, and A. Hierlemann. In VitroMulti-Functional Microelectrode Array Featuring 59 760 Electrodes, 2048 Electrophysiology Channels, Stimulation, Impedance Measurement, and Neurotransmitter Detection Channels. *IEEE Journal of Solid-State Circuits*, 52(6):1576–1590, June 2017.

[51] John Carew Eccles. *The Physiology of Synapses*. Springer, Berlin, Heidelberg, 1964.

[52] Mototsugu Eiraku, Kiichi Watanabe, Mami Matsuo-Takasaki, Masako Kawada, Shigenobu Yonemura, Michiru Matsumura, Takafumi Wataya, Ayaka Nishiyama, Keiko Muguruma, and Yoshiki Sasai. Self-Organized Formation of Polarized Cortical Tissues from ESCs and Its Active Manipulation by Extrinsic Signals. *Cell Stem Cell*, 3(5):519–532, November 2008. Publisher: Elsevier.

[53] Matthew A. T. Elliott, Hunter E. Schweiger, Ash Robbins, Samira Vera-Choqqueccota, Drew Ehrlich, Sebastian Hernandez, Kateryna Voitiuk, Jinghui Geng, Jess L. Sevetson, Cordero Core, Yohei M. Rosen, Mircea

Teodorescu, Nico O. Wagner, David Haussler, and Mohammed A. Mostajo-Radji. Internet-Connected Cortical Organoids for Project-Based Stem Cell and Neuroscience Education. *eNeuro*, 10(12), December 2023. Publisher: Society for Neuroscience Section: Research Article: New Research.

[54] Jonathan C. Erickson, James A. Hayes, Mauricio Bustamante, Rajwol Joshi, Alfred Rwagaju, Niranchan Paskaranandavadivel, and Timothy R. Angeli. Intsy: a low-cost, open-source, wireless multi-channel bioamplifier system. *Physiological Measurement*, 39(3):035008, March 2018. Publisher: IOP Publishing.

[55] Summer R. Fair, Dominic Julian, Annalisa M. Hartlaub, Sai Teja Pusuluri, Girik Malik, Taryn L. Summerfied, Guomao Zhao, Arelis B. Hester, William E. Ackerman, Ethan W. Hollingsworth, Mehboob Ali, Craig A. McElroy, Irina A. Buhimschi, Jaime Imitola, Nathalie L. Maitre, Tracy A. Bedrosian, and Mark E. Hester. Electrophysiological Maturation of Cerebral Organoids Correlates with Dynamic Morphological and Cellular Development. *Stem Cell Reports*, 15(4):855–868, October 2020.

[56] Bahar Farahani, Farshad Firouzi, Victor Chang, Mustafa Badaroglu, Nicholas Constant, and Kunal Mankodiya. Towards fog-driven IoT eHealth: Promises and challenges of IoT in medicine and healthcare. *Future Generation Computer Systems*, 78:659–676, January 2018.

[57] Daniel E. Feldman. The spike timing dependence of plasticity. *Neuron*, 75(4):556–571, August 2012.

[58] D. J. Felleman and D. C. Van Essen. Distributed hierarchical processing in the primate cerebral cortex. *Cerebral Cortex (New York, N.Y.: 1991)*, 1(1):1–47, February 1991.

[59] Lief Fenno, Ofer Yizhar, and Karl Deisseroth. The Development and Application of Optogenetics. *Annual Review of Neuroscience*, 34(1):389–412, 2011. _eprint: https://doi.org/10.1146/annurev-neuro-061010-113817.

[60] Othmane Friha, Mohamed Amine Ferrag, Lei Shu, Leandros Maglaras, and Xiaochan Wang. Internet of Things for the Future of Smart Agriculture: A Comprehensive Survey of Emerging Technologies. *IEEE/CAA Journal of Automatica Sinica*, 8(4):718–752, April 2021. Conference Name: IEEE/CAA Journal of Automatica Sinica.

[61] Min Fu, Xinzhu Yu, Ju Lu, and Yi Zuo. Repetitive motor learning induces coordinated formation of clustered dendritic spines in vivo. *Nature*, 483(7387):92–95, February 2012.

[62] Erich Gamma. *Design patterns : elements of reusable object-oriented software*. Reading, Mass. : Addison-Wesley, 1995.

[63] Leonardo D. Garma, Laura Matino, Giovanni Melle, Fabio Moia, Francesco De Angelis, Francesca Santoro, and Michele Dipalo. Cost-effective and multifunctional acquisition system for in vitro electrophysiological investigations with multi-electrode arrays. *PLOS ONE*, 14(3):e0214017, March 2019. Publisher: Public Library of Science.

[64] Stefano L. Giandomenico, Susanna B. Mierau, George M. Gibbons, Lea M. D. Wenger, Laura Masullo, Timothy Sit, Magdalena Sutcliffe, Jerome Boulanger, Marco Tripodi, Emmanuel Derivery, Ole Paulsen, András Lakatos, and Madeline A. Lancaster. Cerebral organoids at the air–liquid interface generate diverse nerve tracts with functional output. *Nature Neuroscience*, 22(4):669–679, April 2019.

[65] David Goertsen, Nicholas C. Flytzanis, Nick Goeden, Miguel R. Chuapoco, Alexander Cummins, Yijing Chen, Yingying Fan, Qiangge Zhang, Jitendra Sharma, Yangyang Duan, Liping Wang, Guoping Feng, Yu Chen, Nancy Y. Ip, James Pickel, and Viviana Gradinaru. AAV capsid variants with brain-wide transgene expression and decreased liver targeting after intravenous delivery in mouse and marmoset. *Nature Neuroscience*, 25(1):106–115, January 2022. Publisher: Nature Publishing Group.

[66] Cesar Gonzalez, Enrique Armijo, Javiera Bravo-Alegria, Andrea Becerra-Calixto, Charles E. Mays, and Claudio Soto. Modeling amyloid beta and tau pathology in human cerebral organoids. *Molecular Psychiatry*, 23(12):2363–2374, December 2018. Publisher: Nature Publishing Group.

[67] Elena G. Govorunova, Yueyang Gou, Oleg A. Sineshchekov, Hai Li, Xiaoyu Lu, Yumei Wang, Leonid S. Brown, François St-Pierre, Mingshan Xue, and John L. Spudich. Kalium channelrhodopsins are natural light-gated potassium channels that mediate optogenetic inhibition. *Nature Neuroscience*, 25(7):967–974, July 2022. Publisher: Nature Publishing Group.

[68] Viviana Gradinaru, Feng Zhang, Charu Ramakrishnan, Joanna Mattis, Rohit Prakash, Ilka Diester, Inbal Goshen, Kimberly R. Thompson, and Karl Deisseroth. Molecular and Cellular Approaches for Diversifying and Extending Optogenetics. *Cell*, 141(1):154–165, April 2010.

[69] Christine Grienberger and Arthur Konnerth. Imaging Calcium in Neurons. *Neuron*, 73(5):862–885, March 2012.

[70] Lukas Grossberger, Francesco P. Battaglia, and Martin Vinck. Unsupervised clustering of temporal patterns in high-dimensional neuronal ensembles using a novel dissimilarity measure. *PLOS Computational Biology*, 14(7):e1006283, July 2018. Publisher: Public Library of Science.

[71] Songtao Guo, Min Qiang, Xiaorui Luan, Pengfei Xu, Gang He, Xiaoyan Yin, Luo Xi, Xuelin Jin, Jianbin Shao, Xiaojiang Chen, Dingyi Fang, and Baoguo Li. The application of the Internet of Things to animal ecology. *Integrative Zoology*, 10(6):572–578, 2015. _eprint: https://onlinelibrary.wiley.com/doi/pdf/10.1111/1749-4877.12162.

[72] Mostafa Haghi, Kerstin Thurow, and Regina Stoll. Wearable Devices in Medical Internet of Things: Scientific Research and Commercially Available Devices. *Healthcare Informatics Research*, 23(1):4–15, January 2017.

[73] O. P. Hamill, A. Marty, E. Neher, B. Sakmann, and F. J. Sigworth. Improved patch-clamp techniques for high-resolution current recording from cells and cell-free membrane patches. *Pflügers Archiv*, 391(2):85–100, August 1981.

[74] D. Hansel, G. Mato, and C. Meunier. Synchrony in Excitatory Neural Networks. *Neural Computation*, 7(2):307–337, March 1995. Publisher: MIT Press.

[75] Reid R. Harrison, Paul T. Watkins, Ryan J. Kier, Robert O. Lovejoy, Daniel J. Black, Bradley Greger, and Florian Solzbacher. A Low-Power Integrated Circuit for a Wireless 100-Electrode Neural Recording System. *IEEE Journal of Solid-State Circuits*, 42(1):123–133, January 2007. Conference Name: IEEE Journal of Solid-State Circuits.

[76] M. Hassanalieragh, A. Page, T. Soyata, G. Sharma, M. Aktas, G. Mateos, B. Kantarci, and S. Andreescu. Health Monitoring and Management Using Internet-of-Things (IoT) Sensing with Cloud-Based Processing: Opportunities and Challenges. In *2015 IEEE International Conference on Services Computing*, pages 285–292, June 2015.

[77] Alan A. Helal, Rodolfo S. Villaça, Celso A. S. Santos, and Roberto Colistete. An integrated solution of software and hardware for environmental monitoring. *Internet of Things*, 19:100518, August 2022.

[78] Keith B. Hengen, Mary E. Lambo, Stephen D. Van Hooser, Donald B. Katz, and Gina G. Turrigiano. Firing Rate Homeostasis in Visual Cortex of Freely Behaving Rodents. *Neuron*, 80(2):335–342, October 2013.

[79] Keith B. Hengen, Alejandro Torrado Pacheco, James N. McGregor, Stephen D. Van Hooser, and Gina G. Turrigiano. Neuronal Firing Rate Homeostasis Is Inhibited by Sleep and Promoted by Wake. *Cell*, 165(1):180–191, March 2016.

[80] Darrell A. Henze, Zsolt Borhegyi, Jozsef Csicsvari, Akira Mamiya, Kenneth D. Harris, and György Buzsáki. Intracellular Features Predicted by Extracellular Recordings in the Hippocampus In Vivo. *Journal of Neurophysiology*, 84(1):390–400, July 2000. Publisher: American Physiological Society.

[81] Alexander M Herman, Longwen Huang, Dona K Murphey, Isabella Garcia, and Benjamin R Arenkiel. Cell type-specific and time-dependent light exposure contribute to silencing in neurons expressing Channelrhodopsin-2. *eLife*, 3:e01481, January 2014.

[82] J. Hermiz, N. Rogers, E. Kaestner, M. Ganji, D. Cleary, J. Snider, D. Barba, S. Dayeh, E. Halgren, and V. Gilja. A clinic compatible, open source electrophysiology system. In *2016 38th Annual International Conference of the IEEE Engineering in Medicine and Biology Society (EMBC)*, pages 4511–4514, August 2016. ISSN: 1558-4615.

[83] Daniel R. Hochbaum, Yongxin Zhao, Samouil L. Farhi, Nathan Klapoetke, Christopher A. Werley, Vikrant Kapoor, Peng Zou, Joel M. Kralj, Dougal Maclaurin, Niklas Smedemark-Margulies, Jessica L. Saulnier, Gabriella L. Boulting, Christoph Straub, Yong Ku Cho, Michael Melkonian, Gane Ka-Shu Wong, D. Jed Harrison, Venkatesh N. Murthy, Bernardo L. Sabatini, Edward S. Boyden, Robert E. Campbell, and Adam E. Cohen. All-optical electrophysiology in mammalian neurons using engineered microbial rhodopsins. *Nature Methods*, 11(8):825–833, August 2014. Publisher: Nature Publishing Group.

[84] A. L. Hodgkin and A. F. Huxley. Action Potentials Recorded from Inside a Nerve Fibre. *Nature*, 144(3651):710–711, October 1939. Publisher: Nature Publishing Group.

[85] A. L. Hodgkin and A. F. Huxley. A quantitative description of membrane current and its application to conduction and excitation in nerve. *The Journal of Physiology*, 117(4):500–544, 1952. _eprint: https://onlinelibrary.wiley.com/doi/pdf/10.1113/jphysiol.1952.sp004764.

[86] P.M. Horton, A.U. Nicol, K.M. Kendrick, and J.F. Feng. Spike sorting based upon machine learning algorithms (SOMA). *Journal of Neuroscience Methods*, 160(1):52–68, February 2007.

[87] Zahid Hossain, Engin Bumbacher, Alison Brauneis, Monica Diaz, Andy Saltarelli, Paulo Blikstein, and Ingmar H. Riedel-Kruse. Design Guidelines and Empirical Case Study for Scaling Authentic Inquiry-based Science Learning via Open Online Courses and Interactive Biology Cloud Labs. *International Journal of Artificial Intelligence in Education*, 28(4):478–507, December 2018.

[88] Zahid Hossain, Engin W. Bumbacher, Alice M. Chung, Honesty Kim, Casey Litton, Ashley D. Walter, Sachin N. Pradhan, Kemi Jona, Paulo Blikstein, and Ingmar H. Riedel-Kruse. Interactive and scalable biology cloud experimentation for scientific inquiry and education. *Nature Biotechnology*, 34(12):1293–1298, December 2016. Number: 12 Publisher: Nature Publishing Group.

[89] Danying Hu, Yuanzheng Gong, Eric J. Seibel, Laligam N. Sekhar, and Blake Hannaford. Semi-autonomous image-guided brain tumour resection using an integrated robotic system: A bench-top study. *The International Journal of Medical Robotics and Computer Assisted Surgery*, 14(1):e1872, 2018. _eprint: https://onlinelibrary.wiley.com/doi/pdf/10.1002/rcs.1872.

[90] Yu-Ting Huang, Yu-Lin Chang, Chun-Chung Chen, Pik-Yin Lai, and C. K. Chan. Positive feedback and synchronized bursts in neuronal cultures. *PLOS ONE*, 12(11):e0187276, November 2017. Publisher: Public Library of Science.

[91] Gilles Huberfeld, Liset Menendez de la Prida, Johan Pallud, Ivan Cohen, Michel Le Van Quyen, Claude Adam, Stéphane Clemenceau, Michel Baulac, and Richard Miles. Glutamatergic pre-ictal discharges emerge at the transition to seizure in human epilepsy. *Nature Neuroscience*, 14(5):627–634, May 2011. Publisher: Nature Publishing Group.

[92] A. F. Hussein, N. A. kumar, M. Burbano-Fernandez, G. Ramírez-González, E. Abdulhay, and V. H. C. De Albuquerque. An Automated Remote Cloud-Based Heart Rate Variability Monitoring System. *IEEE Access*, 6:77055–77064, 2018. Conference Name: IEEE Access.

[93] Muhammad Irfan, Husnain Jawad, Barkoum Betra Felix, Saadullah Farooq Abbasi, Anum Nawaz, Saeed Akbarzadeh, Muhammad Awais, Lin Chen, Tomi Westerlund, and Wei Chen. Non-Wearable IoT-Based

Smart Ambient Behavior Observation System. *IEEE Sensors Journal*, 21(18):20857–20869, September 2021. Conference Name: IEEE Sensors Journal.

[94] Shinya Ito and David A. Feldheim. The Mouse Superior Colliculus: An Emerging Model for Studying Circuit Formation and Function. *Frontiers in Neural Circuits*, 12, 2018. Publisher: Frontiers.

[95] L. L. Iversen. Role of Transmitter Uptake Mechanisms in Synaptic Neurotransmission. *British Journal of Pharmacology*, 41(4):571–591, 1971. _eprint: https://onlinelibrary.wiley.com/doi/pdf/10.1111/j.1476-5381.1971.tb07066.x.

[96] Andrew E. Jaffe, Daniel J. Hoeppner, Takeshi Saito, Lou Blanpain, Joy Ukaigwe, Emily E. Burke, Leonardo Collado-Torres, Ran Tao, Katsunori Tajinda, Kristen R. Maynard, Matthew N. Tran, Keri Martinowich, Amy Deep-Soboslay, Joo Heon Shin, Joel E. Kleinman, Daniel R. Weinberger, Mitsuyuki Matsumoto, and Thomas M. Hyde. Profiling gene expression in the human dentate gyrus granule cell layer reveals insights into schizophrenia and its genetic risk. *Nature Neuroscience*, 23(4):510–519, April 2020. Publisher: Nature Publishing Group.

[97] C.D. James, A.J.H. Spence, N.M. Dowell-Mesfin, R.J. Hussain, K.L. Smith, H.G. Craighead, M.S. Isaacson, W. Shain, and J.N. Turner. Extracellular recordings from patterned neuronal networks using planar microelectrode arrays. *IEEE Transactions on Biomedical Engineering*, 51(9):1640–1648, September 2004. Conference Name: IEEE Transactions on Biomedical Engineering.

[98] Eva M. Jimenez-Mateos, Tobias Engel, Paula Merino-Serrais, Ross C. McKiernan, Katsuhiro Tanaka, Genshin Mouri, Takanori Sano, Colm O'Tuathaigh, John L. Waddington, Suzanne Prenter, Norman Delanty, Michael A. Farrell, Donncha F. O'Brien, Ronán M. Conroy, Raymond L. Stallings, Javier DeFelipe, and David C. Henshall. Silencing microRNA-134 produces neuroprotective and prolonged seizure-suppressive effects. *Nature Medicine*, 18(7):1087–1094, July 2012.

[99] Lei Jin, Zhou Han, Jelena Platisa, Julian R. A. Wooltorton, Lawrence B. Cohen, and Vincent A. Pieribone. Single action potentials and subthreshold electrical events imaged in neurons with a fluorescent protein voltage probe. *Neuron*, 75(5):779–785, September 2012.

[100] Jolle W. Jolles. Broad-scale applications of the Raspberry Pi: A review and guide for biologists. *Methods in Ecology and Evolution*, 12(9):1562–1579, 2021. _eprint: https://onlinelibrary.wiley.com/doi/pdf/10.1111/2041-210X.13652.

[101] Roland S. G. Jones, Anderson Brito da Silva, Roger G. Whittaker, Gavin L. Woodhall, and Mark O. Cunningham. Human brain slices for epilepsy research: Pitfalls, solutions and future challenges. *Journal of Neuroscience Methods*, 260:221–232, February 2016.

[102] E R Kandel and L Tauc. Mechanism of heterosynaptic facilitation in the giant cell of the abdominal ganglion of Aplysia depilans. *The Journal of Physiology*, 181(1):28–47, November 1965.

[103] Eric R. Kandel, Henry Markram, Paul M. Matthews, Rafael Yuste, and Christof Koch. Neuroscience thinks big (and collaboratively). *Nature Reviews Neuroscience*, 14(9):659–664, September 2013. Number: 9 Publisher: Nature Publishing Group.

[104] Hiroshi Katsuki, Satoru Nakai, Yoshikatsu Hirai, Ken-ichi Akaji, Yoshiaki Kiso, and Masamichi Satoh. Interleukin-1 inhibits long-term potentiation in the CA3 region of mouse hippocampal slices. *European Journal of Pharmacology*, 181(3):323–326, June 1990.

[105] B. Katz and R. Miledi. The timing of calcium action during neuromuscular transmission. *The Journal of Physiology*, 189(3):535–544, 1967. _eprint: https://onlinelibrary.wiley.com/doi/pdf/10.1113/jphysiol.1967.sp008183.

[106] Corey J. Keller, Wilson Truccolo, John T. Gale, Emad Eskandar, Thomas Thesen, Chad Carlson, Orrin Devinsky, Ruben Kuzniecky, Werner K. Doyle, Joseph R. Madsen, Donald L. Schomer, Ashesh D. Mehta, Emery N. Brown, Leigh R. Hochberg, István Ulbert, Eric Halgren, and Sydney S. Cash. Heterogeneous neuronal firing patterns during interictal epileptiform discharges in the human cortex. *Brain*, 133(6):1668–1681, June 2010.

[107] Kevin W. Kelley and Sergiu P. Pașca. Human brain organogenesis: Toward a cellular understanding of development and disease. *Cell*, 185(1):42–61, January 2022.

[108] Jaimon T. Kelly, Katrina L. Campbell, Enying Gong, and Paul Scuffham. The Internet of Things: Impact and Implications for Health Care Delivery. *Journal of Medical Internet Research*, 22(11):e20135, November 2020. Company: Journal of Medical Internet Research Distributor: Journal of Medical

Internet Research Institution: Journal of Medical Internet Research Label: Journal of Medical Internet Research Publisher: JMIR Publications Inc., Toronto, Canada.

[109] Justin P. Kinney, Jacob G. Bernstein, Andrew J. Meyer, Jessica B. Barber, Marti Bolivar, Bryan Newbold, Jorg Scholvin, Caroline Moore-Kochlacs, Christian T. Wentz, Nancy J. Kopell, and Edward S. Boyden. A direct-to-drive neural data acquisition system. *Frontiers in Neural Circuits*, 9, 2015.

[110] Alexander Kirillov, Eric Mintun, Nikhila Ravi, Hanzi Mao, Chloe Rolland, Laura Gustafson, Tete Xiao, Spencer Whitehead, Alexander C. Berg, Wan-Yen Lo, Piotr Dollár, and Ross Girshick. Segment Anything, April 2023. arXiv:2304.02643 [cs].

[111] Nicola J. Knight, Samantha Kanza, Don Cruickshank, William S. Brocklesby, and Jeremy G. Frey. Talk2Lab: The Smart Lab of the Future. *IEEE Internet of Things Journal*, 7(9):8631–8640, September 2020. Conference Name: IEEE Internet of Things Journal.

[112] August Martinius Knudsen. NTNU Cyborg: A study into embodying Neuronal Cultures through Robotic Systems. *131*, 2016. Accepted: 2016-10-10T14:00:35Z Publisher: NTNU.

[113] Fanwei Kong, Liang Yuan, Yuan F. Zheng, and Weidong Chen. Automatic liquid handling for life science: a critical review of the current state of the art. *Journal of Laboratory Automation*, 17(3):169–185, June 2012.

[114] Satoshi Konishi, Takeshi Hashimoto, Tsubasa Nakabuchi, Takatoshi Ozeki, and Hiroki Kajita. Cell and tissue system capable of automated culture, stimulation, and monitor with the aim of feedback control of organs-on-a-chip. *Scientific Reports*, 11(1):2999, February 2021. Publisher: Nature Publishing Group.

[115] Esther Krook-Magnuson, Caren Armstrong, Anh Bui, Sean Lew, Mikko Oijala, and Ivan Soltesz. In vivo evaluation of the dentate gate theory in epilepsy. *The Journal of Physiology*, 593(10):2379–2388, May 2015.

[116] Esther Krook-Magnuson, Caren Armstrong, Mikko Oijala, and Ivan Soltesz. On-demand optogenetic control of spontaneous seizures in temporal lobe epilepsy. *Nature Communications*, 4(1):1376, January 2013. Publisher: Nature Publishing Group.

[117] R. Kumar and M. Pallikonda Rajasekaran. An IoT based patient monitoring system using raspberry Pi. In *2016 International Conference on Computing Technologies and Intelligent Data Engineering (ICCTIDE'16)*, pages 1–4, January 2016.

[118] DingleYu-Ting L, BoutinMolly E, ChirilaAnda M, LiviLiane L, LabriolaNicholas R, JakubekLorin M, MorganJeffrey R, DarlingEric M, KauerJulie A, and Hoffman-KimDiane. Three-Dimensional Neural Spheroid Culture: An In Vitro Model for Cortical Studies. *Tissue Engineering Part C: Methods*, October 2015. Publisher: Mary Ann Liebert, Inc. 140 Huguenot Street, 3rd Floor New Rochelle, NY 10801 USA.

[119] Yinzhi Lai, Ke Cheng, and William Kisaalita. Three Dimensional Neuronal Cell Cultures More Accurately Model Voltage Gated Calcium Channel Functionality in Freshly Dissected Nerve Tissue. *PLOS ONE*, 7(9):e45074, September 2012. Publisher: Public Library of Science.

[120] Madeline A. Lancaster, Magdalena Renner, Carol-Anne Martin, Daniel Wenzel, Louise S. Bicknell, Matthew E. Hurles, Tessa Homfray, Josef M. Penninger, Andrew P. Jackson, and Juergen A. Knoblich. Cerebral organoids model human brain development and microcephaly. *Nature*, 501(7467):373–379, September 2013. Number: 7467 Publisher: Nature Publishing Group.

[121] Lynn Le, Luca Ambrogioni, Katja Seeliger, Yağmur Güçlütürk, Marcel van Gerven, and Umut Güçlü. Brain2Pix: Fully convolutional naturalistic video reconstruction from brain activity. *bioRxiv*, page 2021.02.02.429430, February 2021. Publisher: Cold Spring Harbor Laboratory Section: New Results.

[122] Chang-Soo Lee. Grand Challenges in Microfluidics: A Call for Biological and Engineering Action. *Frontiers in Sensors*, 1, 2020.

[123] Eric Kenji Lee, Hymavathy Balasubramanian, Alexandra Tsolias, Stephanie Udochukwu Anakwe, Maria Medalla, Krishna V. Shenoy, and Chandramouli Chandrasekaran. Non-linear dimensionality reduction on extracellular waveforms reveals cell type diversity in premotor cortex, August 2021. Publisher: eLife Sciences Publications Limited.

[124] JinHyung Lee, Catalin Mitelut, Hooshmand Shokri, Ian Kinsella, Nishchal Dethe, Shenghao Wu, Kevin Li, Eduardo Blancas Reyes, Denis Turcu, Eleanor Batty, Young Joon Kim, Nora Brackbill, Alexandra Kling, Georges Goetz, E. J. Chichilnisky, David Carlson, and Liam Paninski. YASS: Yet Another Spike Sorter applied to large-scale multi-electrode array recordings in

primate retina. Technical report, March 2020. Company: Cold Spring Harbor Laboratory Distributor: Cold Spring Harbor Laboratory Label: Cold Spring Harbor Laboratory Section: New Results Type: article.

[125] Jung Min Lee, Guosong Hong, Dingchang Lin, Thomas G. Schuhmann, Andrew T. Sullivan, Robert D. Viveros, Hong-Gyu Park, and Charles M. Lieber. Nanoenabled Direct Contact Interfacing of Syringe-Injectable Mesh Electronics. *Nano Letters*, 19(8):5818–5826, August 2019.

[126] Kenji Lee, Nicole Carr, Alec Perliss, and Chandramouli Chandrasekaran. WaveMAP for identifying putative cell types from *in vivo* electrophysiology. *STAR Protocols*, 4(2):102320, June 2023.

[127] Suengwon Lee and Christian I. Hong. Organoids as Model Systems to Investigate Circadian Clock-Related Diseases and Treatments. *Frontiers in Genetics*, 13:874288, April 2022.

[128] M. S. Lewicki. A review of methods for spike sorting: the detection and classification of neural action potentials. *Network (Bristol, England)*, 9(4):R53–78, November 1998.

[129] Chong Li, Jonas Simon Fleck, Catarina Martins-Costa, Thomas R. Burkard, Jan Themann, Marlene Stuempflen, Angela Maria Peer, Ábel Vertesy, Jamie B. Littleboy, Christopher Esk, Ulrich Elling, Gregor Kasprian, Nina S. Corsini, Barbara Treutlein, and Juergen A. Knoblich. Single-cell brain organoid screening identifies developmental defects in autism. *Nature*, 621(7978):373–380, September 2023. Number: 7978 Publisher: Nature Publishing Group.

[130] Qiang Li, Kewang Nan, Paul Le Floch, Zuwan Lin, Hao Sheng, and Jia Liu. Cyborg Organoids: Implantation of Nanoelectronics via Organogenesis for Tissue-Wide Electrophysiology. *bioRxiv*, page 697664, July 2019. Publisher: Cold Spring Harbor Laboratory Section: New Results.

[131] Xiaoqing Li, Yu Lu, Xianghua Fu, and Yingjian Qi. Building the Internet of Things platform for smart maternal healthcare services with wearable devices and cloud computing. *Future Generation Computer Systems*, 118:282–296, May 2021.

[132] Xiaoguang Lu and Ye Ai. Automatic Microfluidic Cell Wash Platform for Purifying Cells in Suspension: Puriogen. *Analytical Chemistry*, 94(26):9424–9433, July 2022. Publisher: American Chemical Society.

[133] Liqun Luo, Edward M. Callaway, and Karel Svoboda. Genetic Dissection of Neural Circuits: A Decade of Progress. *Neuron*, 98(2):256–281, April 2018. Publisher: Elsevier.

[134] Victoria T. Ly, Pierre V. Baudin, Pattawong Pansodtee, Erik A. Jung, Kateryna Voitiuk, Yohei M. Rosen, Helen Rankin Willsey, Gary L. Mantalas, Spencer T. Seiler, John A. Selberg, Sergio A. Cordero, Jayden M. Ross, Marco Rolandi, Alex A. Pollen, Tomasz J. Nowakowski, David Haussler, Mohammed A. Mostajo-Radji, Sofie R. Salama, and Mircea Teodorescu. Picroscope: low-cost system for simultaneous longitudinal biological imaging. *Communications Biology*, 4(1):1–11, November 2021. Bandiera_abtest: a Cc_license_type: cc_by Cg_type: Nature Research Journals Number: 1 Primary_atype: Research Publisher: Nature Publishing Group Subject_term: Biological techniques;Developmental biology Subject_term_id: biological-techniques;developmental-biology.

[135] Maxime Lévesque and Massimo Avoli. The kainic acid model of temporal lobe epilepsy. *Neuroscience and Biobehavioral Reviews*, 37(10 Pt 2):2887–2899, December 2013.

[136] Zhengyu Ma, Gina G. Turrigiano, Ralf Wessel, and Keith B. Hengen. Cortical Circuit Dynamics Are Homeostatically Tuned to Criticality In Vivo. *Neuron*, September 2019.

[137] Niall P. Macdonald, Joan M. Cabot, Petr Smejkal, Rosanne M. Guijt, Brett Paull, and Michael C. Breadmore. Comparing Microfluidic Performance of Three-Dimensional (3D) Printing Platforms. *Analytical Chemistry*, 89(7):3858–3866, April 2017. Publisher: American Chemical Society.

[138] Jeremy Magland, James J Jun, Elizabeth Lovero, Alexander J Morley, Cole Lincoln Hurwitz, Alessio Paolo Buccino, Samuel Garcia, and Alex H Barnett. SpikeForest, reproducible web-facing ground-truth validation of automated neural spike sorters. *eLife*, 9:e55167, May 2020. Publisher: eLife Sciences Publications, Ltd.

[139] Nikolaus Maier, Volker Nimmrich, and Andreas Draguhn. Cellular and Network Mechanisms Underlying Spontaneous Sharp Wave–Ripple Complexes in Mouse Hippocampal Slices. *The Journal of Physiology*, 550(3):873–887, 2003. _eprint: https://physoc.onlinelibrary.wiley.com/doi/pdf/10.1113/jphysiol.2003.044602.

[140] Nikola T. Markov, Mária Ercsey-Ravasz, David C. Van Essen, Kenneth Knoblauch, Zoltán Toroczkai, and Henry Kennedy. Cortical High-Density

Counterstream Architectures. *Science*, 342(6158), November 2013. Publisher: American Association for the Advancement of Science Section: Review.

[141] Nikola T. Markov, Julien Vezoli, Pascal Chameau, Arnaud Falchier, René Quilodran, Cyril Huissoud, Camille Lamy, Pierre Misery, Pascale Giroud, Shimon Ullman, Pascal Barone, Colette Dehay, Kenneth Knoblauch, and Henry Kennedy. Anatomy of hierarchy: Feedforward and feedback pathways in macaque visual cortex. *Journal of Comparative Neurology*, 522(1):225–259, 2014. _eprint: https://onlinelibrary.wiley.com/doi/pdf/10.1002/cne.23458.

[142] H. Markram, J. Lübke, M. Frotscher, and B. Sakmann. Regulation of synaptic efficacy by coincidence of postsynaptic APs and EPSPs. *Science (New York, N.Y.)*, 275(5297):213–215, January 1997.

[143] Francis Kei Masuda, Emily A. Aery Jones, Yanjun Sun, and Lisa M. Giocomo. Ketamine evoked disruption of entorhinal and hippocampal spatial maps. *Nature Communications*, 14(1):6285, October 2023. Publisher: Nature Publishing Group.

[144] Leland McInnes and John Healy. Accelerated Hierarchical Density Clustering. In *2017 IEEE International Conference on Data Mining Workshops (ICDMW)*, pages 33–42, November 2017. arXiv:1705.07321 [stat].

[145] Miranda Mele, Ricardo Vieira, Bárbara Correia, Pasqualino De Luca, Filipe V. Duarte, Paulo S. Pinheiro, and Carlos B. Duarte. Transient incubation of cultured hippocampal neurons in the absence of magnesium induces rhythmic and synchronized epileptiform-like activity. *Scientific Reports*, 11(1):11374, May 2021. Publisher: Nature Publishing Group.

[146] John K. Mich, Lucas T. Graybuck, Erik E. Hess, Joseph T. Mahoney, Yoshiko Kojima, Yi Ding, Saroja Somasundaram, Jeremy A. Miller, Brian E. Kalmbach, Cristina Radaelli, Bryan B. Gore, Natalie Weed, Victoria Omstead, Yemeserach Bishaw, Nadiya V. Shapovalova, Refugio A. Martinez, Olivia Fong, Shenqin Yao, Marty Mortrud, Peter Chong, Luke Loftus, Darren Bertagnolli, Jeff Goldy, Tamara Casper, Nick Dee, Ximena Opitz-Araya, Ali Cetin, Kimberly A. Smith, Ryder P. Gwinn, Charles Cobbs, Andrew L. Ko, Jeffrey G. Ojemann, C. Dirk Keene, Daniel L. Silbergeld, Susan M. Sunkin, Viviana Gradinaru, Gregory D. Horwitz, Hongkui Zeng, Bosiljka Tasic, Ed S. Lein, Jonathan T. Ting, and Boaz P. Levi. Functional enhancer elements drive subclass-selective expression from mouse to primate neocortex. *Cell Reports*, 34(13):108754, March 2021.

[147] Ben Miles and Peter L. Lee. Achieving Reproducibility and Closed-Loop Automation in Biological Experimentation with an IoT-Enabled Lab of the Future. *SLAS TECHNOLOGY: Translating Life Sciences Innovation*, 23(5):432–439, October 2018. Publisher: SAGE Publications Inc.

[148] Yuki Miura, Min-Yin Li, Omer Revah, Se-Jin Yoon, Genta Narazaki, and Sergiu P. Pașca. Engineering brain assembloids to interrogate human neural circuits. *Nature Protocols*, 17(1):15–35, January 2022. Number: 1 Publisher: Nature Publishing Group.

[149] I. Mody, J. D. Lambert, and U. Heinemann. Low extracellular magnesium induces epileptiform activity and spreading depression in rat hippocampal slices. *Journal of Neurophysiology*, 57(3):869–888, March 1987.

[150] Tjitse van der Molen, Max Lim, Julian Bartram, Zhuowei Cheng, Ash Robbins, David F. Parks, Linda R. Petzold, Andreas Hierlemann, David Haussler, Paul K. Hansma, Kenneth R. Tovar, and Kenneth S. Kosik. RT-Sort: an action potential propagation-based algorithm for real time spike detection and sorting with millisecond latencies, April 2024. Pages: 2024.04.08.588620 Section: New Results.

[151] Zoltán Molnár and Kathleen S. Rockland. Chapter 5 - Cortical columns. In John Rubenstein, Pasko Rakic, Bin Chen, and Kenneth Y. Kwan, editors, *Neural Circuit and Cognitive Development (Second Edition)*, pages 103–126. Academic Press, January 2020.

[152] David D. Mott, Dennis A. Turner, Maxine M. Okazaki, and Darrell V. Lewis. Interneurons of the Dentate–Hilus Border of the Rat Dentate Gyrus: Morphological and Electrophysiological Heterogeneity. *The Journal of Neuroscience*, 17(11):3990–4005, June 1997.

[153] V. B. Mountcastle. The columnar organization of the neocortex. *Brain: A Journal of Neurology*, 120 (Pt 4):701–722, April 1997.

[154] Brian L. Murphy, Raymund Y. K. Pun, Hulian Yin, Christian R. Faulkner, Andreas W. Loepke, and Steve C. Danzer. Heterogeneous Integration of Adult-Generated Granule Cells into the Epileptic Brain. *Journal of Neuroscience*, 31(1):105–117, January 2011. Publisher: Society for Neuroscience Section: Articles.

[155] Elon Musk and Neuralink. An integrated brain-machine interface platform with thousands of channels. *bioRxiv*, page 703801, August 2019.

[156] Jan Müller, Marco Ballini, Paolo Livi, Yihui Chen, Milos Radivojevic, Amir Shadmani, Vijay Viswam, Ian L. Jones, Michele Fiscella, Roland Diggelmann, Alexander Stettler, Urs Frey, Douglas J. Bakkum, and Andreas Hierlemann. High-resolution CMOS MEA platform to study neurons at subcellular, cellular, and network levels. *Lab on a chip*, 15(13):2767–2780, July 2015.

[157] Konstantinos Nasiotis, Martin Cousineau, François Tadel, Adrien Peyrache, Richard M. Leahy, Christopher C. Pack, and Sylvain Baillet. Integrated open-source software for multiscale electrophysiology. *Scientific Data*, 6(1):231, October 2019. Number: 1 Publisher: Nature Publishing Group.

[158] Michael F. Naso, Brian Tomkowicz, William L. Perry, and William R. Strohl. Adeno-Associated Virus (AAV) as a Vector for Gene Therapy. *Biodrugs*, 31(4):317–334, 2017.

[159] Joseph Negri, Vilas Menon, and Tracy L. Young-Pearse. Assessment of Spontaneous Neuronal Activity In Vitro Using Multi-Well Multi-Electrode Arrays: Implications for Assay Development. *eNeuro*, 7(1), January 2020.

[160] Erwin Neher and Bert Sakmann. Single-channel currents recorded from membrane of denervated frog muscle fibres. *Nature*, 260(5554):799–802, April 1976. Number: 5554 Publisher: Nature Publishing Group.

[161] Jonathan P Newman, Ming-fai Fong, Daniel C Millard, Clarissa J Whitmire, Garrett B Stanley, and Steve M Potter. Optogenetic feedback control of neural activity. *eLife*, 4:e07192, July 2015. Publisher: eLife Sciences Publications, Ltd.

[162] Jonathan Paul Newman, Riley Zeller-Townson, Ming-fai Fong, Sharanya Arcot Desai, Robert E. Gross, and Steve M. Potter. Closed-Loop, Multichannel Experimentation Using the Open-Source NeuroRighter Electrophysiology Platform. *Frontiers in Neural Circuits*, 6, 2013. Publisher: Frontiers.

[163] Marie Engelene J. Obien and Urs Frey. Large-Scale, High-Resolution Microelectrode Arrays for Interrogation of Neurons and Networks. In Michela Chiappalone, Valentina Pasquale, and Monica Frega, editors, *In Vitro Neuronal Networks: From Culturing Methods to Neuro-Technological Applications*, Advances in Neurobiology, pages 83–123. Springer International Publishing, Cham, 2019.

[164] Brian D. O'Connor, Denis Yuen, Vincent Chung, Andrew G. Duncan, Xiang Kun Liu, Janice Patricia, Benedict Paten, Lincoln Stein, and Vincent

Ferretti. The Dockstore: enabling modular, community-focused sharing of Docker-based genomics tools and workflows. *F1000Research*, 6, January 2017.

[165] D. Oertel. Synaptic responses and electrical properties of cells in brain slices of the mouse anteroventral cochlear nucleus. *Journal of Neuroscience*, 3(10):2043–2053, October 1983. Publisher: Society for Neuroscience Section: Articles.

[166] Markus Ojala and Gemma C. Garriga. Permutation Tests for Studying Classifier Performance. *The Journal of Machine Learning Research*, 11:1833–1863, August 2010.

[167] Tatsuya Osaki, Tomoya Duenki, Siu Yu A. Chow, Yasuhiro Ikegami, Romain Beaubois, Timothée Levi, Nao Nakagawa-Tamagawa, Yoji Hirano, and Yoshiho Ikeuchi. Complex activity and short-term plasticity of human cerebral organoids reciprocally connected with axons. *Nature Communications*, 15(1):2945, April 2024. Publisher: Nature Publishing Group.

[168] Marius Pachitariu, Nicholas Steinmetz, Shabnam Kadir, Matteo Carandini, and Harris Kenneth D. Kilosort: realtime spike-sorting for extracellular electrophysiology with hundreds of channels. *bioRxiv*, page 061481, June 2016. Publisher: Cold Spring Harbor Laboratory Section: New Results.

[169] J. Park, G. Kim, and S. Jung. A 128-Channel FPGA-Based Real-Time Spike-Sorting Bidirectional Closed-Loop Neural Interface System. *IEEE Transactions on Neural Systems and Rehabilitation Engineering*, 25(12):2227–2238, December 2017. Conference Name: IEEE Transactions on Neural Systems and Rehabilitation Engineering.

[170] Yoonseok Park, Colin K. Franz, Hanjun Ryu, Haiwen Luan, Kristen Y. Cotton, Jong Uk Kim, Ted S. Chung, Shiwei Zhao, Abraham Vazquez-Guardado, Da Som Yang, Kan Li, Raudel Avila, Jack K. Phillips, Maria J. Quezada, Hokyung Jang, Sung Soo Kwak, Sang Min Won, Kyeongha Kwon, Hyoyoung Jeong, Amay J. Bandodkar, Mengdi Han, Hangbo Zhao, Gabrielle R. Osher, Heling Wang, KunHyuck Lee, Yihui Zhang, Yonggang Huang, John D. Finan, and John A. Rogers. Three-dimensional, multifunctional neural interfaces for cortical spheroids and engineered assembloids. *Science Advances*, 7(12):eabf9153, March 2021. Publisher: American Association for the Advancement of Science Section: Research Article.

[171] Yunjeong Park, Sebastian Hernandez, Cristian O. Hernandez, Hunter E. Schweiger, Houpu Li, Kateryna Voitiuk, Harika Dechiraju, Nico Hawthorne,

Elana M. Muzzy, John A. Selberg, Frederika N. Sullivan, Roberto Urcuyo, Sofie R. Salama, Elham Aslankoohi, Heather J. Knight, Mircea Teodorescu, Mohammed A. Mostajo-Radji, and Marco Rolandi. Modulation of neuronal activity in cortical organoids with bioelectronic delivery of ions and neurotransmitters. *Cell Reports Methods*, 4(1):100686, January 2024.

[172] Yunjeong Park, Sebastian Hernandez, Cristian O. Hernandez, Hunter E. Schweiger, Houpu Li, Kateryna Voitiuk, Harika Dechiraju, Nico Hawthorne, Elana M. Muzzy, John A. Selberg, Frederika N. Sullivan, Roberto Urcuyo, Sofie R. Salama, Elham Aslankoohi, Mircea Teodorescu, Mohammed A. Mostajo-Radji, and Marco Rolandi. Modulation of neuronal activity in cortical organoids with bioelectronic delivery of ions and neurotransmitters, June 2023. Pages: 2023.06.10.544416 Section: New Results.

[173] David F. Parks, Kateryna Voitiuk, Jinghui Geng, Matthew A. T. Elliott, Matthew G. Keefe, Erik A. Jung, Ash Robbins, Pierre V. Baudin, Victoria T. Ly, Nico Hawthorne, Dylan Yong, Sebastian E. Sanso, Nick Rezaee, Jess Sevetson, Spencer T. Seiler, Rob Currie, Keith B. Hengen, Tomasz J. Nowakowski, Sofie R. Salama, Mircea Teodorescu, and David Haussler. Internet of Things Architecture for High Throughput Biology. page 2021.07.29.453595, August 2021. Company: Cold Spring Harbor Laboratory Distributor: Cold Spring Harbor Laboratory Label: Cold Spring Harbor Laboratory Section: New Results Type: article.

[174] David F. Parks, Kateryna Voitiuk, Jinghui Geng, Matthew A. T. Elliott, Matthew G. Keefe, Erik A. Jung, Ash Robbins, Pierre V. Baudin, Victoria T. Ly, Nico Hawthorne, Dylan Yong, Sebastian E. Sanso, Nick Rezaee, Jess Sevetson, Spencer T. Seiler, Rob Currie, Alex A. Pollen, Keith B. Hengen, Tomasz J. Nowakowski, Mohammed A. Mostajo-Radji, Sofie R. Salama, Mircea Teodorescu, and David Haussler. Internet of Things Architecture for Cellular Biology, February 2022. Pages: 2021.07.29.453595 Section: New Results.

[175] David F. Parks, Kateryna Voitiuk, Jinghui Geng, Matthew A. T. Elliott, Matthew G. Keefe, Erik A. Jung, Ash Robbins, Pierre V. Baudin, Victoria T. Ly, Nico Hawthorne, Dylan Yong, Sebastian E. Sanso, Nick Rezaee, Jess L. Sevetson, Spencer T. Seiler, Rob Currie, Alex A. Pollen, Keith B. Hengen, Tomasz J. Nowakowski, Mohammed A. Mostajo-Radji, Sofie R. Salama, Mircea Teodorescu, and David Haussler. IoT cloud laboratory: Internet of Things architecture for cellular biology. *Internet of Things*, page 100618, September 2022.

[176] Jolien Pas, Charalampos Pitsalidis, Dimitrios A. Koutsouras, Pascale P. Quilichini, Francesca Santoro, Bianxiao Cui, Laurent Gallais, Rodney P. O'Connor, George G. Malliaras, and Róisín M. Owens. Neurospheres on Patterned PEDOT:PSS Microelectrode Arrays Enhance Electrophysiology Recordings. *Advanced Biosystems*, 2(1):1700164, January 2018.

[177] Austin P. Passaro and Steven L. Stice. Electrophysiological Analysis of Brain Organoids: Current Approaches and Advancements. *Frontiers in Neuroscience*, 14, 2021. Publisher: Frontiers.

[178] João Passos, Sérgio Ivan Lopes, Filipe Manuel Clemente, Pedro Miguel Moreira, Markel Rico-González, Pedro Bezerra, and Luís Paulo Rodrigues. Wearables and Internet of Things (IoT) Technologies for Fitness Assessment: A Systematic Review. *Sensors*, 21(16):5418, January 2021. Number: 16 Publisher: Multidisciplinary Digital Publishing Institute.

[179] Anca M. Paşca, Jin-Young Park, Hyun-Woo Shin, Qihao Qi, Omer Revah, Rebecca Krasnoff, Ruth O'Hara, A. Jeremy Willsey, Theo D. Palmer, and Sergiu P. Paşca. Human 3D Cellular Model of Hypoxic Brain Injury of Prematurity. *Nature medicine*, 25(5):784–791, May 2019.

[180] Sergiu P. Paşca. Assembling human brain organoids. *Science*, 363(6423):126–127, January 2019. Publisher: American Association for the Advancement of Science Section: Perspective.

[181] Jeffrey M. Perkel. The Internet of Things comes to the lab. *Nature*, 542(7639):125–126, February 2017. Bandiera_abtest: a Cg_type: Nature Research Journals Number: 7639 Primary_atype: Special Features Publisher: Nature Publishing Group Subject_term: Information technology;Technology Subject_term_id: information-technology;technology.

[182] Jeffrey M. Perkel. The Internet of Things comes to the lab. *Nature*, 542(7639):125–126, February 2017. Number: 7639 Publisher: Nature Publishing Group.

[183] Alan Peters. The Morphology of Minicolumns. In Gene J. Blatt, editor, *The Neurochemical Basis of Autism: From Molecules to Minicolumns*, pages 45–68. Springer US, Boston, MA, 2010.

[184] Antoine Pirog, Yannick Bornat, Romain Perrier, Matthieu Raoux, Manon Jaffredo, Adam Quotb, Jochen Lang, Noëlle Lewis, and Sylvie Renaud. Multimed: An Integrated, Multi-Application Platform for the Real-Time Recording and Sub-Millisecond Processing of Biosignals. *Sensors (Basel, Switzerland)*, 18(7), June 2018.

[185] Daniele Poli, Vito P. Pastore, and Paolo Massobrio. Functional connectivity in in vitro neuronal assemblies. *Frontiers in Neural Circuits*, 9, 2015. Publisher: Frontiers.

[186] Alex A. Pollen, Aparna Bhaduri, Madeline G. Andrews, Tomasz J. Nowakowski, Olivia S. Meyerson, Mohammed A. Mostajo-Radji, Elizabeth Di Lullo, Beatriz Alvarado, Melanie Bedolli, Max L. Dougherty, Ian T. Fiddes, Zev N. Kronenberg, Joe Shuga, Anne A. Leyrat, Jay A. West, Marina Bershteyn, Craig B. Lowe, Bryan J. Pavlovic, Sofie R. Salama, David Haussler, Evan E. Eichler, and Arnold R. Kriegstein. Establishing Cerebral Organoids as Models of Human-Specific Brain Evolution. *Cell*, 176(4):743–756.e17, February 2019. Publisher: Elsevier.

[187] Carlos R. Ponce, Will Xiao, Peter F. Schade, Till S. Hartmann, Gabriel Kreiman, and Margaret S. Livingstone. Evolving Images for Visual Neurons Using a Deep Generative Network Reveals Coding Principles and Neuronal Preferences. *Cell*, 177(4):999–1009.e10, May 2019.

[188] Steve M. Potter. Chapter 4 Distributed processing in cultured neuronal networks. In *Progress in Brain Research*, volume 130 of *Advances in Neural Population Coding*, pages 49–62. Elsevier, January 2001.

[189] Steve M. Potter, Ahmed El Hady, and Eberhard E. Fetz. Closed-loop neuroscience and neuroengineering. *Frontiers in Neural Circuits*, 8, 2014. Publisher: Frontiers.

[190] Jan Putzeys, Bogdan C. Raducanu, Alain Carton, Jef De Ceulaer, Bill Karsh, Joshua H. Siegle, Nick Van Helleputte, Timothy D. Harris, Barundeb Dutta, Silke Musa, and Carolina Mora Lopez. Neuropixels Data-Acquisition System: A Scalable Platform for Parallel Recording of 10 000+ Electrophysiological Signals. *IEEE Transactions on Biomedical Circuits and Systems*, 13(6):1635–1644, December 2019.

[191] Giorgia Quadrato, Tuan Nguyen, Evan Z. Macosko, John L. Sherwood, Sung Min Yang, Daniel Berger, Natalie Maria, Jorg Scholvin, Melissa Goldman, Justin Kinney, Edward S. Boyden, Jeff Lichtman, Ziv M. Williams, Steven A. McCarroll, and Paola Arlotta. Cell diversity and network dynamics in photosensitive human brain organoids. *Nature*, 545(7652):48–53, May 2017.

[192] R. Quian Quiroga, Z. Nadasdy, and Y. Ben-Shaul. Unsupervised Spike Detection and Sorting with Wavelets and Superparamagnetic Clustering. *Neural Computation*, 16(8):1661–1687, August 2004.

[193] Maithra Raghu and Eric Schmidt. A Survey of Deep Learning for Scientific Discovery. *arXiv:2003.11755 [cs, stat]*, March 2020. arXiv: 2003.11755.

[194] Negah Rahmati, Kieran P. Normoyle, Joseph Glykys, Volodymyr I. Dzhala, Kyle P. Lillis, Kristopher T. Kahle, Rehan Raiyyani, Theju Jacob, and Kevin J. Staley. Unique Actions of GABA Arising from Cytoplasmic Chloride Microdomains. *Journal of Neuroscience*, 41(23):4957–4975, June 2021. Publisher: Society for Neuroscience Section: Research Articles.

[195] F. Ann Ran, Patrick D. Hsu, Jason Wright, Vineeta Agarwala, David A. Scott, and Feng Zhang. Genome engineering using the CRISPR-Cas9 system. *Nature Protocols*, 8(11):2281–2308, November 2013. Publisher: Nature Publishing Group.

[196] Hernan Gonzalo Rey, Carlos Pedreira, and Rodrigo Quian Quiroga. Past, present and future of spike sorting techniques. *Brain Research Bulletin*, 119:106–117, October 2015.

[197] J. D. Rolston, R. E. Gross, and S. M. Potter. NeuroRighter: Closed-loop multielectrode stimulation and recording for freely moving animals and cell cultures. In *2009 Annual International Conference of the IEEE Engineering in Medicine and Biology Society*, pages 6489–6492, September 2009. ISSN: 1558-4615.

[198] John D. Rolston, Robert E. Gross, and Steve M. Potter. Closed-Loop, Open-Source Electrophysiology. *Frontiers in Neuroscience*, 4, 2010. Publisher: Frontiers.

[199] Cyrille Rossant, Shabnam N. Kadir, Dan F. M. Goodman, John Schulman, Maximilian L. D. Hunter, Aman B. Saleem, Andres Grosmark, Mariano Belluscio, George H. Denfield, Alexander S. Ecker, Andreas S. Tolias, Samuel Solomon, Gyorgy Buzsaki, Matteo Carandini, and Kenneth D. Harris. Spike sorting for large, dense electrode arrays. *Nature Neuroscience*, 19(4):634–641, April 2016.

[200] Nina M. Rzechorzek, Magdalena A. Sutcliffe, Andrei Mihut, Koby Baranes, Nuzli Karam, Daniel Lloyd-Davies Sánchez, Sew Y. Peak-Chew, Aiwei Zeng, Noah Poulin, Estere Seinkmane, Kaiser Karim, Christopher M. Proctor, Mark Kotter, Madeline A. Lancaster, and Andrew D. Beale. Circadian clocks in human cerebral organoids, February 2024. Pages: 2024.02.20.580978 Section: New Results.

[201] Melinda Rácz, Csaba Liber, Erik Németh, Richárd Fiáth, János Rokai, István Harmati, István Ulbert, and Gergely Márton. Spike detection and sorting with deep learning. *Journal of Neural Engineering*, 17(1):016038, January 2020. Publisher: IOP Publishing.

[202] Pintu Kumar Sadhu, Venkata P. Yanambaka, and Ahmed Abdelgawad. Internet of Things: Security and Solutions Survey. *Sensors*, 22(19):7433, January 2022. Number: 19 Publisher: Multidisciplinary Digital Publishing Institute.

[203] Farahnaz Sadoughi, Ali Behmanesh, and Nasrin Sayfouri. Internet of things in medicine: A systematic mapping study. *Journal of Biomedical Informatics*, 103:103383, March 2020.

[204] Hideya Sakaguchi, Yuki Ozaki, Tomoka Ashida, Takayoshi Matsubara, Naotaka Oishi, Shunsuke Kihara, and Jun Takahashi. Self-Organized Synchronous Calcium Transients in a Cultured Human Neural Network Derived from Cerebral Organoids. *Stem Cell Reports*, 13(3):458–473, June 2019.

[205] Joshua I. Sanders and Adam Kepecs. A low-cost programmable pulse generator for physiology and behavior. *Frontiers in Neuroengineering*, 7, 2014. Publisher: Frontiers.

[206] Galina Schmunk, Chang N. Kim, Sarah S. Soliman, Matthew G. Keefe, Derek Bogdanoff, Dario Tejera, Ryan S. Ziffra, David Shin, Denise E. Allen, Bryant B. Chhun, Christopher S. McGinnis, Ethan A. Winkler, Adib A. Abla, Edward F. Chang, Zev J. Gartner, Shalin B. Mehta, Xianhua Piao, Keith B. Hengen, and Tomasz J. Nowakowski. Human microglia upregulate cytokine signatures and accelerate maturation of neural networks. *bioRxiv*, page 2020.03.24.006874, March 2020. Publisher: Cold Spring Harbor Laboratory Section: New Results.

[207] Jörg Scholvin, Justin P. Kinney, Jacob G. Bernstein, Caroline Moore-Kochlacs, Nancy Kopell, Clifton G. Fonstad, and Edward S. Boyden. Close-Packed Silicon Microelectrodes for Scalable Spatially Oversampled Neural Recording. *IEEE Transactions on Biomedical Engineering*, 63(1):120–130, January 2016.

[208] Manuel Schröter, Congwei Wang, Marco Terrigno, Philipp Hornauer, Ziqiang Huang, Ravi Jagasia, and Andreas Hierlemann. Functional imaging of brain organoids using high-density microelectrode arrays. *Mrs Bulletin*, 47(6):530–544, 2022.

[209] Stephanie C. Seeman, Brian J. Mogen, Eberhard E. Fetz, and Steve I. Perlmutter. Paired Stimulation for Spike-Timing-Dependent Plasticity in Primate Sensorimotor Cortex. *Journal of Neuroscience*, 37(7):1935–1949, February 2017. Publisher: Society for Neuroscience Section: Research Articles.

[210] Spencer T. Seiler, Gary L. Mantalas, John Selberg, Sergio Cordero, Sebastian Torres-Montoya, Pierre V. Baudin, Victoria T. Ly, Finn Amend, Liam Tran, Ryan N. Hoffman, Marco Rolandi, Richard E. Green, David Haussler, Sofie R. Salama, and Mircea Teodorescu. Modular automated microfluidic cell culture platform reduces glycolytic stress in cerebral cortex organoids, July 2022. Pages: 2022.07.13.499938 Section: New Results.

[211] Tal Sharf, Tjitse van der Molen, Elmer Guzman, Stella M. K. Glasauer, Gabriel Luna, Zhouwei Cheng, Morgane Audouard, Kamalini G. Ranasinghe, Kiwamu Kudo, Srikantan S. Nagarajan, Kenneth R. Tovar, Linda R. Petzold, Paul K. Hansma, and Kenneth S. Kosik. Intrinsic network activity in human brain organoids. *bioRxiv*, page 2021.01.28.428643, January 2021. Publisher: Cold Spring Harbor Laboratory Section: New Results.

[212] Tal Sharf, Tjitse van der Molen, Stella M. K. Glasauer, Elmer Guzman, Alessio P. Buccino, Gabriel Luna, Zhuowei Cheng, Morgane Audouard, Kamalini G. Ranasinghe, Kiwamu Kudo, Srikantan S. Nagarajan, Kenneth R. Tovar, Linda R. Petzold, Andreas Hierlemann, Paul K. Hansma, and Kenneth S. Kosik. Functional neuronal circuitry and oscillatory dynamics in human brain organoids. *Nature Communications*, 13(1):4403, July 2022. Number: 1 Publisher: Nature Publishing Group.

[213] Alex Shcheglovitov, Yueqi Wang, Laura Bell, Chad Russell, Celeste Armstrong, and Jay Spampanato. Human cortical organoids from single iPSC-derived neural rosettes for studying human cortical development and disorders. *The FASEB Journal*, 33(1_supplement):205.3–205.3, April 2019. Publisher: Federation of American Societies for Experimental Biology.

[214] David Shin, Chang N. Kim, Jayden Ross, Kelsey M. Hennick, Sih-Rong Wu, Neha Paranjape, Rachel Leonard, Jerrick C. Wang, Matthew G. Keefe, Bryan J. Pavlovic, Kevin C. Donohue, Clara Moreau, Emilie M. Wigdor, H. Hanh Larson, Denise E. Allen, Cathryn R. Cadwell, Aparna Bhaduri, Galina Popova, Carrie E. Bearden, Alex A. Pollen, Sebastien Jacquemont, Stephan J. Sanders, David Haussler, Arun P. Wiita, Nicholas A. Frost, Vikaas S. Sohal, and Tomasz J. Nowakowski. Thalamocortical organoids

enable *in vitro* modeling of 22q11.2 microdeletion associated with neuropsychiatric disorders. *Cell Stem Cell*, 31(3):421–432.e8, March 2024.

[215] Joshua H Siegle, Gregory J Hale, Jonathan P Newman, and Jakob Voigts. Neural ensemble communities: open-source approaches to hardware for large-scale electrophysiology. *Current Opinion in Neurobiology*, 32:53–59, June 2015.

[216] Joshua H. Siegle, Xiaoxuan Jia, Séverine Durand, Sam Gale, Corbett Bennett, Nile Graddis, Greggory Heller, Tamina K. Ramirez, Hannah Choi, Jennifer A. Luviano, Peter A. Groblewski, Ruweida Ahmed, Anton Arkhipov, Amy Bernard, Yazan N. Billeh, Dillan Brown, Michael A. Buice, Nicolas Cain, Shiella Caldejon, Linzy Casal, Andrew Cho, Maggie Chvilicek, Timothy C. Cox, Kael Dai, Daniel J. Denman, Saskia E. J. de Vries, Roald Dietzman, Luke Esposito, Colin Farrell, David Feng, John Galbraith, Marina Garrett, Emily C. Gelfand, Nicole Hancock, Julie A. Harris, Robert Howard, Brian Hu, Ross Hytnen, Ramakrishnan Iyer, Erika Jessett, Katelyn Johnson, India Kato, Justin Kiggins, Sophie Lambert, Jerome Lecoq, Peter Ledochowitsch, Jung Hoon Lee, Arielle Leon, Yang Li, Elizabeth Liang, Fuhui Long, Kyla Mace, Jose Melchior, Daniel Millman, Tyler Mollenkopf, Chelsea Nayan, Lydia Ng, Kiet Ngo, Thuyahn Nguyen, Philip R. Nicovich, Kat North, Gabriel Koch Ocker, Doug Ollerenshaw, Michael Oliver, Marius Pachitariu, Jed Perkins, Melissa Reding, David Reid, Miranda Robertson, Kara Ronellenfitch, Sam Seid, Cliff Slaughterbeck, Michelle Stoecklin, David Sullivan, Ben Sutton, Jackie Swapp, Carol Thompson, Kristen Turner, Wayne Wakeman, Jennifer D. Whitesell, Derric Williams, Ali Williford, Rob Young, Hongkui Zeng, Sarah Naylor, John W. Phillips, R. Clay Reid, Stefan Mihalas, Shawn R. Olsen, and Christof Koch. Survey of spiking in the mouse visual system reveals functional hierarchy. *Nature*, 592(7852):86–92, April 2021.

[217] Joshua H Siegle, Aarón Cuevas López, Yogi A Patel, Kirill Abramov, Shay Ohayon, and Jakob Voigts. Open Ephys: an open-source, plugin-based platform for multichannel electrophysiology. *Journal of Neural Engineering*, 14(4):045003, August 2017.

[218] S. J. Singer and Garth L. Nicolson. The Fluid Mosaic Model of the Structure of Cell Membranes. *Science*, 175(4023):720–731, February 1972. Publisher: American Association for the Advancement of Science.

[219] Jens Chr. Skou. The influence of some cations on an adenosine triphos-

phatase from peripheral nerves. *Biochimica et Biophysica Acta*, 23:394–401, January 1957.

[220] Slack. Unlock your productivity potential with Slack Platform.

[221] Aidan Slattery, Zhenghui Wen, Pauline Tenblad, Jesús Sanjosé-Orduna, Diego Pintossi, Tim den Hartog, and Timothy Noël. Automated self-optimization, intensification, and scale-up of photocatalysis in flow. *Science*, 383(6681):eadj1817, January 2024. Publisher: American Association for the Advancement of Science.

[222] Steven A. Sloan, Spyros Darmanis, Nina Huber, Themasap A. Khan, Fikri Birey, Christine Caneda, Richard Reimer, Stephen R. Quake, Ben A. Barres, and Sergiu P. Paşca. Human Astrocyte Maturation Captured in 3D Cerebral Cortical Spheroids Derived from Pluripotent Stem Cells. *Neuron*, 95(4):779–790.e6, August 2017.

[223] Larry Smarr, Camille Crittenden, Thomas DeFanti, John Graham, Dmitry Mishin, Richard Moore, Philip Papadopoulos, and Frank Würthwein. The Pacific Research Platform: Making High-Speed Networking a Reality for the Scientist. In *Proceedings of the Practice and Experience on Advanced Research Computing*, PEARC '18, pages 1–8, Pittsburgh, PA, USA, July 2018. Association for Computing Machinery.

[224] Micha E. Spira, Shun-Ho Huang, Nava Shmoel, and Hadas Erez. Multi-site Intracellular Recordings by MEA. In Michela Chiappalone, Valentina Pasquale, and Monica Frega, editors, *In Vitro Neuronal Networks: From Culturing Methods to Neuro-Technological Applications*, Advances in Neurobiology, pages 125–153. Springer International Publishing, Cham, 2019.

[225] François St-Pierre, Jesse D. Marshall, Ying Yang, Yiyang Gong, Mark J. Schnitzer, and Michael Z. Lin. High-fidelity optical reporting of neuronal electrical activity with an ultrafast fluorescent voltage sensor. *Nature Neuroscience*, 17(6):884–889, June 2014.

[226] Nicholas A. Steinmetz, Cagatay Aydin, Anna Lebedeva, Michael Okun, Marius Pachitariu, Marius Bauza, Maxime Beau, Jai Bhagat, Claudia Böhm, Martijn Broux, Susu Chen, Jennifer Colonell, Richard J. Gardner, Bill Karsh, Fabian Kloosterman, Dimitar Kostadinov, Carolina Mora-Lopez, John O'Callaghan, Junchol Park, Jan Putzeys, Britton Sauerbrei, Rik J. J. van Daal, Abraham Z. Vollan, Shiwei Wang, Marleen Welkenhuysen, Zhiwen Ye, Joshua T. Dudman, Barundeb Dutta, Adam W. Hantman, Kenneth D. Harris, Albert K. Lee, Edvard I. Moser, John O'Keefe, Alfonso

Renart, Karel Svoboda, Michael Häusser, Sebastian Haesler, Matteo Carandini, and Timothy D. Harris. Neuropixels 2.0: A miniaturized high-density probe for stable, long-term brain recordings. *Science*, 372(6539), April 2021. Publisher: American Association for the Advancement of Science Section: Research Article.

[227] Christoph Stosiek, Olga Garaschuk, Knut Holthoff, and Arthur Konnerth. In vivo two-photon calcium imaging of neuronal networks. *Proceedings of the National Academy of Sciences*, 100(12):7319–7324, June 2003. Publisher: National Academy of Sciences Section: Biological Sciences.

[228] Peng Su, Yuanyuan Chen, and Mengmeng Lu. Smart city information processing under internet of things and cloud computing. *The Journal of Supercomputing*, 78(3):3676–3695, February 2022.

[229] Kazutoshi Takahashi and Shinya Yamanaka. Induction of Pluripotent Stem Cells from Mouse Embryonic and Adult Fibroblast Cultures by Defined Factors. *Cell*, 126(4):663–676, August 2006. Publisher: Elsevier.

[230] Mattia Tambaro, Marta Bisio, Marta Maschietto, Alessandro Leparulo, and Stefano Vassanelli. FPGA Design Integration of a 32-Microelectrodes Low-Latency Spike Detector in a Commercial System for Intracortical Recordings. *Digital*, 1(1):34–53, March 2021. Number: 1 Publisher: Multidisciplinary Digital Publishing Institute.

[231] Jonathan T. Ting, Brian Kalmbach, Peter Chong, Rebecca de Frates, C. Dirk Keene, Ryder P. Gwinn, Charles Cobbs, Andrew L. Ko, Jeffrey G. Ojemann, Richard G. Ellenbogen, Christof Koch, and Ed Lein. A robust ex vivo experimental platform for molecular-genetic dissection of adult human neocortical cell types and circuits. *Scientific Reports*, 8(1):8407, May 2018. Publisher: Nature Publishing Group.

[232] Mario A. Torres-Acosta, Gary J. Lye, and Duygu Dikicioglu. Automated liquid-handling operations for robust, resilient, and efficient bio-based laboratory practices. *Biochemical Engineering Journal*, 188:108713, December 2022.

[233] Cleber A. Trujillo, Richard Gao, Priscilla D. Negraes, Jing Gu, Justin Buchanan, Sebastian Preissl, Allen Wang, Wei Wu, Gabriel G. Haddad, Isaac A. Chaim, Alain Domissy, Matthieu Vandenberghe, Anna Devor, Gene W. Yeo, Bradley Voytek, and Alysson R. Muotri. Complex Oscillatory Waves Emerging from Cortical Organoids Model Early Human Brain Network Development. *Cell Stem Cell*, 25(4):558–569.e7, October 2019.

[234] David Tsai, Esha John, Tarun Chari, Rafael Yuste, and Kenneth Shepard. High-channel-count, high-density microelectrode array for closed-loop investigation of neuronal networks. In *2015 37th Annual International Conference of the IEEE Engineering in Medicine and Biology Society (EMBC)*, pages 7510–7513, August 2015. ISSN: 1558-4615.

[235] Dina Tsybulsky and Erez Sinai. IoT in Project-Based Biology Learning: Students' Experiences and Skill Development. *Journal of Science Education and Technology*, 31(4):542–553, August 2022.

[236] Gina G. Turrigiano and Sacha B. Nelson. Homeostatic plasticity in the developing nervous system. *Nature Reviews Neuroscience*, 5(2):97–107, February 2004. Number: 2 Publisher: Nature Publishing Group.

[237] Jan Tønnesen, Andreas T. Sørensen, Karl Deisseroth, Cecilia Lundberg, and Merab Kokaia. Optogenetic control of epileptiform activity. *Proceedings of the National Academy of Sciences*, 106(29):12162–12167, July 2009. Publisher: Proceedings of the National Academy of Sciences.

[238] Francesco Paolo Ulloa Severino, Jelena Ban, Qin Song, Mingliang Tang, Ginestra Bianconi, Guosheng Cheng, and Vincent Torre. The role of dimensionality in neuronal network dynamics. *Scientific Reports*, 6(1):29640, July 2016. Number: 1 Publisher: Nature Publishing Group.

[239] Jean-Paul Urenda, Ashley Del Dosso, Marcella Birtele, and Giorgia Quadrato. Present and Future Modeling of Human Psychiatric Connectopathies With Brain Organoids. *Biological Psychiatry*, 93(7):606–615, April 2023.

[240] Julien Vezoli, Loïc Magrou, Rainer Goebel, Xiao-Jing Wang, Kenneth Knoblauch, Martin Vinck, and Henry Kennedy. Cortical hierarchy, dual counterstream architecture and the importance of top-down generative networks. *NeuroImage*, 225:117479, January 2021.

[241] Annamaria Vezzani, Mirko Conti, Ada De Luigi, Teresa Ravizza, Daniela Moneta, Francesco Marchesi, and Maria Grazia De Simoni. Interleukin-1 Immunoreactivity and Microglia Are Enhanced in the Rat Hippocampus by Focal Kainate Application: Functional Evidence for Enhancement of Electrographic Seizures. *The Journal of Neuroscience*, 19(12):5054–5065, June 1999.

[242] Johannes Vierock, Enrico Schiewer, Christiane Grimm, Andrey Rozenberg, I-Wen Chen, Linda Tillert, Alejandro G. Castro Scalise, Marilù Casini,

Sandra Augustin, Dimitrii Tanese, Benoît C. Forget, Rémi Peyronnet, Franziska Schneider-Warme, Valentina Emiliani, Oded Béjà, and Peter Hegemann. WiChR, a highly potassium-selective channelrhodopsin for low-light one- and two-photon inhibition of excitable cells. *Science Advances*, 8(49):eadd7729, November 2022. Publisher: American Association for the Advancement of Science.

[243] S. Vishnu, S.R. Jino Ramson, and R. Jegan. Internet of Medical Things (IoMT) - An overview. In *2020 5th International Conference on Devices, Circuits and Systems (ICDCS)*, pages 101–104, March 2020. ISSN: 2644-1802.

[244] Kateryna Voitiuk, Jinghui Geng, Matthew G. Keefe, David F. Parks, Sebastian E. Sanso, Nico Hawthorne, Daniel B. Freeman, Mohammed A. Mostajo-Radji, Tomasz J. Nowakowski, Sofie R. Salama, Mircea Teodorescu, and David Haussler. Light-weight Electrophysiology Hardware and Software Platform for Cloud-Based Neural Recording Experiments. *bioRxiv*, page 2021.05.18.444685, May 2021. Publisher: Cold Spring Harbor Laboratory Section: New Results.

[245] Kateryna Voitiuk, Spencer T. Seiler, Mirella Pessoa de Melo, Jinghui Geng, Sebastian Hernandez, Hunter E. Schweiger, Jess L. Sevetson, David F. Parks, Ash Robbins, Sebastian Torres-Montoya, Drew Ehrlich, Matthew A. T. Elliott, Tal Sharf, David Haussler, Mohammed A. Mostajo-Radji, Sofie R. Salama, and Mircea Teodorescu. A feedback-driven IoT microfluidic, electrophysiology, and imaging platform for brain organoid studies, March 2024. Pages: 2024.03.15.585237 Section: New Results.

[246] D. Wagenaar, T.B. DeMarse, and S.M. Potter. MeaBench: A toolset for multi-electrode data acquisition and on-line analysis. In *Conference Proceedings. 2nd International IEEE EMBS Conference on Neural Engineering, 2005.*, pages 518–521, March 2005. ISSN: 1948-3554.

[247] Daniel A. Wagenaar, Radhika Madhavan, Jerome Pine, and Steve M. Potter. Controlling Bursting in Cortical Cultures with Closed-Loop Multi-Electrode Stimulation. *The Journal of Neuroscience*, 25(3):680–688, January 2005.

[248] Sidra Waheed, Joan M. Cabot, Niall P. Macdonald, Trevor Lewis, Rosanne M. Guijt, Brett Paull, and Michael C. Breadmore. 3D printed microfluidic devices: enablers and barriers. *Lab on a Chip*, 16(11):1993–2013, May 2016. Publisher: The Royal Society of Chemistry.

[249] A. A. P. Wai, H. Dajiang, and N. S. Huat. IoT-enabled multimodal sensing headwear system. In *2018 IEEE 4th World Forum on Internet of Things (WF-IoT)*, pages 286–290, February 2018.

[250] Emily A. Walters, Jessica L. Brown, Rebecca Krisher, Steve Voelkel, and Jason E. Swain. Impact of a controlled culture temperature gradient on mouse embryo development and morphokinetics. *Reproductive BioMedicine Online*, 40(4):494–499, April 2020.

[251] Momoko Watanabe, Jessie E. Buth, Neda Vishlaghi, Luis de la Torre-Ubieta, Jiannis Taxidis, Baljit S. Khakh, Giovanni Coppola, Caroline A. Pearson, Ken Yamauchi, Danyang Gong, Xinghong Dai, Robert Damoiseaux, Roghiyh Aliyari, Simone Liebscher, Katja Schenke-Layland, Christine Caneda, Eric J. Huang, Ye Zhang, Genhong Cheng, Daniel H. Geschwind, Peyman Golshani, Ren Sun, and Bennett G. Novitch. Self-Organized Cerebral Organoids with Human-Specific Features Predict Effective Drugs to Combat Zika Virus Infection. *Cell Reports*, 21(2):517–532, October 2017.

[252] Sage Weil, Scott A. Brandt, Ethan L. Miller, Darrell D. E. Long, and Carlos Maltzahn. Ceph: A Scalable, High-Performance Distributed File System. In *Proceedings of the 7th Conference on Operating Systems Design and Implementation (OSDI '06)*. November 2006.

[253] Brandon G. Wong, Christopher P. Mancuso, Szilvia Kiriakov, Caleb J. Bashor, and Ahmad S. Khalil. Precise, automated control of conditions for high-throughput growth of yeast and bacteria with eVOLVER. *Nature Biotechnology*, 36(7):614–623, August 2018. Number: 7 Publisher: Nature Publishing Group.

[254] Robert C. Wykes, Joost H. Heeroma, Laura Mantoan, Kaiyu Zheng, Douglas C. MacDonald, Karl Deisseroth, Kevan S. Hashemi, Matthew C. Walker, Stephanie Schorge, and Dimitri M. Kullmann. Optogenetic and potassium channel gene therapy in a rodent model of focal neocortical epilepsy. *Science Translational Medicine*, 4(161):161ra152, November 2012.

[255] Robert C. Wykes, Dimitri M. Kullmann, Ivan Pavlov, and Vincent Magloire. Optogenetic approaches to treat epilepsy. *Journal of Neuroscience Methods*, 260:215–220, February 2016.

[256] Guobao Xu, Yanjun Shi, Xueyan Sun, and Weiming Shen. Internet of Things in Marine Environment Monitoring: A Review. *Sensors*, 19(7):1711, Jan-

uary 2019. Number: 7 Publisher: Multidisciplinary Digital Publishing Institute.

[257] Yuichiro Yada, Takeshi Mita, Akihiro Sanada, Ryuichi Yano, Ryohei Kanzaki, Douglas J. Bakkum, Andreas Hierlemann, and Hirokazu Takahashi. Development of neural population activity toward self-organized criticality. *Neuroscience*, 343:55–65, 2017.

[258] Abraam M. Yakoub. Cerebral organoids exhibit mature neurons and astrocytes and recapitulate electrophysiological activity of the human brain. *Neural Regeneration Research*, 14(5):757, May 2019. Publisher: Wolters Kluwer – Medknow Publications.

[259] Long Yang, Kwang Lee, Jomar Villagracia, and Sotiris C. Masmanidis. Open source silicon microprobes for high throughput neural recording. *Journal of Neural Engineering*, 17(1):016036, January 2020. Publisher: IOP Publishing.

[260] Zhe Yang, Qihao Zhou, Lei Lei, Kan Zheng, and Wei Xiang. An IoT-cloud Based Wearable ECG Monitoring System for Smart Healthcare. *Journal of Medical Systems*, 40(12):286, October 2016.

[261] Zizhen Yao, Cindy T. J. van Velthoven, Thuc Nghi Nguyen, Jeff Goldy, Adriana E. Sedeno-Cortes, Fahimeh Baftizadeh, Darren Bertagnolli, Tamara Casper, Megan Chiang, Kirsten Crichton, Song-Lin Ding, Olivia Fong, Emma Garren, Alexandra Glandon, Nathan W. Gouwens, James Gray, Lucas T. Graybuck, Michael J. Hawrylycz, Daniel Hirschstein, Matthew Kroll, Kanan Lathia, Changkyu Lee, Boaz Levi, Delissa McMillen, Stephanie Mok, Thanh Pham, Qingzhong Ren, Christine Rimorin, Nadiya Shapovalova, Josef Sulc, Susan M. Sunkin, Michael Tieu, Amy Torkelson, Herman Tung, Katelyn Ward, Nick Dee, Kimberly A. Smith, Bosiljka Tasic, and Hongkui Zeng. A taxonomy of transcriptomic cell types across the isocortex and hippocampal formation. *Cell*, 184(12):3222–3241.e26, June 2021.

[262] Pierre Yger, Giulia LB Spampinato, Elric Esposito, Baptiste Lefebvre, Stéphane Deny, Christophe Gardella, Marcel Stimberg, Florian Jetter, Guenther Zeck, Serge Picaud, Jens Duebel, and Olivier Marre. A spike sorting toolbox for up to thousands of electrodes validated with ground truth recordings in vitro and in vivo. *eLife*, 7:e34518, March 2018. Publisher: eLife Sciences Publications, Ltd.

[263] Ofer Yizhar, Lief E. Fenno, Thomas J. Davidson, Murtaza Mogri, and Karl Deisseroth. Optogenetics in Neural Systems. *Neuron*, 71(1):9–34, July 2011.

[264] P. K. Yong and E. T. Wei Ho. Streaming brain and physiological signal acquisition system for IoT neuroscience application. In *2016 IEEE EMBS Conference on Biomedical Engineering and Sciences (IECBES)*, pages 752–757, December 2016.

[265] Xinyue Yuan, Manuel Schröter, Marie Engelene J. Obien, Michele Fiscella, Wei Gong, Tetsuhiro Kikuchi, Aoi Odawara, Shuhei Noji, Ikuro Suzuki, Jun Takahashi, Andreas Hierlemann, and Urs Frey. Versatile live-cell activity analysis platform for characterization of neuronal dynamics at single-cell and network level. *bioRxiv*, page 2020.05.01.071787, May 2020. Publisher: Cold Spring Harbor Laboratory Section: New Results.

[266] Maria-Patapia Zafeiriou, Guobin Bao, James Hudson, Rashi Halder, Alica Blenkle, Marie-Kristin Schreiber, Andre Fischer, Detlev Schild, and Wolfram-Hubertus Zimmermann. Developmental GABA polarity switch and neuronal plasticity in Bioengineered Neuronal Organoids. *Nature Communications*, 11(1):3791, July 2020. Number: 1 Publisher: Nature Publishing Group.

[267] Friedemann Zenke and Wulfram Gerstner. Hebbian plasticity requires compensatory processes on multiple timescales. *Philosophical Transactions of the Royal Society of London. Series B, Biological Sciences*, 372(1715), 2017.

[268] Danqing Zhu, David H. Brookes, Akosua Busia, Ana Carneiro, Clara Fannjiang, Galina Popova, David Shin, Kevin C. Donohue, Li F. Lin, Zachary M. Miller, Evan R. Williams, Edward F. Chang, Tomasz J. Nowakowski, Jennifer Listgarten, and David V. Schaffer. Optimal trade-off control in machine learning–based library design, with application to adeno-associated virus (AAV) for gene therapy. *Science Advances*, 10(4):eadj3786, January 2024. Publisher: American Association for the Advancement of Science.

[269] Danqing Zhu, Adam J. Schieferecke, Paola A. Lopez, and David V. Schaffer. Adeno-Associated Virus Vector for Central Nervous System Gene Therapy. *Trends in Molecular Medicine*, 27(6):524–537, June 2021.